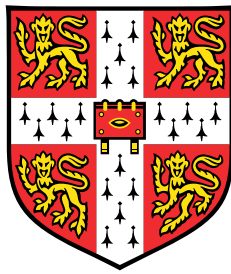


Synthesis of neuromorphic circuits with neuromodulatory properties



Luka Ribar

Supervisor: Prof. R. Sepulchre

Department of Engineering
University of Cambridge

This dissertation is submitted for the degree of
Doctor of Philosophy

Trinity College

October 2019

Declaration

I hereby declare that except where specific reference is made to the work of others, the contents of this dissertation are original and have not been submitted in whole or in part for consideration for any other degree or qualification in this, or any other university. This dissertation is my own work and contains nothing which is the outcome of work done in collaboration with others, except as specified in the text and Acknowledgements. This dissertation contains fewer than 65,000 words including appendices, bibliography, footnotes, tables and equations and has fewer than 150 figures.

Luka Ribar
October 2019

Abstract

Title: Synthesis of neuromorphic circuits with neuromodulatory properties

Author: Luka Ribar

The field of neuromorphic engineering shows great promise in delivering novel devices inspired by biological principles that would undertake sensory and processing tasks with an unprecedented level of efficiency. In order to achieve that, engineers are required to understand and implement the many complex biological regulatory mechanisms that allow the nervous system to robustly operate and adapt over scales covering many orders of magnitude, while at the same time using unreliable and noisy components.

As a step towards that, this thesis aims at discussing and implementing the principles of neuromodulation in neuromorphic hardware, mechanisms which allow neurons to change and regulate their behaviour through the continuous control of their internal currents. We discuss how neural dynamics and its modulation can be broken down into four essential feedback loops, and we introduce a simplified model of the neural membrane respecting this fundamental structure. We present a novel methodology for controlling the neuron's behaviour through the shaping of its I-V curves in distinct timescales, thus characterising the behaviour of the neural circuit through its input-output properties. We show how modulation of the feedback loops affects the behaviour, and importantly, captures the transition between spiking and bursting oscillatory regimes, two major signalling modes of neurons. We then show how the architecture can be easily implemented using well-known neuromorphic building blocks based on subthreshold MOSFET circuits. Finally, we discuss how the excitability switch captured by the model can be exploited in simple network settings, thus opening up the possibility for future research into novel architectures where the control of cellular properties is utilised to shape the global behaviour of the network.

Acknowledgements

Firstly, I would like to thank my supervisor Prof. Rodolphe Sepulchre for his guidance, academic advice and trust in me. His enduring enthusiasm and positive outlook at the research questions at hand have truly been inspirational, and have kept me pushing through even in periods when progress would seem to stall.

I would like to thank Dr Alessio Franci and Dr Guillaume Drion whose initial research much of the work presented here is based on, and whose insightful comments helped shape the results of the thesis. The hardware implementation presented in Chapter 5 was done in collaboration with Dr Felix Miranda, whose help and advice I am sincerely grateful for. I also gratefully acknowledge the financial support from Trinity College and the European Research Council I have received throughout my studies.

The Control Group has been a wonderful work environment, and I would like to thank all the past and present members of the group for providing such a relaxed and fun place to work in. I would particularly like to thank my fellow PhD students Tomas, Thiago, Ilario and Alessandro who shared much of the journey with me, and have been a great company in the many academic discussions, lunches, coffee breaks, pub nights and trips.

Cambridge has been a second home for me for eight years, and during this time I have met many close friends whose constant support has been irreplaceable. Thanks to Sasa and Andrea for sharing the PhD ups and downs and all the umami nights, as well as Eric, Mihajlo, Nikola, Dusan, Milan, Mario and many other college and non-college friends for making it a fun and exciting experience even in those periods when *nothing would seem to work*. Thanks to Sandy for providing so much support and keeping my sanity in check in this critical period - I know it was not easy. I would also like to thank the many friends from home who have been an ongoing part of my life - in particular Ognjen, Mina and Nevena for the many Skype conversations and kafana evenings at home, as well as Marko, whose PhD experience, positive and negative, so often mirrored mine.

Lastly, I want to thank my family, and particularly, my parents, for their continual encouragement, patience, support and advice, and for believing in me even when I did not.

Table of contents

List of figures	xiii
List of tables	xvii
1 Introduction	1
1.1 Outline	3
2 Neuronal excitability and neuromodulation	5
2.1 Excitability	6
2.1.1 The Hodgkin-Huxley model	7
2.1.2 Feedback structure of excitability	10
2.1.3 Minimal models of excitability	13
2.2 Multi-scale excitability: Bursting	15
2.2.1 Feedback structure of bursting	16
2.2.2 Minimal models of bursting	18
2.3 Neuromodulation	19
2.3.1 Neuromodulation as circuit loop shaping	20
Appendix 2.A Linearising Hodgkin-Huxley equations	22
Appendix 2.B Linearising R-15 neuron model equations	23
Appendix 2.C Simulation parameters	25

3	Neuromorphic engineering	29
3.1	Overview of the neuromorphic approach	30
3.2	Neuromorphic neurons	31
3.2.1	Biophysically accurate circuits	32
3.2.2	Simplified circuits	32
3.2.3	Balancing between?	33
3.3	Neuromorphic building blocks	34
3.3.1	Subthreshold regime	34
3.3.2	I-V element primitive: Transconductance amplifier circuit	37
3.3.3	Dynamical primitive: follower-integrator	38
	Appendix 3.A Simulation note	40
4	Neuromodulation through I-V curve shaping	41
4.1	I-V curve shaping by interconnection	42
4.2	Shaping an excitable circuit	46
4.3	Neuromodulating an excitable circuit	49
4.4	Shaping a bursting circuit	49
4.5	Neuromodulating a bursting circuit	54
4.5.1	Bursting/spiking modulation through slow I-V curve	57
4.6	Fragile and rigid bursting mechanisms	60
	Appendix 4.A Graphical interface for I-V curve neuromodulation	63
	Appendix 4.B Transcritical bifurcation in the bursting model	64
	Appendix 4.C Simulation parameters	66
5	Circuit design	69
5.1	Circuit elements	70
5.1.1	Implementation of a localised conductance element	70
5.1.2	Implementation of the passive element	71

5.2	SPICE simulation	73
5.3	Robustness of I-V curve shaping	75
5.4	Hardware implementation	77
	Appendix 5.A Transconductance amplifier linearisation	81
6	Excitability switch: from single neurons to networks	83
6.1	Single cell control	84
6.1.1	Modulating single neuron I/O properties	84
6.1.2	External I/O modulation	86
6.2	Neural interconnections	88
6.2.1	Synapse Circuit	90
6.3	Half-centre oscillator	91
6.3.1	Excitability switch through inhibition	93
6.4	Central pattern generator	94
	Appendix 6.A Simulation parameters	99
7	Conclusion	101
7.1	Summary	101
7.2	Future work	103
	References	105

List of figures

2.1	Input-output characteristic of excitable systems	7
2.2	The Hodgkin-Huxley circuit	8
2.3	Steady-state and time-constant functions of the gating variables	9
2.4	Linearisation of the Hodgkin-Huxley currents	11
2.5	Linearised Hodgkin-Huxley circuit	11
2.6	Linearised conductances of the Hodgkin-Huxley model	12
2.7	Input-output characteristic of bursting systems	15
2.8	Linearised conductances of the Aplysia R-15 bursting model	17
2.9	A general conductance-based circuit	21
3.1	An n-channel MOSFET	35
3.2	Drain-source current (i_{ds}) as a function of the drain-source voltage (v_{ds}) and the gate-source voltage (v_{gs})	35
3.3	Transconductance amplifier	37
3.4	Follower-integrator circuit	39
4.1	The neural circuit	42
4.2	Synthesis of an excitable circuit	46
4.3	Properties of an excitable circuit	47
4.4	The “N-shaped” fast I-V curve	48
4.5	Amplitude of the spikes is determined by the fast I-V curve	50

4.6	Tuning the frequency of spiking	51
4.7	Synthesis of a bursting circuit	51
4.8	Slow excitable circuit	52
4.9	Slow bistability between the rest state and the spiking state	53
4.10	Properties of a bursting circuit	55
4.11	Controlling the bursting waveform	56
4.12	Controlling the intraburst and interburst frequencies of the circuit	57
4.13	Controlling the oscillation mode	59
4.14	Type I excitable neuron	60
4.15	Generating bursting from a Type II neuron	61
4.16	Generating bursting from a Type I neuron	62
4.17	Graphical interface for simulating a single neuron	63
5.1	Implementation of a localised conductance element	70
5.2	Linearised transconductance amplifier	72
5.3	Comparison of input-output characteristics of the regular and linearised transconductance amplifiers	73
5.4	Transition between bursting and spiking modes in the SPICE circuit simulation	74
5.5	Compensating for process variation	76
5.6	Temperature dependence of the circuit	78
5.7	Breadboard with a single neuron circuit	79
5.8	Burst excitability of the circuit	79
5.9	Bursting and spiking traces of the circuit	80
5.10	Transition between spiking and bursting in the circuit	80
5.11	Small-signal analysis of the linearised transconductance amplifier	81
6.1	Neural circuit's input-output properties in the oscillating regime	85
6.2	Hyperpolarisation-induced bursting	87

6.3	Synapse circuit	90
6.4	Half-centre oscillator disconnected	92
6.5	Half-centre oscillator connected	92
6.6	Excitability switch in the half-centre oscillator	92
6.7	Inhibitory switch of neuron excitability	93
6.8	CPG disconnected	95
6.9	CPG connected	96
6.10	Disconnecting a rhythm from the CPG	97

List of tables

- 4.1 Parameter values for simulations in Chapter 4 67
- 6.1 Parameter values for simulations in Chapter 6 99

Chapter 1

Introduction

Although recently there has been a myriad of astonishing developments in artificial intelligence and robotics, comparing the state-of-the-art digital hardware and biological systems still shows a striking discrepancy in robustness, adaptability and energy efficiency between the two. The fact that even the simplest animals possess an awesome repertoire for sensing and navigating their environments while at the same time using very little energy has led scientists and engineers to believe that there are significant fundamental advantages to the organisational principles that biology utilises compared to the established semiconductor techniques. This realisation has ushered in an interest in understanding and applying the biological neural mechanisms in silicon, leading to the field of *neuromorphic engineering*, coined by the early pioneer Carver Mead in the late 1980s.

Since its inception, neuromorphic engineering has showed great promise in developing novel, biologically inspired devices that would undertake the complex motor, sensory and processing tasks in new, more efficient ways. Early developments in emulating the structure of the retina and the cochlea in semiconductor technology have been successful at demonstrating how the sensory information processing can be undertaken on the hardware level. This has led to advancements in developing efficient systems that would have extraordinary adaptation capabilities, while at the same time optimising the use of the available bandwidth by intelligently compressing signals, much like our own sensory systems do. Spiking neural chips have sparked an ongoing interest into developing non-von Neumann architectures for processing tasks. At the same time, engineers have been inspired by the developments in artificial neural networks to develop hardware solutions that would have the same learning

capabilities, with novel devices showing promise in implementing learning rules using the device physics.

The potential of neuromorphic systems is undoubtedly great and it has ignited renewed interest within the semiconductor industry as a possible way forward past the end of Moore's law era. Nevertheless, important issues remain that still prove to be a bottleneck in expanding the biologically inspired analogue concepts to mass production. The unreliability of the basic components and their fragility to noise in low-power analogue applications highlights the prevailing question in building neuromorphic systems: how does nature utilise unreliable building blocks in order to build robust and adaptable systems? Understanding this requires us not only to try to replicate the observable biological behaviour, but to identify the key organisational principles that are used in biological systems and translate them to circuit architectures that can be implemented in hardware. Uncovering these principles is a necessary step for both synthesising and controlling such systems.

Biological principles that allow the rich adaption of neural systems are prevalent on all scales: from the tiny ion channels that shape the single neuron behaviour, to the neural networks that control actions such as locomotion and breathing through the collective action of many neurons and their interconnections, to finally entire brain regions that produce cognitive emergent behaviour. One of the key control principles in neuroscience is *neuromodulation*. It covers the effects of various chemicals on internal properties of neurons, and subsequently, how they shape the electrical behaviour of cells. As such, the cumulative action of neuromodulatory substances can have profound effects on neural behaviour by drastically changing their firing patterns and properties such as frequency and duty cycle.

The aim of this thesis is to introduce the principles of neuromodulation as an engineering concept that can be applied to simple neuromorphic circuits. We present a simple circuit architecture and show how it captures the fundamental feedback loops present in biological neurons, and how the circuit's behaviour can be modulated by considering its input-output properties. As such, the methodology does not require intricate knowledge of the neural physiology, but allows for a rich set of different behaviours. More importantly, the architecture aims to reproduce the same neuromodulatory mechanisms in a simplified modelling framework, so that the circuit not only produces various different waveform patterns, but captures the underlying dynamics, in turn capturing the same robustness and adaptation capabilities.

1.1 Outline

The thesis is structured in the following way:

Chapter 2 covers the biological and modelling background behind neuronal excitability and neuromodulation. It begins by introducing the fundamental concept of excitability and the classical Hodgkin-Huxley model of an excitable cell. We then take a look at neuronal bursting and an example model in the conductance-based framework. In both cases we dissect and highlight the essential feedback mechanisms present in the models that are responsible for the complex nonlinear behaviour. We compare these to the minimal models of excitability and bursting and show how minimal models capture the same feedback structure. Finally, we take a look at neuromodulation, and how it can be understood as a cumulative effect of many agents on the same fundamental feedback loops.

Chapter 3 gives an overview of the neuromorphic approach and some of the fundamentals of the VLSI circuit design behind it. It starts with a brief overview of the history of neuromorphic devices and some of the major achievements of the field so far. We revisit the prevailing modelling concepts, and motivate the need for simple architectures capturing the biological neuromodulatory mechanisms. The second part of the chapter introduces the fundamental building blocks and the principles of subthreshold MOSFET design widely utilised within the neuromorphic community, which will serve as the basis for our own synthesis approach.

Chapter 4 covers the main results of the thesis. We first introduce the model of the circuit architecture that we will be using, and introduce the concepts of neuromodulation through *I-V curve shaping*. We show how designing different behaviours in this way reduces to the synthesis of I-V curves in the appropriate timescales. The initial construction covers the design of an excitable circuit, after which we show how the same principles can be extended to model more complicated behaviour such as neuronal bursting. We show how the feedback loops of the circuit can be modulated to control its behaviour, and how this relates to the I-V curves. This chapter is largely based on work presented at IEEE BioCAS 2017 [88] and published in IEEE Circuits and Systems [90].

Chapter 5 builds upon the previous chapter to show how the model introduced in Chapter 4 can be realised in hardware using the methodology from Chapter 3. We show how each

element has a simple realisation using the standard MOSFET transconductance amplifiers operating in the subthreshold regime. To this end, we provide a SPICE simulation using the TSMC 0.35 μm model parameters. Finally, we provide a proof-of-concept realisation using off-the-shelf discrete components and showcase its modulation capabilities. This chapter is largely based on work published in IEEE Circuits and Systems [90].

Chapter 6 discusses the potential of the circuit architecture from Chapters 4 and 5 for building small rhythm generating networks. We start by outlining the different properties of spiking and bursting neural regimes, why this excitability switch can have important consequences in a network setting, and how it can be implemented through external current modulation. We start the network construction by introducing a simple model of neural synapses using the same principles utilised in modelling conductance elements of single neurons. We then show how an elementary oscillatory unit in the form of a half-centre oscillator can be realised using these elements, and how a simple pattern generating network inspired by the stomatogastric ganglion can switch between different rhythms. In both cases, the modulatory properties of the individual cells are essential for the switching behaviour at the network level. Some of the results in this chapter were presented at CNS 2018 [89].

Chapter 7 provides conclusions and discusses the potential for future work. On the single neuron level, this includes the study into homeostasis-inspired mechanisms that would allow automatic regulation of neuronal properties in the face of technological variation, noise and temperature dependence. On the network level, this includes future studies into small pattern generating networks, as well as the potential in using the architecture in devices inspired by biological sensory networks.

Chapter 2

Neuronal excitability and neuromodulation

Neurons are the basic processing units of animal nervous systems, and as such, are responsible for the plethora of different functions such as analysing sensory stimuli, memory, generation of movement, awareness, cognition and others. Each individual neuron receives information from potentially many other neurons through synaptic and electrical connections, processes the information while taking into account the memory of its past activity, and in turn, affects other neurons it is connected to in the network. Every neuron in itself is a complex dynamical system [57], where the voltage across its membrane is determined by the joint operation of possibly many ion channels that open or close in response to changes in the membrane voltage and thus allow the ionic currents to flow across and control the voltage. Single neurons vary greatly and are able to experience rich dynamical behaviour [53, 25], while networks consisting of many such cells obtain their functions through complex interactions of all its individual units [117].

It is a daunting task to analyse these systems that transcend many spatial and temporal scales, mostly because of the prevailing question: what properties in the small scale are fundamental for the activity in the large scale, and how does changing these properties modulate the global behaviour? Therefore, finding simple prevailing mechanisms in the neural behaviour is of paramount importance, mainly for two reasons:

- Firstly, it leads to the analytical understanding, as mapping the many parameters of detailed biophysical models to a few aggregate ones unveils their respective roles in the behaviour, as well as the role of biological redundancies.

- Secondly, and in line with this thesis' aims, simple models capturing the essential dynamical mechanisms allow us to design neuromorphic systems that would be able to experience rich biological behaviour, but also be susceptible to straightforward analysis and manufacturing.

This chapter presents a brief overview of the fundamental properties of neurons and their physiological background, including the identification of the minimal necessary dynamical components required for robust and controllable simplified models.

We first revisit the fundamental notion of excitability, and the classical biophysical model of an excitable cell in the form of the Hodgkin-Huxley conductance-based model. We aim to present the well-known results through a simplified feedback outlook that uncovers the essential dynamical components for the excitable behaviour. Next, we take the same approach to more complex neuronal behaviours such as *bursting*: again starting with a biophysical conductance-based model, we dissect the essential feedback loops and compare the structure with the previous picture of excitability. In both cases we show how the simplified feedback structure relates to the minimal mathematical models of neuronal activity.

Finally, we examine basic neuromodulatory mechanisms that allow a neural cell to actively change its properties, and relate those complex mechanisms to the simple feedback structure identified previously.

2.1 Excitability

We start by introducing the defining input-output property of neurons, which is *excitability*.

We characterise a neuron's input-output relationship by considering the externally applied current as the input, and the cell's membrane voltage as the output. In that sense, a neuron is excitable because for small, sub-threshold input pulses, the output will change slightly before relaxing to rest again. In contrast, a current above a certain level will have a significantly different effect: the voltage goes through a large, well-defined excursion called an action potential (Fig. 2.1), before returning to rest. Such specific non-linear behaviour comes from the appropriate balance of ionic currents that flow through the membrane and react to the changes in the membrane voltage. In order to understand how ionic currents provide the feedback loops behind excitability, we will first take a look at the physiological background behind the excitability of neurons.

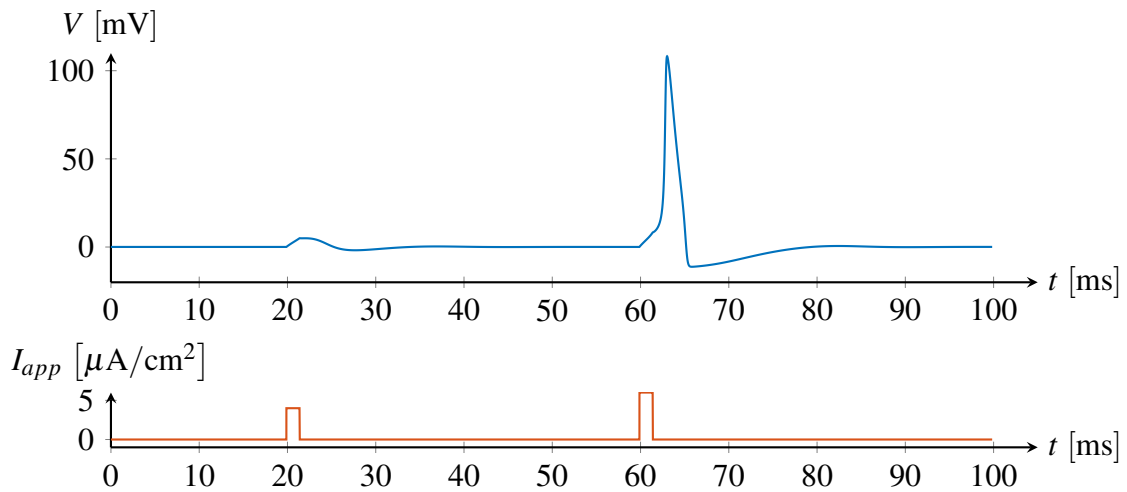


Fig. 2.1: Input-output characteristic of excitable systems. Subthreshold inputs generate subthreshold outputs, but suprathreshold inputs generate an all-or-none response in the form of one or several action potentials. Response shown for the Hodgkin-Huxley neural model.

2.1.1 The Hodgkin-Huxley model

The classical picture of excitability comes from the analysis of Hodgkin and Huxley of the squid giant axon in 1952 [43]. Although the analysis concentrated on this particular neuron, the methodology was later applied to explain the behaviour of other neural cells. The starting point of the analysis is that the excitable membrane can be modelled as an electrical circuit (Fig. 2.2).

Firstly, every cell consists of an impermeable membrane which is able to maintain an electrical potential difference between the intercellular and the extracellular environments. This property is modelled with a capacitor which stores the charge between the two media. In addition to this, the membrane is equipped with special proteins called *ion channels* which are selectively permeable to specific ions in the environment. Due to the different concentrations of ions inside and outside the cell, the cell dynamically controls its membrane voltage by opening and closing these channels and thus controlling the ion currents that pass through them. Hodgkin and Huxley were able to identify the key players for the generation of electrical pulses in the squid axon: potassium (K^+) and sodium (Na^+) ion currents, lumping all other currents into a third, leak component. The selective permeability to each ion is captured by an individual conductance element in the circuit, while the equilibrium voltage where the diffusion is exactly balanced by the electrical force is captured by a battery in each ion branch. There is a higher concentration of sodium outside the cell than inside, and vice-versa for potassium. Within the circuit modelling framework, this translates to

the sodium battery potential being higher than the membrane voltage, while the potassium battery potential is lower. Thus, sodium current is always inward (negative by convention) and acts to increase the voltage, while potassium current is outward (positive by convention) and acts to decrease the voltage.

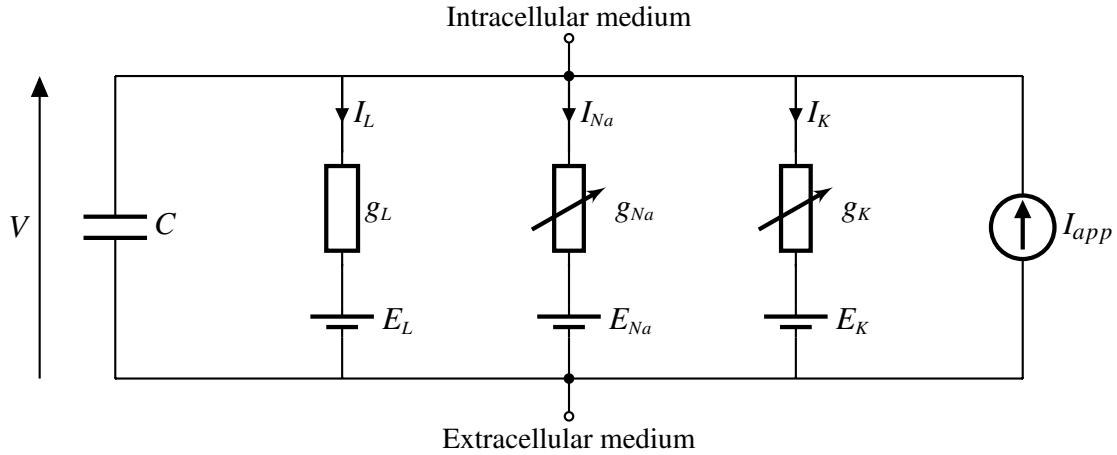


Fig. 2.2: The Hodgkin-Huxley circuit. The neural membrane, separating the intracellular and the extracellular media, is modelled as a parallel interconnection of the passive capacitor and leak current I_L , together with the active sodium I_{Na} and potassium I_K currents. External current applied to the cell is represented with the current source I_{app} .

The dynamics of the system are therefore governed by the following equation:

$$C_m \frac{dV}{dt} = -g_{Na}(V - E_{Na}) - g_K(V - E_K) - g_L(V - E_L) + I_{app} \quad (2.1)$$

where C_m is the membrane capacitance, V is the membrane voltage, g_{Na} , g_K , and g_L are the conductances corresponding to sodium, potassium and leak respectively, with E_{Na} , E_K and E_L being their corresponding equilibrium potentials, and I_{app} is the externally injected current into the cell.

Sodium and potassium conductances are *active* i.e. they are voltage and time dependent. This reflects the continuous opening and closing of their ion channels, in contrast to the leak conductance which is constant, and accounts for the passive properties of the membrane. By using the technique known as *voltage clamping*, Hodgkin and Huxley were able to keep the membrane voltage fixed at different levels and measure independently the transient currents due to sodium and potassium, thus effectively being able to measure different step responses from the resting state of the system. Fitting the data to the simplest form, they

obtained the equations for the two conductances:

$$g_{Na} = \bar{g}_{Na} m^3 h \quad (2.2)$$

$$g_K = \bar{g}_K n^4 \quad (2.3)$$

where \bar{g}_{Na} and \bar{g}_K are the maximal conductances of sodium and potassium respectively, and m , h , and n are the gating variables that follow first-order dynamics:

$$\begin{aligned} \tau_m(V) \dot{m} &= m_\infty(V) - m \\ \tau_h(V) \dot{h} &= h_\infty(V) - h \\ \tau_n(V) \dot{n} &= n_\infty(V) - n \end{aligned} \quad (2.4)$$

Each gating variable has a value between 0 and 1 and thus represents the continuous tuning of the ion channels between being fully closed and fully open. The steady-state functions $m_\infty(V)$, $h_\infty(V)$, and $n_\infty(V)$ have a sigmoidal shape (Fig. 2.3, left), while the voltage-dependent time-constants τ_m , τ_h , and τ_n have a Gaussian shape (Fig. 2.3, right). The mathematical form of the functions and parameter values can be found in the Appendix 2.C.

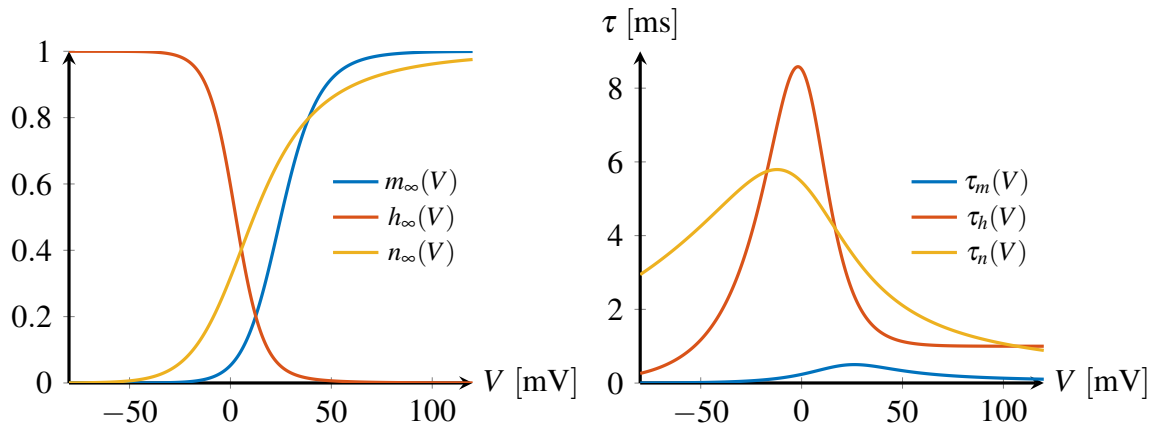


Fig. 2.3: Steady-state and time-constant functions of the gating variables. The steady-state functions (left) have a sigmoidal shape and are monotonically increasing for activation variables, and monotonically decreasing for inactivation variables. The time-constants (right) have a Gaussian shape.

The dynamics of each gating variable is fully characterised by these two voltage-dependent functions. The steady-state functions are monotonic and the voltage range in which the slope of these functions is non-zero defines the window in which the currents are active, while the slope defines the sign of the feedback. Thus, as m_∞ is monotonically increasing (called an *activation* variable) and sodium current is inward, we see that the vari-

able has a *positive feedback* effect on the membrane voltage, while h_∞ , being monotonically decreasing (called an *inactivation* variable), has a *negative feedback* effect. Similarly, due to the potassium current being outward and n_∞ being monotonically increasing, n also adds to the negative feedback.

The voltage-dependent time constants define the time-scale window in which the currents operate. To understand the essential mechanism behind excitability, it is not necessary to consider the specific shape of these functions, but to note that both n and h operate on a significantly slower time-scale than m . Thus m , being the source of positive feedback, acts quickly in response to the changes in voltage, while n and h which constitute to negative feedback, act slowly. This dynamical structure of **fast positive** in conjunction with **slow negative** feedback is a signature of excitable systems. We discuss this further in the following section by considering the linearisation of the Hodgkin-Huxley equations.

2.1.2 Feedback structure of excitability

In order to understand the role of the ionic currents in terms of their feedback effects, we can study the behaviour for small variations around different voltage levels, i.e. the behaviour of the *linearised* system [57]. When studied locally, the nonlinear circuit described in the previous chapter simplifies to a purely linear one, containing only the standard circuit components in the form of resistors, capacitors and inductors whose values depend on the voltage around which the system is studied.

If we apply a small change in the membrane voltage and look at the change in current within each branch, we can see that there are effectively two contributions: an instant change in the current, due to the passive properties of each ion current, and a slower component, due to the active properties of the gating variables. In circuit terms, the passive property leads to a simple resistor that gives an instantaneous change in current for a change in voltage, and each gating variable leads to a resistor-inductor branch, capturing the slower, first-order dynamics that arise. This is shown in Fig. 2.4, and the combined linearised circuit is shown in Fig. 2.5.

The value of each component will depend on the voltage around which we study the change. Writing this down, we get the linearised system equations (the derivation can be

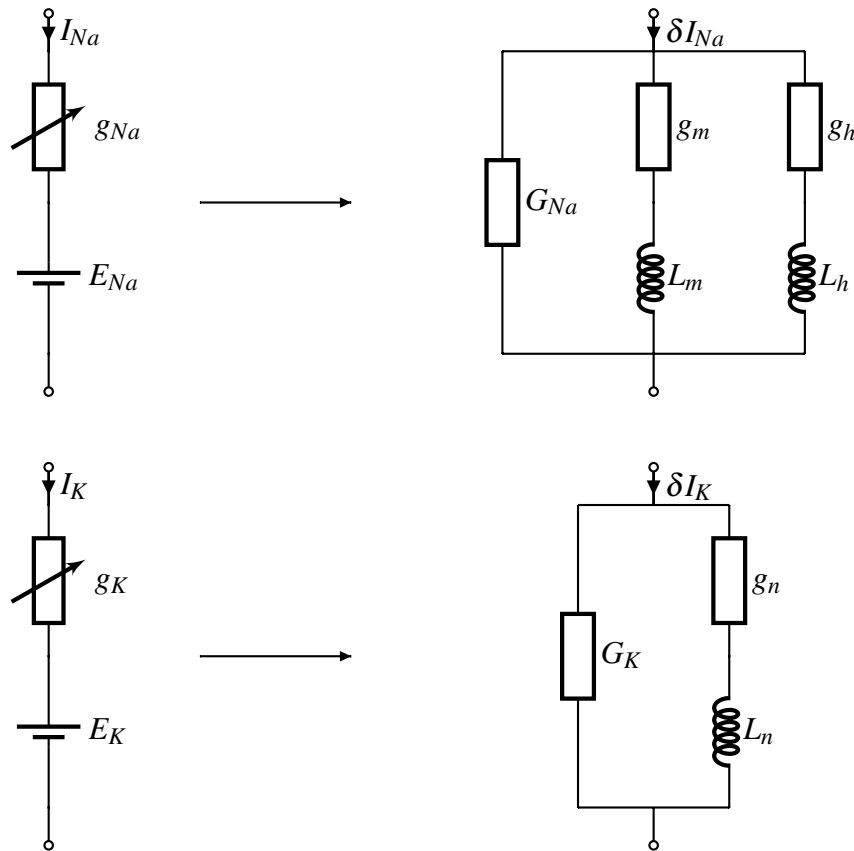


Fig. 2.4: Linearisation of the Hodgkin-Huxley currents. The sodium current (top) projects into three branches: passive, and one for each of the gating variables m and h . Similarly, potassium current (bottom) projects into a passive component and a branch corresponding to its activation variable n .

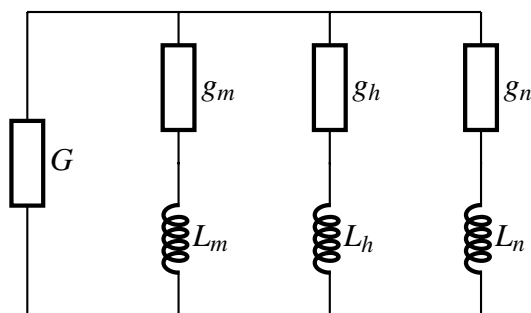


Fig. 2.5: Linearised Hodgkin-Huxley circuit. The circuit consists of the total passive component $G = \bar{g}_L + G_{Na} + G_K$, in parallel with the first-order branches corresponding to the gating variables. The fast positive feedback appears as the fast negative conductance branch $g_m - L_m$, while the slow negative feedback appears as the two positive conductance branches $g_h - L_h$ and $g_n - L_n$. All the values in the circuit are voltage-dependent, depending on the voltage point around which the linearisation is considered.

found in the Appendix 2.A):

$$\delta I_{Na} = G_{Na}(V^*) \delta V + \frac{g_m(V^*)}{\tau_m(V^*) d/dt + 1} \delta V + \frac{g_h(V^*)}{\tau_h(V^*) d/dt + 1} \delta V \quad (2.5)$$

$$\delta I_K = G_K(V^*) \delta V + \frac{g_n(V^*)}{\tau_n(V^*) d/dt + 1} \delta V \quad (2.6)$$

$$\delta I_L = \bar{g}_L \delta V \quad (2.7)$$

where V^* is the voltage value around which we are considering the linearisation. The passive components of the each branch can be grouped into a single conductance element $G = \bar{g}_L + G_{Na} + G_K$.

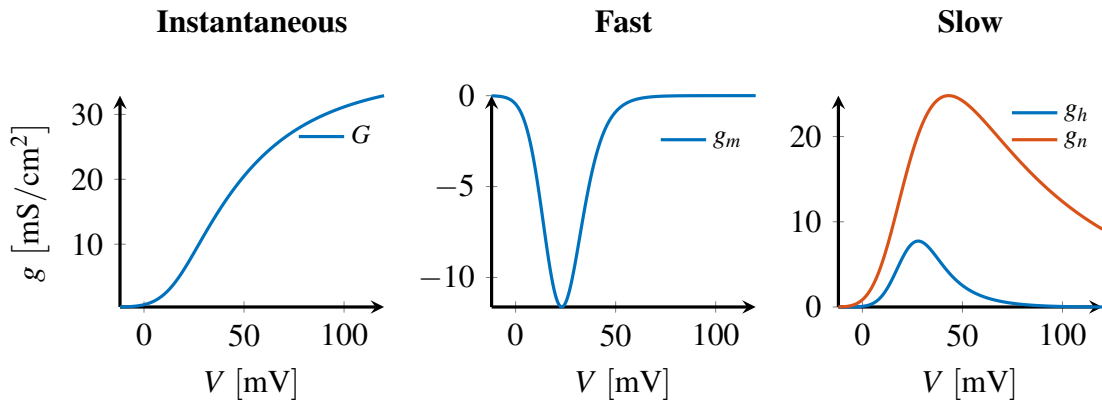


Fig. 2.6: Linearised conductances of the Hodgkin-Huxley model. The conductances are grouped in three parts: instantaneous (left), fast (middle) and slow (right). The excitability stems from the combination of the fast positive feedback (negative conductance) and the slow negative feedback (positive conductance).

The interesting insight from this analysis comes when we consider the steady state values of conductances at every voltage in the physiological range $V \in [E_K, E_{Na}]$. This is shown in Fig. 2.6, where we have grouped the conductances based on the timescale in which they are acting:

- The *instantaneous* branch describes the passive dissipative property of the membrane.
- The *fast* branch is due to the fast action of the sodium activation, which is several times faster than the sodium inactivation and potassium activation (Fig. 2.3, right).
- The *slow* branch is due to the slower action of the sodium inactivation and potassium activation.

The linearisation therefore illuminates the dynamical signature of excitable systems in terms of the circuit structure. The instantaneous branch is purely positive and captures the passive dissipative properties of the membrane (Fig. 2.6, left). As the sodium current is inward, its activation provides a positive feedback effect captured in the circuit as a negative conductance¹ (Fig. 2.6 middle), while its inactivation conversely provides a positive conductance in the slower timescale (Fig. 2.6, right). Similarly, potassium is an outward current, so that its activation leads to a negative feedback effect, captured again as a slow positive conductance (Fig. 2.6, right). Excitability comes from the interconnection of the passive circuit with a **fast negative** and a **slow positive** conductance.

The second important point captured by the linearisation is the local action of the dynamic currents. Both the fast negative conductance due to g_m and the slow positive conductance due to g_h and g_n act in a voltage window defined by their respective gating variables (i.e. where the derivatives of m_∞ , h_∞ and n_∞ are non-zero).

We therefore highlight the following properties of the currents of an excitable neuron:

- The feedback currents are *local in amplitude*: they act in a limited voltage window.
- The feedback currents are *local in time*: they have a well defined time-scale in which they act.

It is the combination of these two properties of the basic building blocks that allows for the complex neural behaviour that we observe. We show later how this property is captured in the architecture we introduce in Chapter 4.

2.1.3 Minimal models of excitability

The Hodgkin-Huxley formalism has been incredibly successful in describing the neurophysiological mechanisms of excitability. Since the publication of the model of the squid giant axon, there have been many conductance-based models of different excitable cells [15], differing in the structure of their ionic conductances, but retaining the same signature of excitable cells. The complexity of the original Hodgkin-Huxley model and the plethora of various excitable cells therefore leads to the question: what is the minimal mathematical model of excitability?

¹We use the term conductance interchangeably with *differential* conductance throughout the thesis.

The classical minimal model of excitability comes in the form of the FitzHugh-Nagumo equations [27, 79]. The model captures the essential excitability mechanism that requires fast positive feedback, and slow negative feedback in a two-dimensional model:

$$\begin{aligned}\dot{v} &= -\frac{v^3}{3} + v - w + I_{app} \\ \tau\dot{w} &= v + a - bw\end{aligned}\tag{2.8}$$

The model qualitatively captures the picture of Fig. 2.6 in a reduced sense: the instantaneous dissipative properties are captured by the term $\frac{v^3}{3}$, the fast negative conductance by the instantaneous term v , and the slow positive conductance by the term w . The state w is ensured to evolve on a significantly slower timescale than v by imposing $\tau \gg 1$.

The main contribution of the model has been to uncover the phase portrait picture of excitability. By reducing the number of states to two, the dynamics behind the generation of an action potential can be understood in the phase plane. In addition, the simple structure of the model allowed for straightforward circuit realisations, starting with the contribution from Nagumo and colleagues [79].

Another important minimal model that captures the excitability properties of the barnacle muscle fibre is the Morris-Lecar model [78]. Unlike the FitzHugh-Nagumo model, the model has a conductance-based structure which is why it has commonly been used when biophysical interpretability is needed. The model is minimal as it is two-dimensional and has the necessary and sufficient components for excitability: a fast negative conductance component, represented by the instantaneously activated inward calcium current, and slow positive conductance component, represented by the slowly activating potassium current. This leads to the following model:

$$\begin{aligned}C\frac{dV}{dt} &= -\bar{g}_{Ca}m_\infty(V)(V - E_{Ca}) - \bar{g}_K n(V - E_K) - \bar{g}_L(V - E_L) + I_{app} \\ \tau_n\dot{n} &= n_\infty(V) - n\end{aligned}\tag{2.9}$$

From the dynamical systems perspective, the model is also important because for different model parameters it can showcase different subtypes of excitability in a minimal representation, while at the same time being susceptible to the phase plane analysis.

2.2 Multi-scale excitability: Bursting

We now take a look at the more complex neuronal signalling behaviour in the form of *bursting*. Bursting is a dynamical property where a neuron is able to experience alternating periods of spiking behaviour, followed by periods of quiescence characterised by no activity. Although every excitable neuron can be turned into a burster with a sustained periodic input, here we concentrate on intrinsically bursting neurons which are able to generate such behaviour without an external stimulus. Such systems experience *burst excitability*, which showcases as an all-or-none response in the form of a burst of spikes, in contrast to the excitability discussed in Section 2.1. The characteristic input-output behaviour of bursting systems is shown in Fig. 2.7.

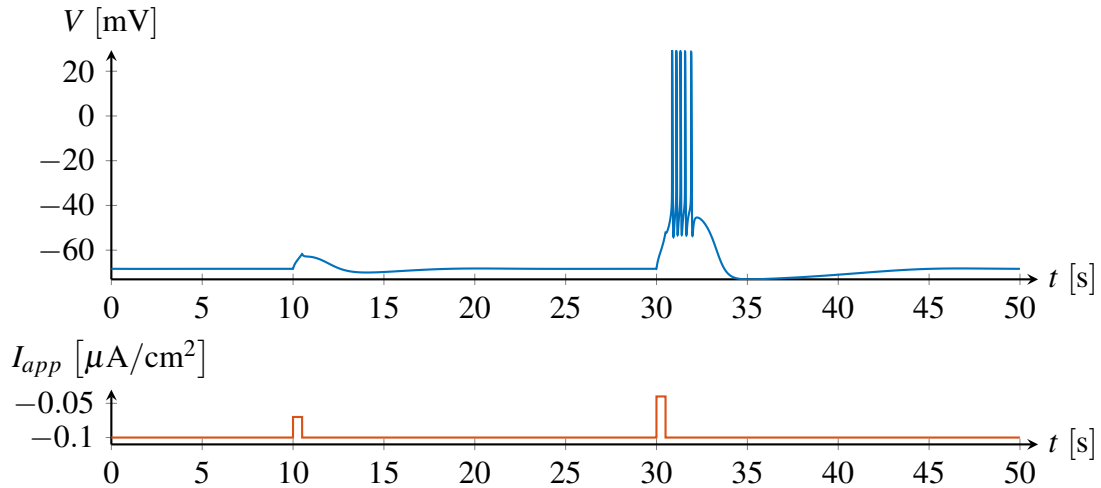


Fig. 2.7: Input-output characteristic of bursting systems. Similarly to the excitability property shown in Fig. 2.1, the subthreshold inputs generate small, subthreshold outputs. However, suprathreshold inputs generate a *burst* of spikes. Response shown for Aplysia R-15 model [94].

There are many biological examples of intrinsically bursting neurons, such as the neurons in the neocortex [14, 37], hippocampus [109], thalamus [108], cerebellum [118]. Other well-studied examples include the pancreatic β -cell [13], the Aplysia R-15 [84] and the neurons within the stomatogastric ganglion of crabs [70].

Although bursting activity can appear in vastly different forms, and different neurons utilise different combinations of ion channels to generate their activity, we would like to concentrate on the elementary mechanisms that are common to all of them. Bursting is fundamentally a two-timescale dynamical phenomenon, as it appears as an interplay of the slow wave that defines the bursting upstrokes and downstrokes, and the fast spiking behaviour

that is triggered during the active phases of the slow wave. Its generation therefore requires an interaction between a *slow excitable* subsystem, and a *fast excitable* subsystem, where the ionic agents responsible for either can differ in their structure.

We illustrate this structure on a specific example from the literature in the following section.

2.2.1 Feedback structure of bursting

We consider the neuron R-15 of *Aplysia* studied in [84, 94] as an illustration of a bursting neuron. Traditionally, it has been one of the most well-studied bursting neurons in the literature, and here we concentrate on one of the classical models of its behaviour. The neuron has the same ionic currents as the Hodgkin-Huxley model (Section 2.1.1), i.e. the sodium and potassium channels responsible for generating individual spikes, but in addition it has slower channels that are responsible for generating the slow variations of the membrane voltage. These channels are responsible for two additional ion currents: an inward calcium current, and an outward calcium-activated potassium current. The model has the following structure:

$$C_m \frac{dV}{dt} = -g_{Na}(V - E_{Na}) - g_K(V - E_K) - g_L(V - E_L) - g_{Ca}(V - E_{Ca}) - g_{K-Ca}(V - E_K) + I_{app} \quad (2.10)$$

where g_{Na} and g_K are as in Eq. (2.2) with the standard simplification that sodium activation is instantaneous (i.e. $m = m_\infty(V)$). The additional currents have the following characteristics:

$$g_{Ca} = \bar{g}_{Ca} x \quad (2.11)$$

$$g_{K-Ca} = \bar{g}_{K-Ca} \frac{c}{0.5 + c} \quad (2.12)$$

The calcium activation variable x and the calcium concentration c have the first-order dynamics:

$$\tau_x \dot{x} = x_\infty(V) - x \quad (2.13)$$

$$\tau_c \dot{c} = (K_c x (E_{Ca} - V) - c) \quad (2.14)$$

The detailed model parameters can be found in the Appendix 2.C. The time constants of the additional currents in the model τ_x and τ_c are significantly larger than the dynamics of

the Hodgkin-Huxley currents. The calcium current therefore activates slowly compared to the potassium current I_K , while in turn the calcium-activated potassium current I_{K-Ca} is the slowest in the model.

The two currents have a different structure, but they again play exactly the same roles as the Hodgkin-Huxley currents in establishing *slow excitability*. The calcium current is inward and its activation leads to a positive feedback effect acting on a slower timescale than the spiking generation dynamics, while the activation of the calcium-activated potassium current leads to a stabilising negative feedback effect in the slowest timescale of the model. Bursting generation can therefore be effectively divided into two parts: the fast spiking generation requiring a combination of fast positive and slow negative feedback effect currents, and the slow wave generation requiring currents that provide the same feedback structure, but acting on a significantly slower timescale.

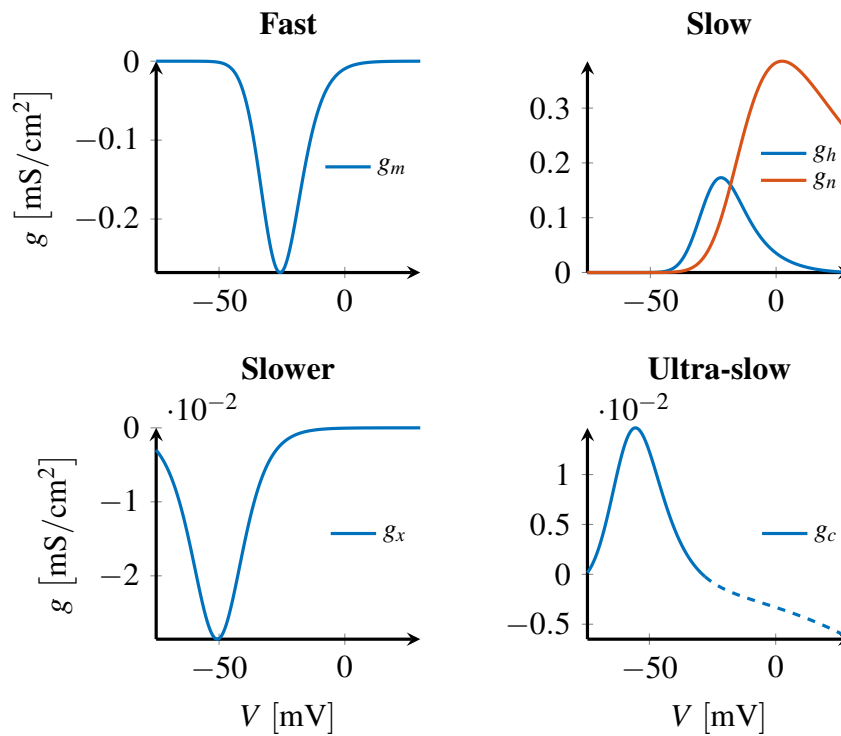


Fig. 2.8: Linearised conductances of the Aplysia R-15 bursting model. Building from the picture shown in Fig. 2.6, in addition to the fast negative and slow positive conductance necessary for spike generation (top), bursting requires additional slower negative and ultra-slow positive conductances (bottom). The two slower conductances activate at lower voltages than the two faster ones, so that the slow wave is generated in the lower voltage range. Note that at high voltage values the ultra-slow g_c becomes negative: the excursions in this range are too fast for the ultra-slow variable to have an effect.

We again observe this in the structure of the linearised circuit. Adding to the picture shown in Section 2.1.2, there are two additional active currents:

$$\delta I_{Ca} = G_{Ca}(V^*) \delta V + \frac{g_x(V^*)}{\tau_x d/dt + 1} \delta V \quad (2.15)$$

$$\delta I_{K-Ca} = G_{K-Ca}(V^*) \delta V + \frac{g_c(V^*)}{\tau_c d/dt + 1} \delta V \quad (2.16)$$

and we can plot the voltage dependence of the linearised conductances as before (Fig. 2.8). The derivation of g_x and g_c can be found in the Appendix 2.B. Note that the voltages are shifted compared to the Hodgkin-Huxley model, as the rest voltage is not set to lie at 0mV.

Again, linearisation illuminates the basic circuit structure of a bursting neuron. The **fast negative, slow positive** conductance of excitability is effectively repeated *twice*, so that the faster combination of the conductances generates the individual spikes within the burst, while the slower conductance combination generates the slow wave that turns the spiking on and off. In the example presented here, the source of slow negative conductance acts on a slower timescale than the sodium and potassium currents providing fast excitability. This may be further simplified by assuming the slower source of negative conductance acts on the same timescale of the slow positive conductance, and this simplification is further discussed in Section 2.2.2 and used in the circuit architecture introduced in Chapter 4.

Another important point is the different localisation in the voltage range: the fast conductances are localised in a higher voltage range than the slower conductances, which enables the activation of the slow wave to in turn activate the fast spiking threshold.

We will consider this dynamical organisation as the foundation for building models that are able to generate robust and controllable bursting waveforms.

2.2.2 Minimal models of bursting

There are various proposed mathematical models of bursting in literature, capturing the particular dynamical features of different neuronal bursting cells [53]. From the mathematical viewpoint, the main classification between the bursting types lies in the mechanism of the transition from resting to spiking and back. If the fast spiking system has a region of bistability between the resting and spiking states, then an additional slower variable is sufficient to drive the system around the hysteresis and generate a bursting attractor. However, if the fast system is monostable, then the slow system needs to be at least two-dimensional in order to generate

semi-autonomous slow oscillations that push the system between spiking and rest. Analysis of these mechanisms has led to an extensive classification that focuses on the bifurcations that lead to the transition between resting and spiking and vice-versa [51].

Recent work has illuminated the important fact that regardless of the underlying mechanism of bursting, in order to robustly model the dynamical features of bursting neurons, it is necessary to retain the essential four feedback loops discussed in the previous section [31, 16]. This has led to the proposed three-timescale model based on the transcritical singularity [30]. The model is based on the reduction of the Hodgkin-Huxley model with the addition of a slowly-activated calcium current [23], and has a similar form as the FitzHugh-Nagumo model. It also has a similar structure to the well-known Hindmarsh and Rose minimal model [42], but in addition, provides a mathematical framework for understanding the mechanisms that allow a system to modulate its behaviour between bursting and spiking modes. The model is the following:

$$\begin{aligned} \dot{v} &= -\frac{v^3}{3} + v - (n + n_0)^2 - z + I_{app} \\ \tau_n \dot{n} &= n_\infty(V - V_0) - n \\ \tau_z \dot{z} &= z_\infty(V - V_0) - z \end{aligned} \tag{2.17}$$

The model has two main differences compared to the FitzHugh-Nagumo model. Firstly, the slow variable is quadratic instead of linear: the variable therefore captures both the negative and the positive feedback effect in the slow timescale. In that sense, it captures two of the essential feedback loops in a single variable: the slow *positive* and the slow *negative* conductance, by assuming both currents act on the same timescale. Secondly, there is the additional ultraslow variable z that captures the ultraslow negative feedback effect. Because the model has the four essential feedback loops presented in Section 2.2.1, it is able to experience the full dynamical properties of bursting neurons, including the physiological transition between bursting and purely spiking regimes.

2.3 Neuromodulation

We have so far discussed the mechanisms that allow neurons to have different excitability properties, both in terms of their physiological structure, and the simplified feedback outlook. However, neurons are not “hard-wired”, but are able to actively change their pattern of behaviour. The ionic feedback loops of neurons are constantly tuned as a result of the

action of external signals, and this process is called *neuromodulation*. It covers the effects of different substances called neuromodulators on the electrical activity of neurons. Some examples of major neuromodulators include dopamine, serotonin, acetylcholine, histamine and norepinephrine [72].

Understanding how neuromodulation configures neural circuits and affects the behaviour is one of the most important questions in neuroscience, and in turn, in neural modelling and synthesis. The ability of neuromodulators to greatly modify the cellular properties of neurons means that the behaviour of sensory systems can be dynamically adjusted [58], as well as the way the information is relayed to the higher processing stages [102]. Rhythm generating networks known as the *central pattern generators* (CPGs) are constantly under the effect of neuromodulators [40, 68]. This allows them to swiftly change their rhythmic patterns in response to varying conditions, providing the amazing robustness and flexibility of animal locomotory actions. The capability of neuromodulation to target and modify local parts of neural networks in a matter of seconds is at the essence of the biological control across scales that allows the local changes to shape the global behaviour in a robust way [100, 101].

We will now briefly take a look at the modelling framework for neuromodulation. We aim to connect the problem of neuromodulation to the feedback structure we have shown in Sections 2.1 and 2.2.

2.3.1 Neuromodulation as circuit loop shaping

We have discussed two specific conductance-based models of neurons so far in Sections 2.1.1 and 2.2.1. Generally, we can consider an arbitrary neuron in the form of a conductance-based circuit (Fig. 2.9). A neuron may have many different ionic currents in parallel all working in unison to generate the specific neural behaviour.

In this modelling framework, we can consider the effects of the various external substances as modulating the maximal conductance parameters of the currents \bar{g}_i . Understanding how neuromodulators can drive the behaviour in the desired way therefore boils down to understanding which regions in the rich parameter space of the maximal conductances correspond to which behaviour. This is a difficult task due to the highly non-linear nature of the currents, but recent work [21] has proposed a way of viewing the modulation of maximal conductances as a form of *loop-shaping* of the basic feedback loops responsible for generating the behaviour.

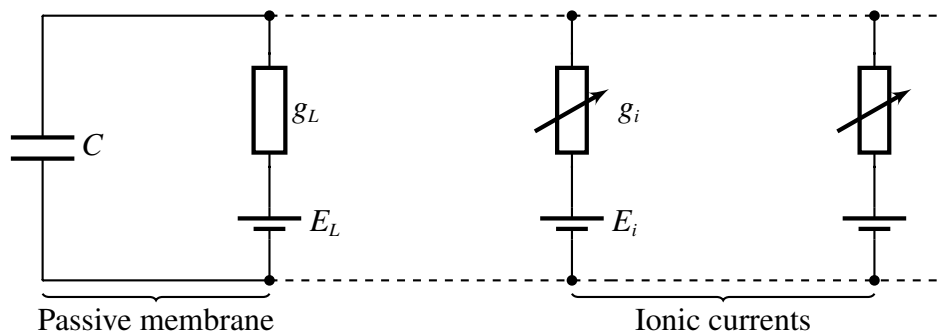


Fig. 2.9: A general conductance-based circuit. The passive membrane consisting of the membrane capacitor and the leak current is interconnected with possibly many ion currents.

In this sense, we can map the effects of the multitude of ion currents into only a few distinct timescales that are relevant for the spike-generation. The effects can be superimposed through the linearisation techniques discussed in Sections 2.1.2 and 2.2.1 into the aggregate conductances for each timescale: *fast*, *slow* and *ultra-slow*. Spiking then requires the appearance of fast negative conductance, and slow positive conductance, while bursting requires the addition of the slow negative conductance and ultra-slow positive conductance, appropriately localised in the voltage range.

Modulating the maximal conductances thus *shapes* the conductance in each timescale, changing the properties such as frequency, duty cycle, as well as the qualitative properties of the waveform. Balancing between the slow positive and slow negative conductance leads to the transition between the purely spiking and purely bursting modes, drastically altering the processing capabilities of neurons.

For any proposed neural model we can view its modulation as shaping the conductance in the appropriate timescale, and we will utilise this viewpoint for the design of neuromorphic neurons by exploiting the fact that it is both necessary and sufficient to appropriately model the conductance in the three relevant timescales.

Appendix 2.A Linearising Hodgkin-Huxley equations

We start by considering the change in sodium and potassium currents for a small change in voltage δV :

$$\delta I_{Na} = \left. \frac{\partial I_{Na}}{\partial V} \right|_{V^*} \delta V + \left. \frac{\partial I_{Na}}{\partial m} \right|_{V^*} \delta m + \left. \frac{\partial I_{Na}}{\partial h} \right|_{V^*} \delta h \quad (2.18)$$

$$\delta I_K = \left. \frac{\partial I_K}{\partial V} \right|_{V^*} \delta V + \left. \frac{\partial I_K}{\partial n} \right|_{V^*} \delta n \quad (2.19)$$

The partial derivatives are then calculated to be:

$$\left. \frac{\partial I_{Na}}{\partial V} \right|_{V^*} = \bar{g}_{Na} m_\infty^3(V^*) h_\infty(V^*) \quad (2.20)$$

$$\left. \frac{\partial I_{Na}}{\partial m} \right|_{V^*} = 3 \bar{g}_{Na} m_\infty^2(V^*) h_\infty(V^*) (V^* - E_{Na}) \quad (2.21)$$

$$\left. \frac{\partial I_{Na}}{\partial h} \right|_{V^*} = \bar{g}_{Na} m_\infty^3(V^*) (V^* - E_{Na}) \quad (2.22)$$

for sodium and:

$$\left. \frac{\partial I_K}{\partial V} \right|_{V^*} = \bar{g}_K n_\infty^4(V^*) \quad (2.23)$$

$$\left. \frac{\partial I_K}{\partial n} \right|_{V^*} = 4 \bar{g}_K n_\infty^3(V^*) (V^* - E_K) \quad (2.24)$$

for potassium. All the values are evaluated at an arbitrary voltage V^* around which we are linearising the system. By considering the dynamical equations for the gating variables (Eq. (2.4)), we obtain:

$$\delta m = \frac{dm_\infty/dV}{\tau_m(V^*) d/dt + 1} \delta V, \quad \delta h = \frac{dh_\infty/dV}{\tau_h(V^*) d/dt + 1} \delta V \quad (2.25)$$

and the same for potassium:

$$\delta n = \frac{dn_\infty/dV}{\tau_n(V^*) d/dt + 1} \delta V \quad (2.26)$$

Putting all of this together, we see that the total linearised sodium current has three components:

$$\delta I_{Na} = G_{Na}(V^*) \delta V + \frac{g_m(V^*)}{\tau_m(V^*) d/dt + 1} \delta V + \frac{g_h(V^*)}{\tau_h(V^*) d/dt + 1} \delta V \quad (2.27)$$

where:

$$G_{Na} = \frac{\partial I_{Na}}{\partial V} \quad (2.28)$$

$$g_m = \frac{\partial I_{Na}}{\partial m} \frac{dm_\infty}{dV} \quad (2.29)$$

$$g_h = \frac{\partial I_{Na}}{\partial h} \frac{dh_\infty}{dV} \quad (2.30)$$

and the total linearised potassium current has two components:

$$\delta I_K = G_K(V^*) \delta V + \frac{g_n(V^*)}{\tau_n(V^*) d/dt + 1} \delta V \quad (2.31)$$

where:

$$G_K = \frac{\partial I_K}{\partial V} \quad (2.32)$$

$$g_n = \frac{\partial I_K}{\partial n} \frac{dn_\infty}{dV} \quad (2.33)$$

Comparing these equations to the circuits in Fig. 2.4 gives the values of inductors as follows:

$$L_m = \frac{\tau_m}{g_m}, \quad L_h = \frac{\tau_h}{g_h}, \quad L_n = \frac{\tau_n}{g_n} \quad (2.34)$$

Appendix 2.B Linearising R-15 neuron model equations

As in Appendix 2.A, the changes in sodium and potassium currents can be found to be:

$$\delta I_{Na} = G_{Na}(V^*) \delta V + g_m(V^*) \delta V + \frac{g_h(V^*)}{\tau_h(V^*) d/dt + 1} \delta V \quad (2.35)$$

$$\delta I_K = G_K(V^*) \delta V + \frac{g_n(V^*)}{\tau_n(V^*) d/dt + 1} \delta V \quad (2.36)$$

We apply the same technique to the two additional currents, I_{Ca} and I_{K-Ca} . Starting from the partial derivatives, we obtain:

$$\delta I_{Ca} = \left. \frac{\partial I_{Ca}}{\partial V} \right|_{V^*} \delta V + \left. \frac{\partial I_{Ca}}{\partial x} \right|_{V^*} \delta x \quad (2.37)$$

$$\delta I_{K-Ca} = \left. \frac{\partial I_{K-Ca}}{\partial V} \right|_{V^*} \delta V + \left. \frac{\partial I_{K-Ca}}{\partial c} \right|_{V^*} \delta c \quad (2.38)$$

The partial derivatives for the calcium current are:

$$\left. \frac{\partial I_{Ca}}{\partial V} \right|_{V^*} = \bar{g}_{Ca} x_{\infty}(V^*) \quad (2.39)$$

$$\left. \frac{\partial I_{Ca}}{\partial x} \right|_{V^*} = \bar{g}_{Ca} (V^* - E_{Ca}) \quad (2.40)$$

and for the calcium-activated potassium current:

$$\left. \frac{\partial I_{K-Ca}}{\partial V} \right|_{V^*} = \bar{g}_{K-Ca} \frac{c_{\infty}(V^*)}{0.5 + c_{\infty}(V^*)} \quad (2.41)$$

$$\left. \frac{\partial I_{K-Ca}}{\partial c} \right|_{V^*} = \bar{g}_{K-Ca} \frac{0.5}{(0.5 + c_{\infty}(V^*))^2} (V^* - E_K) \quad (2.42)$$

where we have defined:

$$c_{\infty}(V) = K_c x_{\infty}(V) (E_{Ca} - V) \quad (2.43)$$

We approximate the calcium dynamics as a first-order equation by noting that $\tau_c \gg \tau_x$, so that we set $x = x_{\infty}(V)$ in Eq. (2.14). This simplification means that the linearisation with respect to the calcium concentration will again lead to a simple resistor-inductor branch. From Eqs. (2.13) and (2.14) we therefore obtain:

$$\delta x = \frac{dx_{\infty}/dV}{\tau_x d/dt + 1} \delta V \quad (2.44)$$

$$\delta c = \frac{dc_{\infty}/dV}{\tau_c d/dt + 1} \delta V \quad (2.45)$$

Putting all these together, we finally get:

$$\delta I_{Ca} = G_{Ca}(V^*) \delta V + \frac{g_x(V^*)}{\tau_x d/dt + 1} \delta V \quad (2.46)$$

$$\delta I_{K-Ca} = G_{K-Ca}(V^*) \delta V + \frac{g_c(V^*)}{\tau_c d/dt + 1} \delta V \quad (2.47)$$

with the passive components:

$$G_{Ca} = \frac{\partial I_{Ca}}{\partial V} \quad (2.48)$$

$$G_{K-Ca} = \frac{\partial I_{K-Ca}}{\partial V} \quad (2.49)$$

and the active components:

$$g_x = \frac{\partial I_{Ca}}{\partial x} \frac{dx_\infty}{dV} \quad (2.50)$$

$$g_c = \frac{\partial I_{K-Ca}}{\partial c} \frac{dc_\infty}{dV} \quad (2.51)$$

Appendix 2.C Simulation parameters

Hodgkin-Huxley

The Hodgkin-Huxley model has the following equations for the dynamics of the ion channels [55]:

$$\begin{aligned} \dot{m} &= \alpha_m(1 - m) - \beta_m m \\ \dot{h} &= \alpha_h(1 - h) - \beta_h h \\ \dot{n} &= \alpha_n(1 - n) - \beta_n n \end{aligned} \quad (2.52)$$

with the functions having the following forms:

$$\begin{aligned} \alpha_m &= 0.1 \frac{25 - V}{\exp\left(\frac{25 - V}{10}\right) - 1} \\ \beta_m &= 4 \exp\left(\frac{-V}{18}\right) \\ \alpha_h &= 0.07 \exp\left(\frac{-V}{20}\right) \\ \beta_h &= \frac{1}{\exp\left(\frac{30 - V}{10}\right) + 1} \\ \alpha_n &= 0.01 \frac{10 - V}{\exp\left(\frac{10 - V}{10}\right) - 1} \\ \beta_n &= 0.125 \exp\left(\frac{-V}{80}\right) \end{aligned}$$

The equations Eq. (2.52) can be rewritten in the form presented in the chapter (Eq. (2.4)), by using the following equations for the steady-state and time-constant functions:

$$\begin{aligned} m_\infty(V) &= \frac{\alpha_m(V)}{\alpha_m(V) + \beta_m(V)}, & \tau_m(V) &= \frac{1}{\alpha_m(V) + \beta_m(V)} \\ h_\infty(V) &= \frac{\alpha_h(V)}{\alpha_h(V) + \beta_h(V)}, & \tau_h(V) &= \frac{1}{\alpha_h(V) + \beta_h(V)} \\ n_\infty(V) &= \frac{\alpha_n(V)}{\alpha_n(V) + \beta_n(V)}, & \tau_n(V) &= \frac{1}{\alpha_n(V) + \beta_n(V)} \end{aligned}$$

The other parameters are then:

$$\begin{aligned} C_m &= 1 \mu\text{F}/\text{cm}^2 \\ \bar{g}_{Na} &= 120 \text{mS}/\text{cm}^2, & \bar{g}_K &= 36 \text{mS}/\text{cm}^2, & \bar{g}_L &= 0.3 \text{mS}/\text{cm}^2 \\ E_{Na} &= 120 \text{mV}, & E_K &= -12 \text{mV}, & E_L &= 10.6 \text{mV} \end{aligned}$$

Aplysia R-15

The parameters for Aplysia R-15 model are taken from [94]. The equations for the dynamics of the ion channels are the following:

$$\begin{aligned} \alpha_m &= 0.1 \frac{50 - V}{\exp\left(\frac{50 - V}{10}\right) - 1} \\ \beta_m &= 4 \exp\left(\frac{25 - V}{18}\right) \\ \alpha_h &= 0.07 \exp\left(\frac{25 - V}{20}\right) \\ \beta_h &= \frac{1}{\exp\left(\frac{55 - V}{10}\right) + 1} \\ \alpha_n &= 0.01 \frac{55 - V}{\exp\left(\frac{55 - V}{10}\right) - 1} \\ \beta_n &= 0.125 \exp\left(\frac{45 - V}{80}\right) \end{aligned}$$

For the steady-state and time-constant functions the following coordinate transformation is used:

$$\tilde{V} = C_1 V + C_2,$$

$$C_1 = 127/105, \quad C_2 = 8265/105$$

so that:

$$m_\infty(V) = \frac{\alpha_m(\tilde{V})}{\alpha_m(\tilde{V}) + \beta_m(\tilde{V})},$$

$$h_\infty(V) = \frac{\alpha_h(\tilde{V})}{\alpha_h(\tilde{V}) + \beta_h(\tilde{V})}, \quad \tau_h(V) = \frac{12.5}{\alpha_h(\tilde{V}) + \beta_h(\tilde{V})}$$

$$n_\infty(V) = \frac{\alpha_n(\tilde{V})}{\alpha_n(\tilde{V}) + \beta_n(\tilde{V})}, \quad \tau_n(V) = \frac{12.5}{\alpha_n(\tilde{V}) + \beta_n(\tilde{V})}$$

For x :

$$x_\infty(V) = \frac{1}{\exp(A(B - V)) + 1}, \quad \tau_x = 235 \text{ ms}$$

where

$$A = 0.15, \quad B = -50$$

For c :

$$\tau_c = 1/0.003 \text{ ms}$$

$$K_c = 0.0085 \text{ mV}^{-1}$$

The other parameters are:

$$C_m = 1 \mu\text{F}/\text{cm}^2$$

$$\bar{g}_{Na} = 4 \text{ mS}/\text{cm}^2, \quad \bar{g}_{Ca} = 0.004 \text{ mS}/\text{cm}^2,$$

$$\bar{g}_K = 0.3 \text{ mS}/\text{cm}^2, \quad \bar{g}_{K-Ca} = 0.03 \text{ mS}/\text{cm}^2, \quad \bar{g}_L = 0.003 \text{ mS}/\text{cm}^2$$

$$E_{Na} = 30 \text{ mV}, \quad E_{Ca} = 140 \text{ mV}, \quad E_K = -75 \text{ mV}, \quad E_L = -40 \text{ mV}$$

Chapter 3

Neuromorphic engineering

Since its inception, neuromorphic engineering has provided an exciting avenue for understanding and utilising the computational principles that underlie animal behaviour. The term *neuromorphic* [74] provides a good summary of the main objectives of the field: to apply the biological organisational principles to the established semiconductor technology with the aim of achieving the level of performance and energy efficiency observed in nature. Unlike the prevailing purely digital von Neumann architecture we are accustomed to, neural systems employ a mix of analogue and digital principles that allows them to operate at an amazing level of efficiency [95]. Reverse engineering these processes would allow scientists and engineers to approach closer to these levels of processing capabilities, while at the same time leading to a better understanding of the biological systems.

In this chapter we start by providing an overview of the different approaches undertaken within the neuromorphic community since the birth of the field 30 years ago. The field has covered many exciting applications, from understanding and recreating how our sensory systems behave, to building large neural networks that aim at uncovering the principles of cognition. We will focus on understanding the different levels of abstraction that the various approaches have utilised, and how these relate to the biophysical principles and the mathematical models we have described in Chapter 2. Through this, we aim to motivate the systems approach to synthesising and analysing neuromorphic circuits that we undertake in Chapter 4. Our aim is to use well-known neuromorphic circuits, and show how neural behaviours can be easily synthesised and controlled by respecting the fundamental feedback structure described in Chapter 2.

In the second part of the chapter we present the circuit building blocks that have been successfully utilised in analogue subthreshold neuromorphic circuits. We discuss the main characteristics of these circuits, and why they provide good basic elements for synthesising nonlinear I-V curves, as well as providing temporal filtering necessary for realising the dynamic nature of neurons.

3.1 Overview of the neuromorphic approach

The first steps towards utilising the silicon technology for recreating biological behaviour were undertaken by Carver Mead and his colleagues in the late 1980s [66, 73, 74]. By making an analogy between the behaviour of MOS transistors at low operating voltages and the channel dynamics of neurons, they provided a novel methodology for synthesising bioinspired systems by using the physics of the devices as a computational resource. This analogue way of computing is in contrast with the established digital technology where transistors are purely viewed as on/off switches, and computation is achieved by abstracting their behaviour and utilising the principles of Boolean algebra.

These initial studies led to the first developments of electrical circuits emulating the structure and operation of neurons, sensory organs and the fundamental organisational principles of neural networks. These included the first developments on implementing the conductance-based structure of neurons, which led to the development of the first silicon Hodgkin-Huxley based neuron [67], as well as replicating the auditory and vision sensory systems through the silicon cochlea [65, 114] and the silicon retina [75]. The most powerful aspect of these sensory devices is that they aim to achieve preprocessing of signals already at the level of hardware, much like our own sensory systems do. Such low-level computational methods using device physics enrich the hardware with automatic adaptation and compression mechanisms that can lead to significant savings in the bandwidth and processing requirements in the later stages. Other important functional primitives, such as the “winner-take-all” function used in decision making and action selection, also had successful hardware realisations [59]. Together with these, novel communicational methods were developed to circumvent the inability of implementing the massively interconnected neural structures found in biology. This was achieved by cleverly combining the analogue processing of individual neurons with digital communication through a central communicational hub in the address-event representation [19, 8].

The initial research into neuromorphic computing has since influenced many other approaches for developing neuroinspired hardware. Several neuromorphic chips have been developed [34], such as [86, 120], as well as the larger-scale IBM True North [76], Neurogrid [5] and BrainScaleS [98]. All of these use different levels of abstraction, as well as a different digital/analogue mix for implementing the neural computations. Significant advancements have been made in the neuromorphic vision, allowing for commercial products that use the retinal principles [7, 63]. Recent developments into novel devices such as memristors, together with the incredible rise of artificial neural networks, has directed research into finding ways of using these devices as natural implementations of synapses that would be able to experience plasticity [54, 49]. Future advancements in this direction may lead to intelligent systems that would have learning and adaptation capabilities on the physical level, providing solutions with unparalleled efficiency.

All of the examples show that there has been an ongoing trend of finding novel ways of developing bioinspired hardware. The techniques used do not necessarily strive for accurate biological inspiration, but use bioinspiration to different extent in both analogue and digital approaches. Considering the richness of the neuromorphic techniques [48], we would like to concentrate on the question of finding the right level of abstraction of the neural representation. In the following section, we revisit different methodologies that have been used in neural circuit modelling, and aim to connect them to the feedback outlook that we have discussed in Chapter 2.

3.2 Neuromorphic neurons

One of the main design choices that we face when approaching the development of neuromorphic hardware is finding the right level of abstraction of the neural behaviour [50, 41]. From the detailed compartmental models which aim to capture the morphological details of neurons, to the simplistic integrate-and-fire models which simplify neurons as leaky integrators with a threshold, there is a vast range of different modelling levels that can be used. The choice generally boils down to the trade-off between the biological complexity and the circuit simplicity [48].

Focusing on the concept of neuromodulation and the control of excitability properties we have discussed in Chapter 2, we will broadly classify the different approaches into biophysically detailed models and simplified models, and discuss their capability to capture the dynamical properties of neurons.

3.2.1 Biophysically accurate circuits

The original neuromorphic developments were focused on reproducing the neural biophysical principles using the CMOS device physics, leading to the first implementation of the conductance-based neuron [67]. The approach took several simplifications, but successfully reproduced the conductance-based structure and the essential characteristics of a spiking neuron. Several approaches since have aimed at generating biophysically more accurate models, such as capturing the temporal details of the ion channel dynamics [45, 46, 26], or introducing adaptation mechanisms to the model [106]. In [119], the authors implement a detailed parametrised Hodgkin-Huxley type neuron. Due to the ability to control the many parameters of the model, it can be set up to show different neural behaviours by modifying the form and the dynamics of its ion channel representations [121]. Another implementation of a conductance-based model of the leech heart interneuron was presented in [103] which is able to experience bursting behaviour.

The biggest advantage of these models is that their parameters have biophysical meaning and can come from cell measurements, allowing scientists to directly study the cell behaviour that the models are based on. On the other hand, the drawback of such models comes directly from the nature of the conductance-based models: due to the complex parameter space that they occupy, it is not a trivial task to understand the mechanisms of neuromodulation and the collaborative effect of the parameters. From an engineer's perspective, it also not a straightforward task to choose the appropriate set of ion currents to be modelled in order to achieve a certain set of biological behaviour, as the circuits are tailored for modelling a specific neural type. Finally, the high complexity of conductance-based models compared to some of the simplified mathematical models, leads to the question if neuromorphic implementations of simple models may provide an expansive set of neural behaviour at a lower cost of design and production.

3.2.2 Simplified circuits

On the other side of the complexity range are the simplified models of the neural membrane that have been extensively used in neuromorphic designs, especially when the implementation of larger neural networks is considered. FitzHugh-Nagumo model was one of the first to receive a circuit implementation [79, 56], including a VLSI implementation [62]. Still, the lack of diversity of the neuronal behaviours that it can reproduce, as well as its relative complexity, has led to developments mostly concentrating on different abstractions. One of

the most popular modelling paradigm is the integrate-and-fire modelling, which in the most basic form, consists of a leaky integrator which fires a discrete spike once a certain amount of charge is accumulated at the capacitor [73]. Adaptation mechanism can easily be added to this model, and such circuits have been broadly used [47]. Expanding this methodology in order to model more complex spiking patterns, several models have been introduced, such as the well-known Izhikevich model [52], adaptive exponential integrate-and-fire (AdEx) [9], or the Mihalas-Niebur model [77]. All of these are able to reproduce a rich set of firing patterns in minimal representations, and as such have seen several implementations in the neuromorphic hardware (see e.g. [115, 87] for the Izhikevich model, [1] for the AdEx model, or [28] for the Mihalas-Niebur model). Other approaches have aimed to reproduce the local bifurcation mechanisms [4, 3] that lead to spiking, thus capturing the spike generation dynamics in a minimal sense.

Integrate-and-fire modelling framework provides a powerful way of realising various neural behaviours in simple models that are not difficult to implement in hardware. Still, when studying the effects of neuromodulation and how neural behaviour is shaped through the control of appropriate parameters, they do not provide a clear connection to the biological mechanisms like the detailed biophysical models do. Obtaining a certain behaviour generally requires the fine-tuning of the parameters, and the observed waveform might not have the same robust and tunable mechanisms behind its generation [85]. Capturing the bifurcation mechanisms can lead to the simplified mechanisms of neuromodulation as demonstrated previously [11], but the proposed circuit implementation presented a closed dynamical system which does not provide for a clear interconnection structure for scaling up the design.

3.2.3 Balancing between?

We have presented a brief overview of different modelling approaches present within the neuromorphic engineering community. Looking at the models capable of showcasing the rich neural dynamics that involve several timescales, we find two drawbacks at the two extremes of the modelling spectrum. The biophysically detailed models provide a powerful avenue for studying how the many physiological parameters influence the behaviour, but from an engineer's perspective, suffer from the difficulty of controlling and analysing the complex parameter space in which they live in. Moreover, the incredible diversity of biological ion channels leads to the question of choice of ionic currents to be modelled that would replicate a rich set of neuronal behaviour. On the other hand, simple models can be cheaply synthesised

and may produce an incredibly varied set of neural behaviours, but as analysed in recent work [85], often lack the underlying dynamical mechanisms of detailed models, making them unsuitable for studying how neuromodulation shapes the behaviour.

We have discussed in Chapter 2 how neural excitability and its control are greatly simplified by obtaining a feedback outlook of a neuron, where all ionic currents are classified as contributing to the four essential feedback loops. In order for a neural model to experience robust modulation mechanisms between the different multi-scale firing patterns, it needs to retain these four loops and their modulation in some form. We therefore aim to provide a simplified modelling framework for these loops, which would be able to capture the neuromodulatory processes.

Such an approach is complimentary to the modelling principles described previously in this chapter: by analysing and replicating the modulatory effects of the basic feedback loops, one can gain a better understanding of how modulating the ion channels in a detailed conductance-based model may affect the behaviour, as well as what set of ion channels would be necessary for replicating the spiking/bursting behaviours. On the other hand, it highlights what are the minimal requirements for a simplified model to capture the neuromodulatory mechanisms of neurons.

3.3 Neuromorphic building blocks

In this section we revisit the design principles laid out by Carver Mead and colleagues in their pioneering work [66, 73, 74]. We present the basics of the subthreshold MOSFET design and its advantages compared to the standard above-threshold operation. The basic building blocks of the methodology are discussed: the *transconductance amplifier* which realises a non-linear current-voltage relationship, and the *integrator-follower* circuit, which achieves temporal integration. We describe why these simple circuits provide good building blocks for the I-V curve shaping methodology that we introduce in Chapter 4.

3.3.1 Subthreshold regime

A standard n-channel MOSFET transistor is shown in Fig. 3.1. At the most basic level, we can view a transistor as a three-terminal current source element: the current going between its drain and its source (output current) is controlled by the voltage applied between its

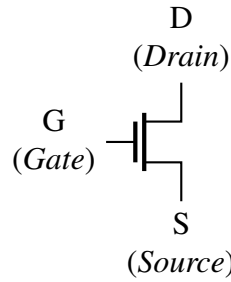


Fig. 3.1: An n-channel MOSFET.

gate and source (input voltage). This can most easily be seen in Fig. 3.2, left: sufficiently increasing v_{ds} saturates the transistor so that the current between its drain and source is mostly independent of the voltage between the two terminals, and can be controlled by varying the voltage at its gate. The transistor does not act as a perfect current source though, apparent from the finite slope of the i_{ds} dependence in the saturated regime.

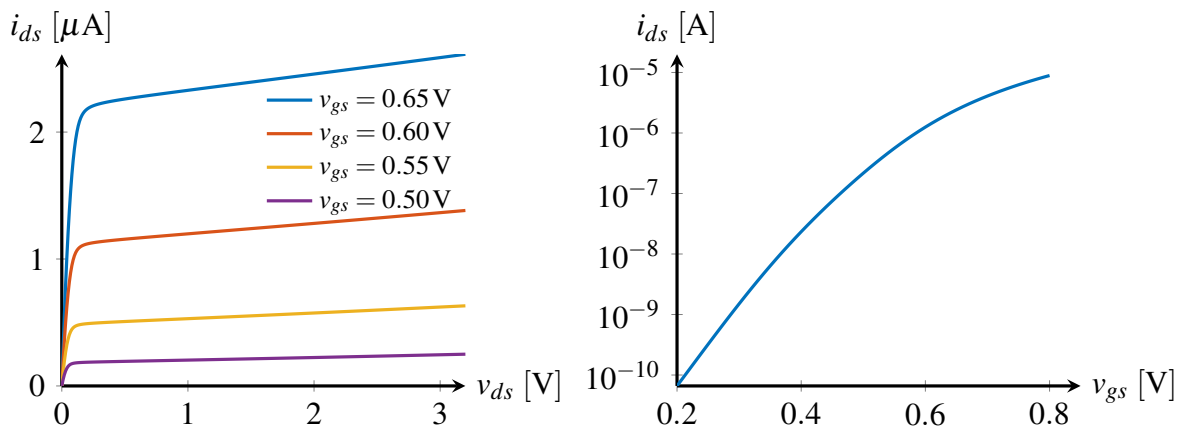


Fig. 3.2: Drain-source current (i_{ds}) as a function of the drain-source voltage (v_{ds}) and the gate-source voltage (v_{gs}). For a large-enough v_{ds} , the current saturates and the MOSFET acts as a current source whose magnitude is mainly controlled by v_{gs} . For small v_{gs} the current exponentially increases with increasing input voltage (subthreshold regime). For a large enough v_{gs} (i.e. above threshold), the exponential dependence turns into a quadratic dependence, and the transistor is commonly considered on.

In traditional electronics, MOSFET is only considered *on* if the input voltage is sufficiently high, disregarding the small output current when the input is below the threshold voltage. In this regime the output current is a quadratic function of the input voltage and the charge is mainly carried by drift. In turn, we concentrate on the *subthreshold* regime where the output current is orders of magnitude smaller and there is an exponential input-output relationship

(Fig. 3.2, right). In this region, the charge is mainly carried by diffusion, and the transistor has the following characteristic:

$$i_{ds} = i_0 e^{\frac{\kappa v_g}{v_T}} e^{\frac{-v_s}{v_T}} \left(1 - e^{\frac{-v_{ds}}{v_T}} \right) \quad (3.1)$$

where i_0 is the zero-bias current, $v_T \approx 25\text{mV}$ is the thermal voltage, and $\kappa \in (0, 1)$ is a process-dependent variable. If we consider grounding the source of the transistor, and the saturated region where $v_{ds} \gg v_T$, then the relationship simplifies to:

$$i_{ds} = i_0 e^{\frac{\kappa v_{gs}}{v_T}} \quad (3.2)$$

so that the output current is purely an exponential function of the input voltage. The transistor has finite output resistance due to the Early effect, which appears in Fig. 3.2, left as the finite slope of the output current in the saturated regime. We often disregard this for most calculations and consider the transistor as a perfect current source controlled by its gate-source voltage, but if the effect is considered it can be modelled as an additional factor added to the Eq. (3.2):

$$i_{ds} = i_0 e^{\frac{\kappa v_{gs}}{v_T}} \left(1 + \frac{v_{ds}}{v_0} \right) \quad (3.3)$$

where v_0 is the Early voltage.

In our work we will be purely considering the MOSFETs in the subthreshold region. There are two main advantages of operating in this regime:

- The voltages and the currents are kept low. This leads to circuits operating with very low power requirements in the order of μWs .
- The exponential input-output relationship is a powerful analogue primitive for synthesising non-linear functions.

In the following section we take a look at the standard transconductance amplifier operating in the subthreshold regime, and show how it leads to a realisation of a basic sigmoidal I-V relationship.

3.3.2 I-V element primitive: Transconductance amplifier circuit

The transconductance amplifier is the essential circuit building block of this dissertation. It generates an output current that depends on the differential input voltage. The schematic of the differential amplifier is shown in Fig. 3.3.

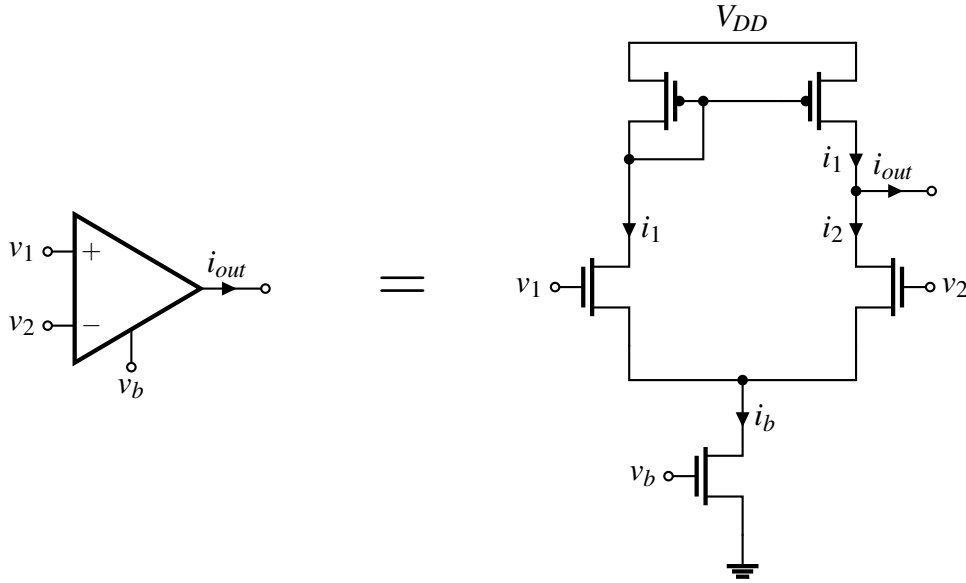


Fig. 3.3: Transconductance amplifier. The circuit realises a hyperbolic tangent mapping from the differential voltage input to the current output. The gain of the function is determined by the current flowing through the base transistor (i_b), controlled by its base voltage (v_b) that acts as the additional amplifier input.

As the transistors are operating in the subthreshold regime, the currents through the input transistors can be found to be the following:

$$i_1 = i_b \frac{1}{1 + e^{\kappa(v_2 - v_1)/v_T}}, \quad i_2 = i_b \frac{1}{1 + e^{\kappa(v_1 - v_2)/v_T}} \quad (3.4)$$

The bottom three transistors of the circuit therefore provide a sigmoidal mapping from the input to the currents i_1 and i_2 . The two top transistors are then used as a current mirror that realises a subtraction of the two currents, so that we obtain the output current:

$$\begin{aligned} i_{out} &= i_1 - i_2 \\ &= i_b \tanh\left(\kappa \frac{v_1 - v_2}{2v_T}\right) \end{aligned} \quad (3.5)$$

The full transconductance amplifier provides a hyperbolic tangent mapping from the differential input to the output current. Its versatility comes from the fact that the gain of the element can be simply controlled by varying the current i_b through the voltage at the base transistor v_b . Since there is an exponential relationship between v_b and i_b , the gain of the element can be easily controlled over several orders of magnitude.

The realisation of the transconductance amplifier shown in Fig. 3.3 has several limitations. The mismatch of transistors in the final circuit design means that the input-output characteristic will not be symmetrical. This mainly manifests as an inherent offset that appears in the Eq. (3.5). Such an offset can be compensated for by appropriately tuning the inputs v_1 or v_2 , but is unknown at the design stage.

Furthermore, since the transistors do not behave as ideal current sources, there are additional limitations that are imposed on the circuit operation. Firstly, the output current can only be supplied in the finite voltage range of the output voltage v_{out} . Secondly, due to the output resistance of the transistors, the supplied i_{out} will have a dependency on the voltage at the output node. These issues can be circumvented easily by limiting the output voltage range in which we are operating.

As the transconductance amplifier provides a controllable I-V characteristic with a limited active voltage range due to its saturation, we will utilise it as a basic element for synthesising nonlinear I-V curves. We also utilise it as a dynamical primitive, as it can be used to construct a nonlinear first-order filter as we show in the following section.

3.3.3 Dynamical primitive: follower-integrator

The time-constants of neuromorphic systems generally require high resistor values in order to align with the frequencies at which biological systems operate. Due to this, using resistors in the standard CMOS processes is generally impractical, and instead, the transconductance amplifier of the previous section can be utilised as a resistive element with variable resistance.

The elementary dynamical circuit that we will utilise is the so-called *follower-integrator* circuit [66, 73]. Essentially, it acts as a first-order filter, where instead of a resistor-capacitor network, the filtering is implemented with a transconductance amplifier connected to a capacitor. This is shown in Fig. 3.4.

The circuit consists of a transconductance amplifier from the previous section, with its negative input and output short circuited, in series with a capacitor. The output voltage is

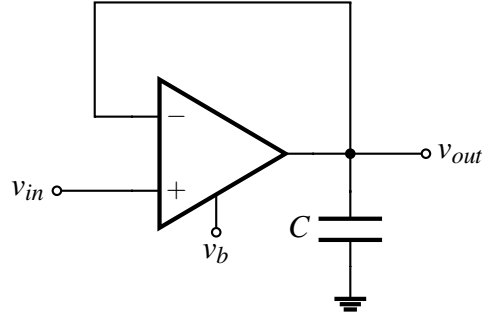


Fig. 3.4: Follower-integrator circuit. The circuit implements nonlinear first-order filtering of the input voltage v_{in} . The time-constant of the filter can be controlled by changing the voltage v_b , which effectively controls the output resistance of the amplifier.

then:

$$C \frac{dv_{out}}{dt} = i_b \tanh \left(\frac{\kappa(v_{in} - v_{out})}{2v_T} \right) \quad (3.6)$$

where i_b is controlled by the base voltage v_b so that $i_b = i_0 e^{\kappa v_b / v_T}$. Although the circuit is non-linear, by considering small changes in voltage we can find the approximate time-constant of the circuit:

$$C \frac{dv_{out}}{dt} \approx \frac{i_b \kappa}{2v_T} (v_{in} - v_{out}) \quad (3.7)$$

defining the time-constant as:

$$T = \frac{2Cv_T}{\kappa i_b} \quad (3.8)$$

As the non-linear nature of the filter does not have a major effect on the temporal characteristics of our proposed model, we will use this circuit as the basic element for temporal filtering.

Appendix 3.A Simulation note

Figure 3.2 was generated with the data from SPICE simulation using the BSIM3 MOSFET model with TSMC 0.35 μm process parameters.

Chapter 4

Neuromodulation through I-V curve shaping

Building from the ideas discussed in Chapters 2 and 3, in the following chapter we present a novel methodology for synthesising neural behaviour. The methodology departs from earlier approaches by rooting the design and analysis in an input-output rather than state-space model of the circuit. We assume the specific circuit architecture common to all voltage-gated conductance-based models of neurophysiology: the excitable membrane is modelled as a passive RC circuit in parallel with (possibly many) circuit elements, each of which controls the circuit conductance in a specific voltage and dynamic range. This architecture is also common to recently introduced low-dimensional model of bursting [29, 30]. By separating the circuit elements in distinct timescales, we propose that shaping the circuit's I-V characteristics in those distinct timescales is modular and sufficient to control the excitability properties of the circuit. The curve shaping methodology maps with surprising ease to the dynamical behaviours of the circuit, and allows us to generalise the intuitive spike-generation mechanisms of the FitzHugh-Nagumo circuit to the more complex neuronal behaviours such as bursting, while also enabling easy modulation between distinct behaviours.

Although the proposed methodology is rooted in the rigorous mathematical analysis of a low-dimensional bursting model [29, 30], the key contribution of this chapter is to present a qualitative approach to tuning the neuronal behaviours which is purely input-output and by-passes the state-space realisation of the circuit for its design and analysis. This is in contrast with recent efforts in designing spiking and bursting feedback circuits from simplified state-space models [33, 11]. Here we directly formulate the task of controlling

a given excitable behaviour as an I-V curve synthesis problem, independent of the circuit implementation specifics. Most importantly, our circuits are inherently neuromodulable as the control of each current element maps to the modulation of a maximal conductance parameter in biophysical conductance-based models [21, 36, 82, 110]. We regard this as an important step towards building neuromorphic circuits with neuromodulation capabilities.

We start by describing the general structure of the neural circuit, relating it to standard examples of excitable circuits such as the FitzHugh-Nagumo model, as well as more recent bursting models. We then define the notion of I-V curves in separate timescales, and describe a simple yet general circuit architecture that allows us to shape the I-V curves through parallel interconnections of basic elements with localised conductance and first-order dynamics. In the following sections, we show how, similarly to the classic FitzHugh-Nagumo circuit, a tunable spiking neuron is realised as an interconnection of the passive membrane, a fast negative conductance element, and a slow positive conductance element. We further show how the interconnection of additional slow negative conductance and ultra-slow positive conductance elements leads to a tunable bursting circuit, mirroring the ionic conductance structure of the bursting neurons [94, 21]. We also compare the bursting mechanism we present with alternative mechanisms studied in neurodynamical models [93]. We show why such mechanisms do not allow for robust control due to their fragile parameter choice requirements.

A graphical interface for simulating the principles of this chapter is described at the end in Appendix 4.A.

4.1 I-V curve shaping by interconnection

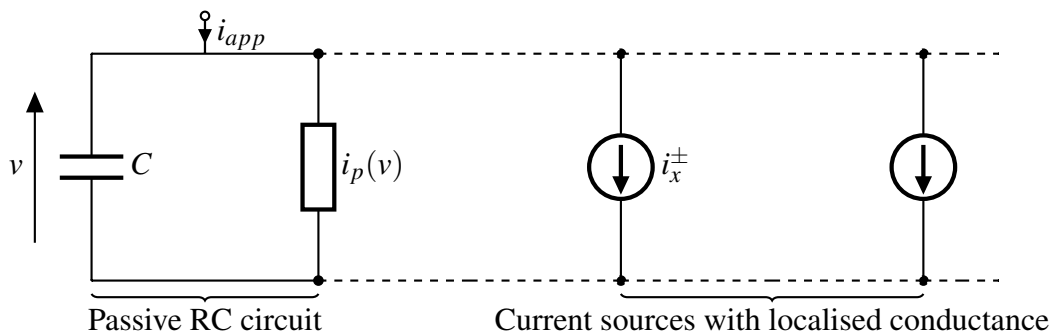


Fig. 4.1: The neural circuit. A passive RC circuit is interconnected with localised conductance current source elements that model the action of the ionic currents.

We base our methodology on the general neural circuit architecture shown in Fig. 4.1. This architecture mirrors the biophysical modelling principles pioneered by Hodgkin and Huxley in their seminal work [43]: an excitable membrane is modelled as the parallel interconnection of a passive RC circuit with several voltage-gated ionic currents (sodium, potassium, calcium, etc.). Here, the passive membrane properties are represented with a membrane capacitor C and a purely resistive element $i_p(v)$, so that its I-V characteristic satisfies:

$$\frac{di_p(v)}{dv} \geq 0, \forall v \quad (4.1)$$

We assume that each voltage-controlled current source obeys the elementary model:

$$i_x^\pm = f_x^\pm(v_x) \quad (4.2a)$$

$$T_x \dot{v}_x = v - v_x \quad (4.2b)$$

so that the output current i_x^\pm has a monotonic dependence on the filtered voltage v_x through the function $f_x^\pm(v)$ that satisfies

$$\frac{df_x^+(v)}{dv} \geq 0, \forall v \quad (4.3)$$

for a positive conductance element, or

$$\frac{df_x^-(v)}{dv} \leq 0, \forall v \quad (4.4)$$

for a negative conductance element. The time constant T_x defines the timescale of the current.

The behaviour of the circuit is then governed simply by Kirchhoff's law:

$$C\dot{v} = -i_p(v) - \sum i_x^\pm + i_{app}, \quad (4.5)$$

and we can define an approximate time constant of the voltage equation:

$$C/T_v = \left. \frac{di_p(v)}{dv} \right|_{v=v_e} \quad (4.6)$$

with the derivative taken around the equilibrium point of the system $v = v_e$. This allows us to consider all time constants relative to the membrane dynamics:

$$\tau_x = T_x/T_v \quad (4.7)$$

In order to describe both bursting and spiking behaviours, it is sufficient to include elements that act on three separate timescales: fast (τ_f), slow (τ_s) and ultra-slow (τ_{us}), for which we assume:

$$\max(\tau_v, \tau_f) \ll \tau_s \ll \tau_{us} \quad (4.8)$$

The dynamics of the fast element relative to the membrane dynamics can be arbitrary, and in particular, the fast dynamics can be taken as instantaneous. We use an instantaneous fast element throughout the simulations in the chapter, corresponding to $\tau_f = 0$.

For modelling purposes, we will consider a dimensionless representation of this circuit architecture. We will denote the dimensionless quantities with capital letters, so that Eqs. (4.2) and (4.5) become:

$$\frac{dV}{d\tau} = -I_p(V) - \sum I_x^\pm + I_{app} \quad (4.9a)$$

$$I_x^\pm = F_x^\pm(V_x) \quad (4.9b)$$

$$\tau_x \frac{dV_x}{d\tau} = V - V_x, \quad (4.9c)$$

with τ being the dimensionless time.

The classic FitzHugh-Nagumo model of excitability assumes this form with the elements:

$$I_p(V) = V^3/3 \quad (4.10a)$$

$$F_f^-(V) = -V \quad (4.10b)$$

$$F_s^+(V) = kV, \quad (4.10c)$$

with $\tau_f = 0$ and $k > 1$. The recent model [30] generalises FitzHugh-Nagumo circuit to allow for a modulation between bursting and spiking behaviours. It can also be presented in this form:

$$I_p(V) = V^3/3 \quad (4.11a)$$

$$F_f^-(V) = -V \quad (4.11b)$$

$$F_s^-(V) + F_s^+(V) = (V + V^*)^2 \quad (4.11c)$$

$$F_{us}^+(V) = V, \quad (4.11d)$$

The bursting behaviour relies on a non-monotonic slow current and an additional ultra-slow current. The parameter V^* controls if the model is spiking or bursting.

Here we will consider those particular circuits as specific interconnections of standardised elements with I-V characteristic

$$F_x^\pm(V) = \pm\alpha_x^\pm \tanh(V_x - \delta_x^\pm). \quad (4.12)$$

Such characteristics retain a fundamental property of biophysical circuits: the conductance has a *localised* activation range, as well as a well-defined timescale. The local range is specified by the linear range of the sigmoid, whereas the timescale is specified by the time constant τ_x . The parameter $\alpha_x^\pm > 0$ controls the gain of the conductance, and the parameter δ_x^\pm determines where in the voltage range the element is active. In addition, we have the passive element taking form of a resistor, so that:

$$I_p(V) = V \quad (4.13)$$

We view the role of localised conductance elements as *shaping* the I-V characteristics of the circuit in distinct timescales. Accordingly, we will consider the I-V characteristics of the circuit in the respective **fast**, **slow**, and **ultra-slow** timescales. Those curves will be denoted by:

$$\mathcal{I}_x = I_p(V) + \sum_{\tau_y \leq \tau_x} F_y^\pm(V), \quad (4.14)$$

so that \mathcal{I}_x represents the summation of all the I-V curves of elements acting on the timescale τ_x , or faster.

The basic rationale of our design will be the following: we will use *negative* conductance elements to create local ranges of negative conductance in a given timescale and *positive* conductance elements to restore the positive conductance in slower timescales. The circuit behaviour will be determined by shaping the local ranges of negative conductance in the right voltage ranges and timescales. Our methodology is obviously qualitative in nature: it does not depend on specific circuit or mathematical realisations but only on shaping the monotonicity properties of the I-V curves in distinct timescales.

4.2 Shaping an excitable circuit

Ever since the early works of Van der Pol [111], Hodgkin and Huxley [43] and FitzHugh and Nagumo [27, 79], the property of excitability of a circuit has been rooted in a region of *negative* conductance in a specific voltage range [99]. As a first step, we briefly revisit this construction with our I-V shaping technique.

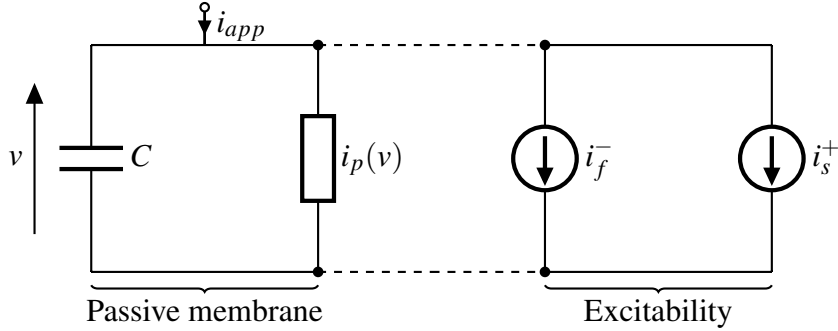


Fig. 4.2: Synthesis of an excitable circuit. Excitable circuit is constructed as the parallel interconnection of a passive membrane with a fast negative conductance element (I_f^-), balanced by a slow positive conductance element (I_s^+).

The excitable circuit in Fig. 4.2 uses two localised conductance elements: a fast negative conductance element I_f^- and a slow positive conductance element I_s^+ . The role of I_f^- is to create a negative conductance range (V_1^f, V_2^f) in the fast I-V curve. The role of I_s^+ is to restore a positive conductance characteristic in the slow I-V curve. The I-V curve shaping is thus determined by the following two conditions:

$$\frac{d\mathcal{I}_f}{dV} < 0, V \in (V_1^f, V_2^f) \quad (4.15)$$

$$\frac{d\mathcal{I}_s}{dV} > 0, \forall V \quad (4.16)$$

which correspond to the graphs illustrated in Fig. 4.3: the passive and slow I-V curves are monotone, whereas the fast I-V curve has the characteristic “N-shape” of a negative conductance circuit¹.

Provided that the timescale separation is sufficient, the resulting dynamical behaviour of the circuit has the following properties:

¹The I-V plots in Fig. 4.3 and throughout the thesis are generated using the simulation data.

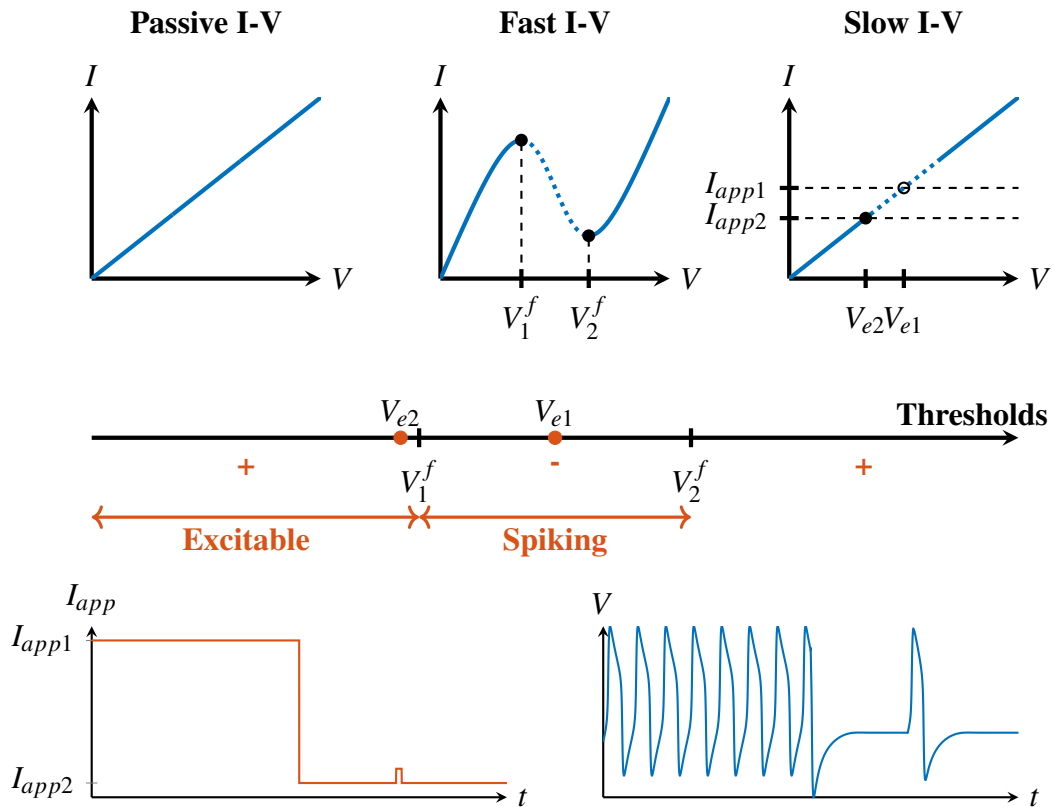


Fig. 4.3: Properties of an excitable circuit. Top: Passive, fast and slow I-V curves of an excitable circuit. The fast curve is “N-shaped”. The slow curve is monotone and its intersection with the line $I = I_{app}$ determines the system’s equilibrium (V_e). The I-V curves share the same voltage axis (V) range, while the current axis (I) range is modified to be between the minimum and the maximum value for each plot. Middle: If the equilibrium voltage lies in the negative conductance region of the fast I-V curve (V_{e1}) the system is spiking, or is excitable otherwise (V_{e2}). Voltage regions are indicated with the sign of the slope of the fast I-V curve. Bottom: Transition between the spiking and excitable regimes through the applied current.

- The circuit has a monotone equilibrium characteristic given by the slow I-V curve. A unique equilibrium (I_{app}, V_e) exists for every value of I_{app} . The equilibrium voltage is stable except in a finite range included in the interval (V_1^f, V_2^f) .
- The circuit has a stable spiking behaviour in a finite range of constant applied current. The spiking behaviour is characterised by a stable limit cycle oscillation with sharp upstrokes and downstrokes between a “low” and a “high” voltage range.
- For equilibrium voltages close to the negative conductance range (V_1^f, V_2^f) , the circuit is excitable: the steady-state behaviour is a stable equilibrium but small current pulses can trigger “spikes”, i.e. a transient manifestation of the oscillatory behaviour.

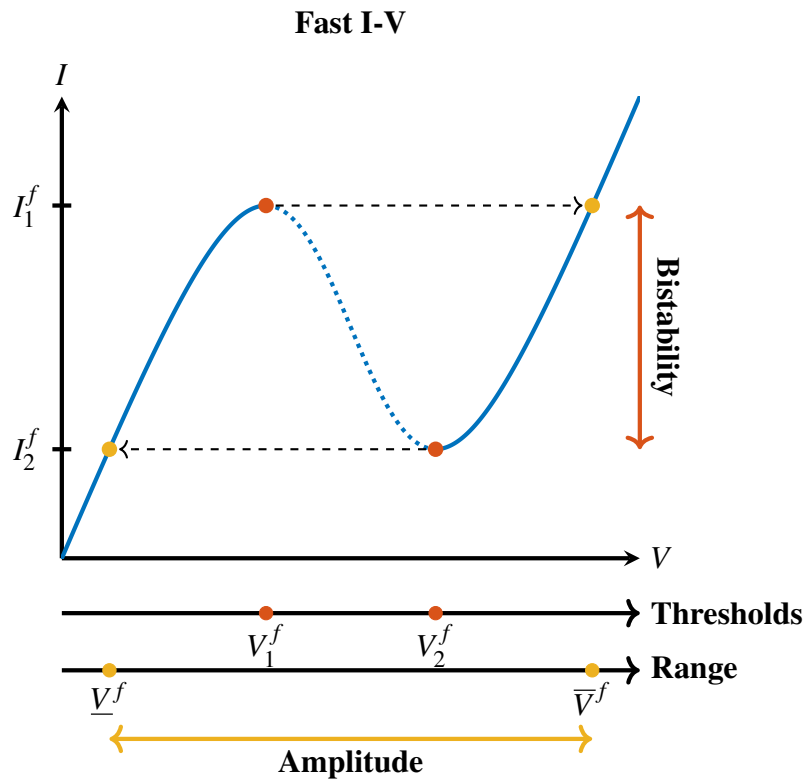


Fig. 4.4: The “N-shaped” fast I-V curve. The threshold voltages V_1^f and V_2^f define the bistable region, so that by increasing the current above I_1^f or decreasing it below I_2^f makes the system jump to the opposite branch of the curve, defined by voltages \bar{V}^f and \underline{V}^f respectively. Controlling the location of these points represents the essential modulation mechanism of the circuit.

The three properties above determine an excitable behaviour [99]. They primarily owe to the fast-slow decomposition of the circuit. In the fast timescale, the negative conductance characteristic makes the circuit bistable and hysteretic: in the range of currents (I_1^f, I_2^f) , two

stable voltage points coexist, so that the behaviour can easily switch between a low voltage state in the range (\underline{V}^f, V_1^f) and a high voltage state in the range (V_2^f, \bar{V}^f) (Fig. 4.4). In the slow timescale, the positive conductance characteristic makes the circuit monostable, resulting in either a stable equilibrium or a stable spiking behaviour.

This analysis is consistent with the biophysics of excitable neurons: sodium channel activation is fast and acts as a negative conductance close to the resting potential, whereas potassium channel activation is slow and acts as a positive conductance.

4.3 Neuromodulating an excitable circuit

Provided a sufficient timescale separation between “fast” and “slow”, the qualitative behaviours of our excitable circuit are solely determined by the I-V curve shaping. Classical dynamical systems tools (see e.g. [53]) show that the unstable voltage range is delineated by two Hopf bifurcations and that the unstable range converges to (V_1^f, V_2^f) as the ratio $\max(\tau_v, \tau_f)/\tau_s$ approaches zero. These asymptotic properties are very convenient to tune the excitable circuit from its fast and slow I-V curves:

- The amplitude range of the spiking behaviour is determined by the hysteresis of the fast I-V curve. With a localised conductance as in Eq. (4.12), the hysteresis is centred around δ_f^- and its range is modulated by the control parameter α_f^- (Fig. 4.5).
- The spiking frequency is determined by the time spent in the low and high voltage range (\underline{V}^f, V_1^f) and (V_2^f, \bar{V}^f) , respectively. For a fixed negative conductance element, this time is primarily modulated by the control parameter α_s^+ (Fig. 4.6, left). The frequency can also be modulated by the applied current (Fig. 4.6, right). The neuron is of Type II in the terminology of [53] because of a non-zero minimal spiking frequency at the Hopf bifurcation.

4.4 Shaping a bursting circuit

Our bursting circuit in Fig. 4.7 closely mimics the architecture of the spiking circuit in the previous section. We view bursting as shaped by two, rather than one, ranges of negative conductance: the first one in the fast timescale, created by I_f^- , and a second one in the

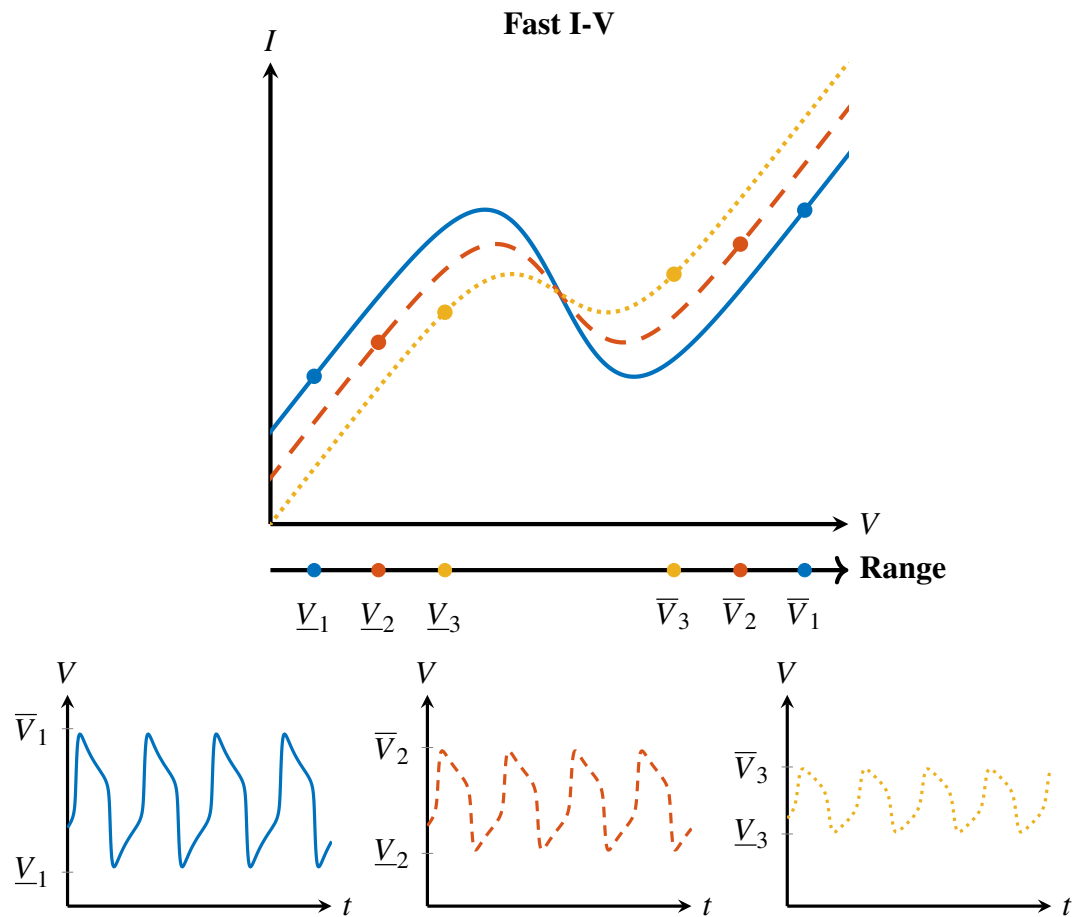


Fig. 4.5: Amplitude of the spikes is determined by the fast I-V curve. The jumps between the low and the high voltage happen at the local maximum and minimum of the curve. Increasing the gain of the fast negative conductance element (α_f^-) widens the negative conductance region and increases the amplitude of the spikes. In order to keep the frequency of the oscillations approximately constant, the gain of the slow positive conductance element is kept the same as the gain of the fast negative conductance in all simulations ($\alpha_s^+ = \alpha_f^-$).

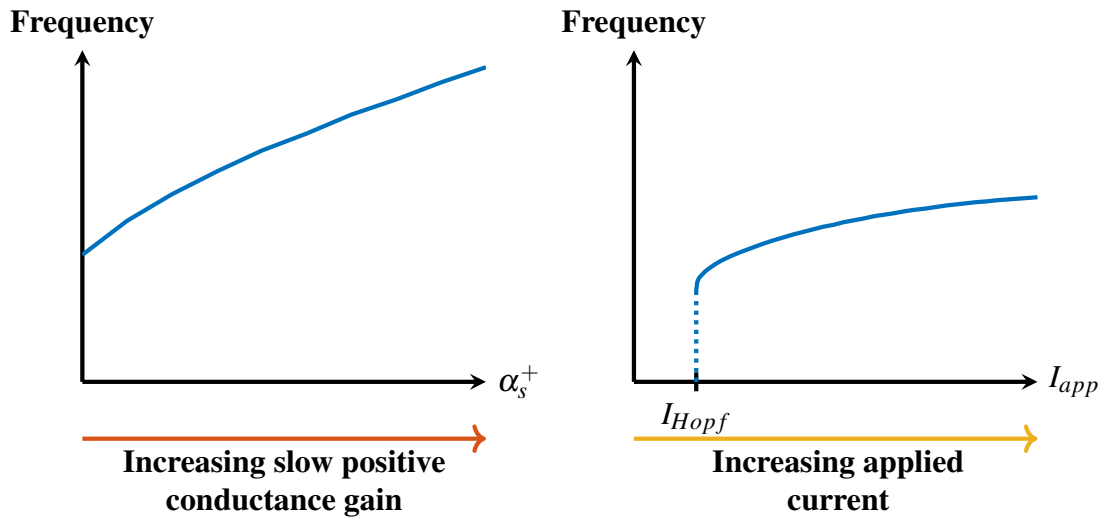


Fig. 4.6: Tuning the frequency of spiking. Left: Frequency of the oscillation can be controlled by varying the slow positive conductance gain (α_s^+). This controls the “up” and “down” time intervals of the spike, which approximately determines the period of oscillation due to the fast nature of the jumps. Right: For fixed α_s^+ , increasing the applied current increases the frequency, but there is a discontinuous jump at I_{Hopf} due to the oscillations emerging through a Hopf bifurcation.

slow timescale, created by I_s^- . The first negative conductance is balanced by a positive conductance I_s^+ in the slow timescale, whereas the slow negative conductance is balanced by a positive conductance I_{us}^+ in the ultra-slow timescale.

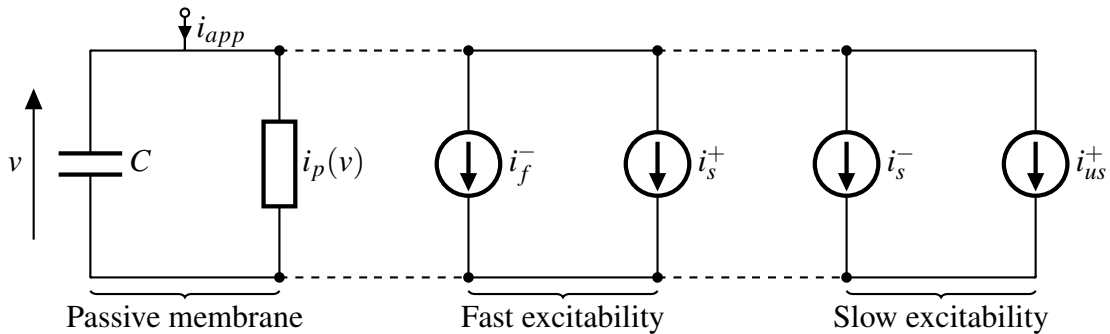


Fig. 4.7: Synthesis of a bursting circuit. Bursting circuit is constructed as the parallel interconnection of a passive membrane with both fast (I_f^-) and slow (I_s^-) negative conductance elements, respectively balanced by slow (I_s^+) and ultra-slow (I_{us}^+) positive conductance elements.

Figure 4.8 illustrates the design of the slow excitable circuit (in the absence of I_f^- and I_s^+) exactly as in the previous section.

Bursting is obtained by shaping the fast and slow I-V curves as illustrated in Fig. 4.9. Each curve has a range of negative conductance and the two ranges overlap in such a way

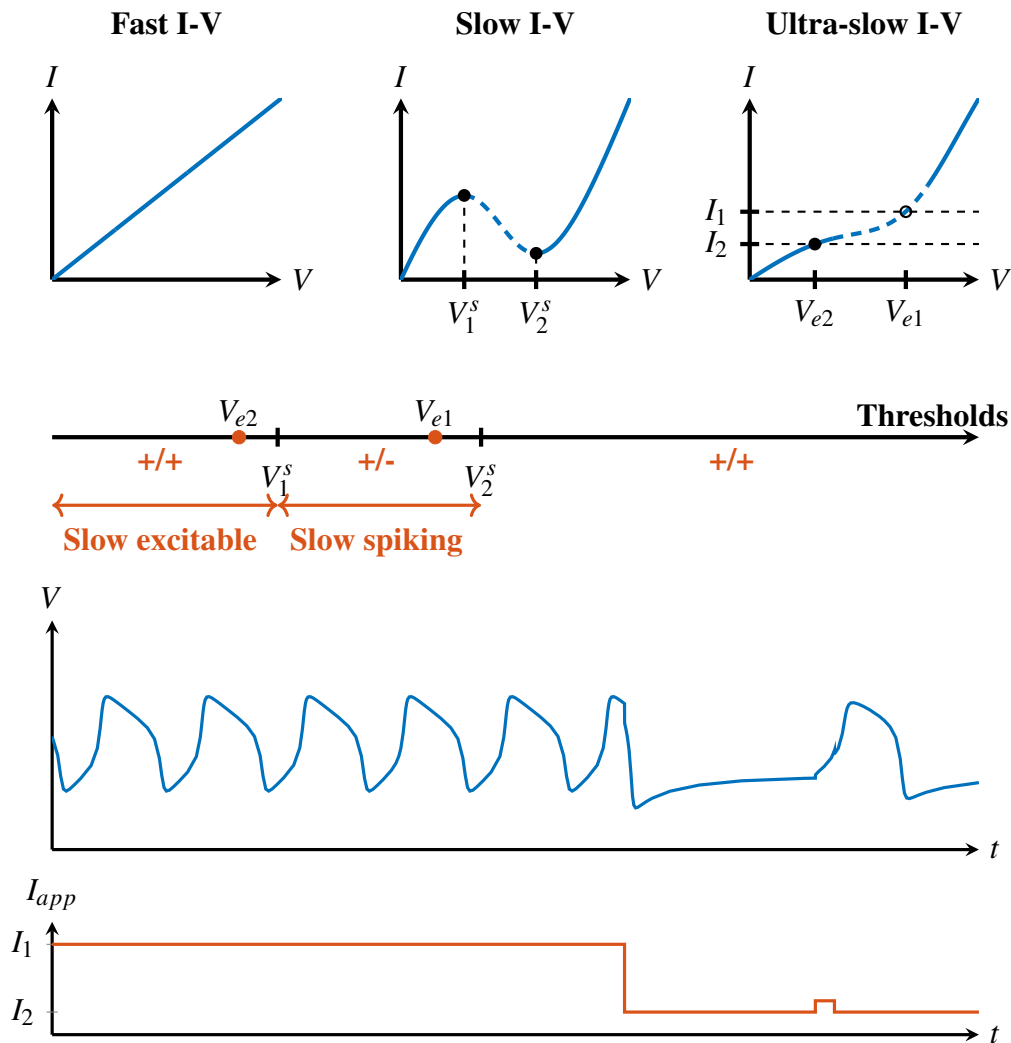


Fig. 4.8: Slow excitable circuit. Without the fast excitability elements, fast I-V curve is monotonic, slow I-V curve is “N-shaped”, and the ultra-slow I-V curve is monotonic, so that the system is slow excitable, similarly to Fig. 4.3. The voltage regions are now indicated with two signs, so that the first sign corresponds to the sign of the slope of the fast I-V curve, and the second sign corresponds to the sign of the slope of the slow I-V curve.

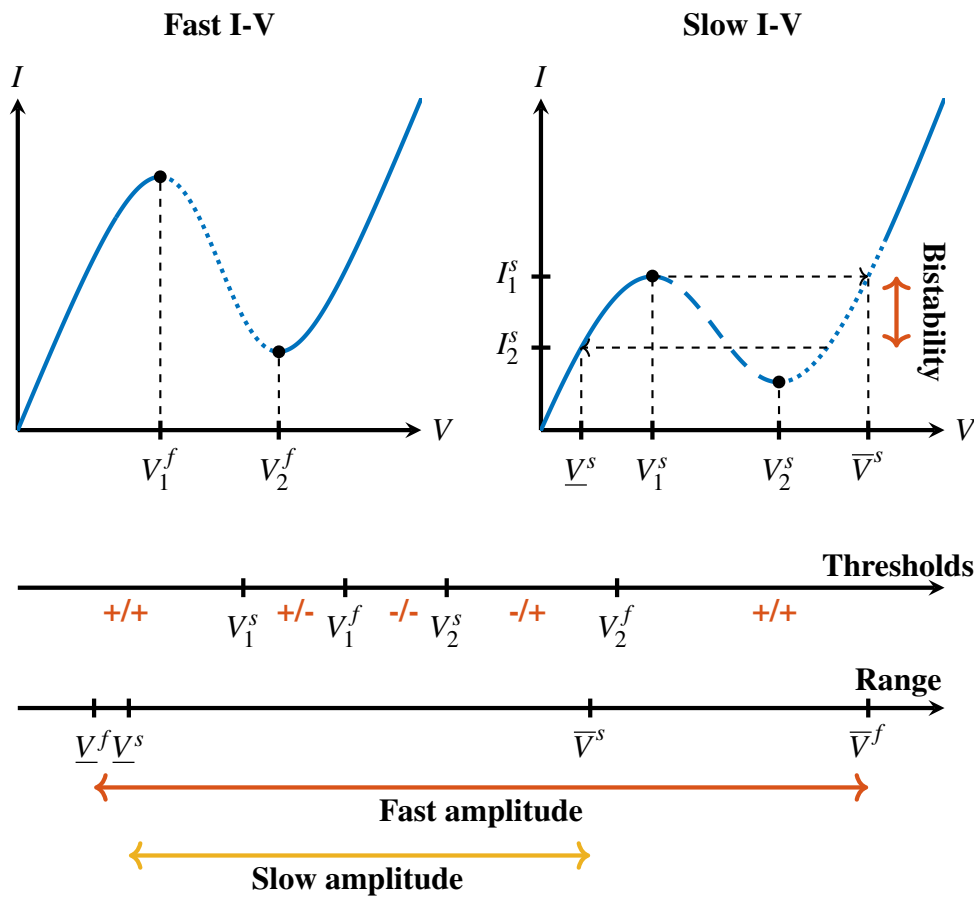


Fig. 4.9: Slow bistability between the rest state and the spiking state. The I-V curves (top) show a system with a double hysteresis: both the fast and the slow I-V curves are “N-shaped”. By having the “up” state of the slow curve correspond to the unstable region of the fast system, the system experiences rest-spike bistability, given that the slow threshold is at lower voltage than the fast one, i.e. $V_1^s < V_1^f$. The system now has two pairs of threshold and range voltages corresponding to the fast and the slow I-V curves, which gives the full set of modulation variables for controlling the behaviour of the circuit.

that

$$V_1^s < V_1^f < V_2^s < V_2^f. \quad (4.17)$$

Finally, the ultra-slow positive conductance element restores monotonicity in the ultra-slow I-V curve, as illustrated in Fig. 4.10. Provided that the timescale separation is sufficient, the resulting dynamical behaviour has the following properties:

- The circuit has a monotone equilibrium characteristic given by the ultra-slow I-V curve.
- Depending on the constant applied current, the circuit has a stable equilibrium (resting state), a stable limit cycle behaviour (spiking), or a stable limit cycle characterised by an alternation of spikes and rest (bursting state).
- Close to the bursting range of applied currents, the circuit is burst excitable. The steady-state behaviour is a stable equilibrium but small current pulses can trigger individual “bursts”, i.e. a transient manifestation of the bursting behaviour.

It is remarkable that those qualitative properties are entirely determined by the shaping of I-V curves as in Fig. 4.10. This owes to the three timescale decomposition of the dynamical behaviours. A detailed analysis in [29, 30] shows that the shaping in Fig. 4.9 is sufficient to enforce bistability in the slow timescale between rest and spiking. The rest-spike bistable range in Fig. 4.9 is analogous to the rest-rest bistable range in Fig. 4.4. It is governed by a transcritical bifurcation at the current I_2^s , as studied in [29, 30] and derived in the Appendix 4.B.

The architecture of the bursting circuit is once again consistent with the biophysics of bursting neurons: the slow negative conductance is provided by the slow activation of calcium ions or the slow inactivation of potassium ions, while calcium-activated potassium channels provide the ultra-slow positive conductance.

4.5 Neuromodulating a bursting circuit

Very much like how the fast I-V curve determined the amplitude of spiking in Fig. 4.5, the fast and slow I-V curves of Fig. 4.9 determine the amplitude tuning of bursting. The gains of the negative conductance elements I_f^- and I_s^- can be modulated to control the amplitude properties of the bursting waveforms. For instance Fig. 4.11 illustrates how moving the

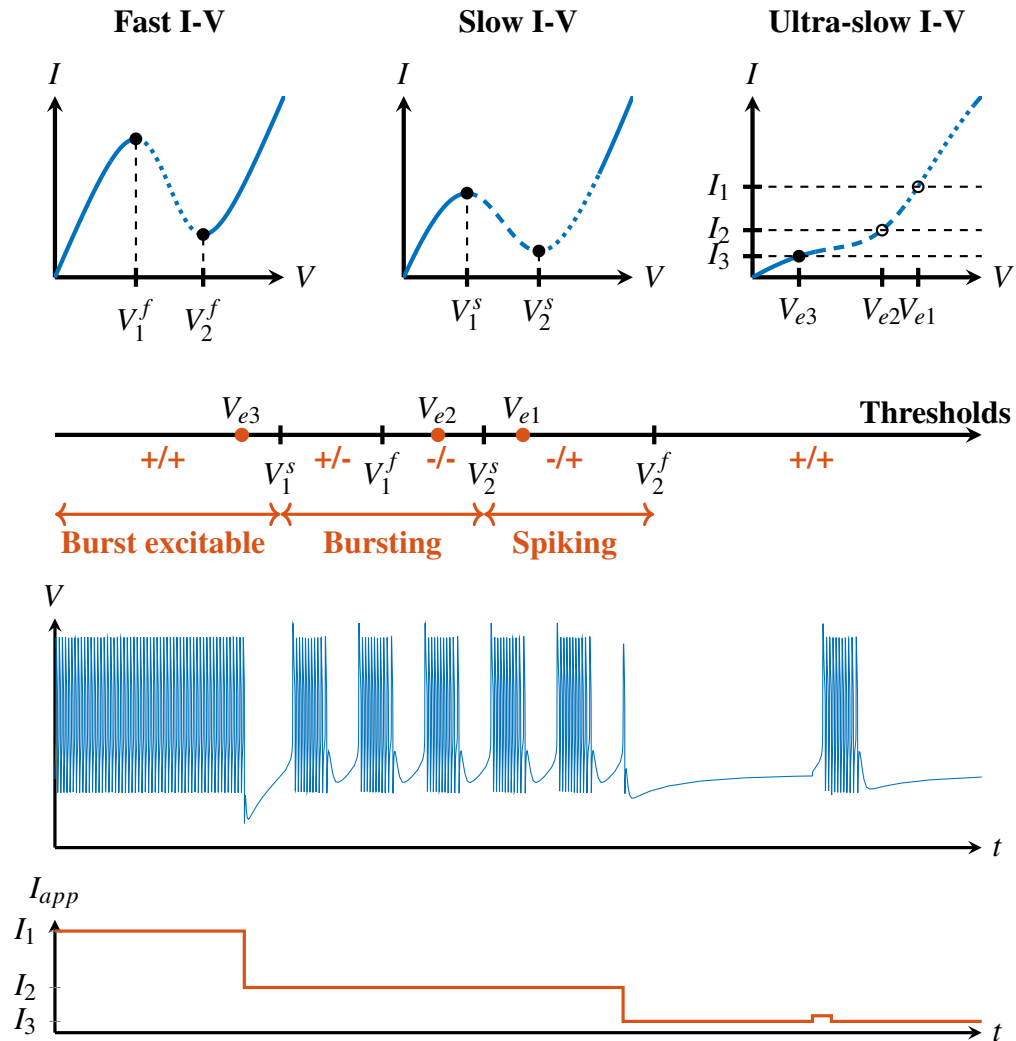


Fig. 4.10: Properties of a bursting circuit. Top: Both fast and slow I-V curves are “N-shaped”. The ultra-slow I-V curve is monotonically increasing, and the intersection with the $I = I_{app}$ line determines the location of the system’s equilibrium V_e . Middle: If the equilibrium voltage lies below the slow threshold, the system is burst excitable (V_{e3}), if the equilibrium lies in the negative conductance region of the slow I-V curve the system is bursting (V_{e2}), while if the system lies in the negative conductance region of the fast I-V curve above V_2^s (V_{e1}), the system is purely fast spiking. Bottom: The transition between the three regimes through I_{app} .

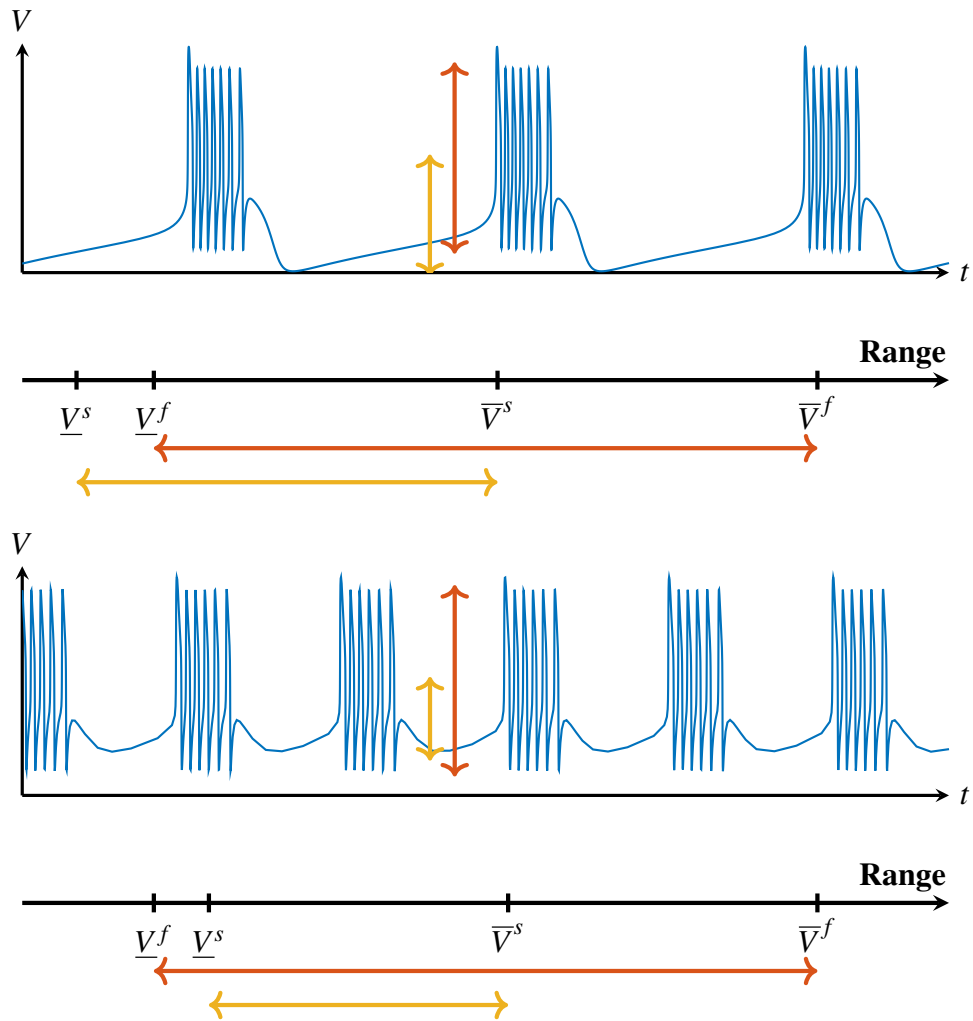


Fig. 4.11: Controlling the bursting waveform. The bursting oscillations can be designed by independently considering the fast and the slow I-V curves, and shaping both fast and slow spiking. In this way we can design plateau oscillations (top) and non-plateau oscillations (bottom), by moving the negative conductance region of the slow I-V curve relative to the the negative conductance region of the fast I-V curve (see Fig. 4.9).

negative conductance regions of the fast and slow I-V curves relative to each other as well as modulating their widths, leads to a transition between plateau and non-plateau bursting.

Likewise, for fixed negative conductance elements, the gains of the positive conductance elements provide natural parameters to control intraburst and interburst frequencies of the bursting attractor (Fig. 4.12).

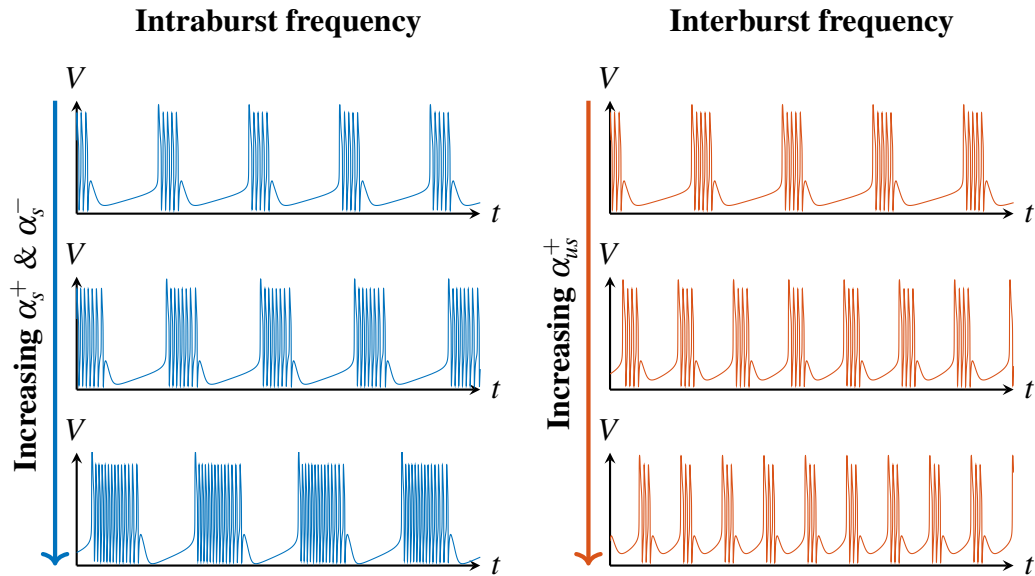


Fig. 4.12: Controlling the intraburst and interburst frequencies of the circuit. Increasing the gain of the slow positive conductance element increases the frequency of the fast spiking, thus increasing the intraburst frequency (left column); the slow negative conductance is increased by the same amount to keep the interburst period approximately constant. Increasing the gain of the ultra-slow positive conductance element increases the frequency of the slow spiking, thus increasing the interburst frequency (right column).

Figures 4.11 and 4.12 illustrate the versatility of our approach and the relevance of tuning a bursting circuit from I-V curves rather than through an exhaustive exploration of the parameter space.

4.5.1 Bursting/spiking modulation through slow I-V curve

Our bursting circuit has a simple parallel architecture with four basic control parameters: two negative conductance gains, α_f^- and α_s^- , and two positive conductance gains α_s^+ and α_{us}^+ . Each negative conductance gain controls one mode of excitability: spiking, a fast excitability mode (α_f^-) and bursting, a slow excitability mode (α_s^-). Each positive conductance gain controls the corresponding frequency: spiking frequency (α_s^+) and bursting frequency (α_{us}^+).

Those control parameters are in close analogy with the maximal conductances of the four typical ionic currents of a bursting neuron: sodium and calcium currents are inward currents whose activation gating variables control the negative conductances. The activation of calcium currents is often five to ten times slower than the activation of a sodium current. Potassium and calcium-activated potassium currents are outward currents whose activation variables control the positive conductances. The activation timescale of potassium and calcium are often similar, whereas the activation of calcium-activated potassium lags behind. See [31] for a further analysis of the physiological conductances of a neuron.

The balance between I_s^- and I_s^+ is particularly important in the modulation of the circuit activity between spiking and bursting. The modulation of this balance shapes the monotonicity of the slow I-V curve: a monotone shape will lead to spiking behavior whereas an “N-shaped” curve will lead to bursting.

Further insight into this regulation is provided by a local analysis of the I-V curves around critical points. This analysis makes contact with singularity theory, that has been the key analysis tool to analyse the modulation of bursting in [30]. We briefly illustrate the value of singularity theory by studying the transition from spiking to bursting around the critical point

$$V = V_1^f = V_1^s, \quad (4.18)$$

obtained by aligning the fast and slow threshold of Fig. 4.9. The concavity of the slow I-V curve around that point locally controls the transition from bursting (locally concave) to spiking (locally convex). The transition is determined by a change of sign in the second derivative:

$$\frac{d^2 \mathcal{J}_s}{dV^2} = 0 \quad (4.19)$$

which, together with Eq. (4.18) determines a pitchfork bifurcation in the fast-slow model [30].

Figure 4.13 illustrates a smooth transition from bursting to tonic spiking around that point. The transition is governed by the modulation of the sole parameter α_s^- . Such a transition is in close analogy with the modulation of calcium currents in the physiologically significant transition from tonic spiking to bursting, see e.g. [72].

The balance between I_s^- and I_s^+ can also be used to control the properties of a purely spiking circuit, as this balance is central to controlling the spiking frequency of a neuron in the low frequency range [24]. Neurons that can spike at arbitrarily low frequency are referred to as Type I excitable neurons. Fig. 4.14 illustrates the classical Type I neuron model

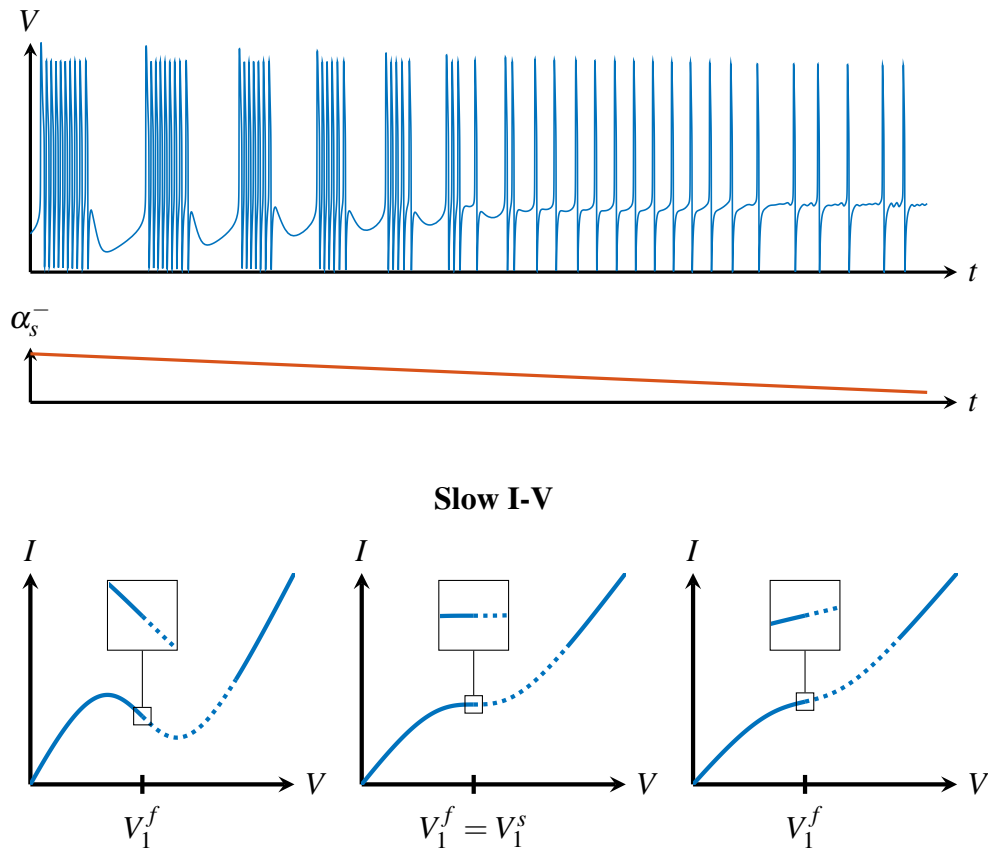


Fig. 4.13: Controlling the oscillation mode. Top: Transition between bursting and regular spiking modes by changing the gain of the slow negative conductance element. Bottom: The transition can be traced locally around the fast threshold V_1^f through the circuit's slow I-V curve (bottom). Starting from a balanced condition (middle), increasing the gain makes the slope locally negative and creates slow bistability (left), while decreasing the gain makes the slow curve monotonic (right). Decreasing the size of the bistable region continuously decreases the number of spikes per burst, changing the behavior into regular spiking when bistability is lost.

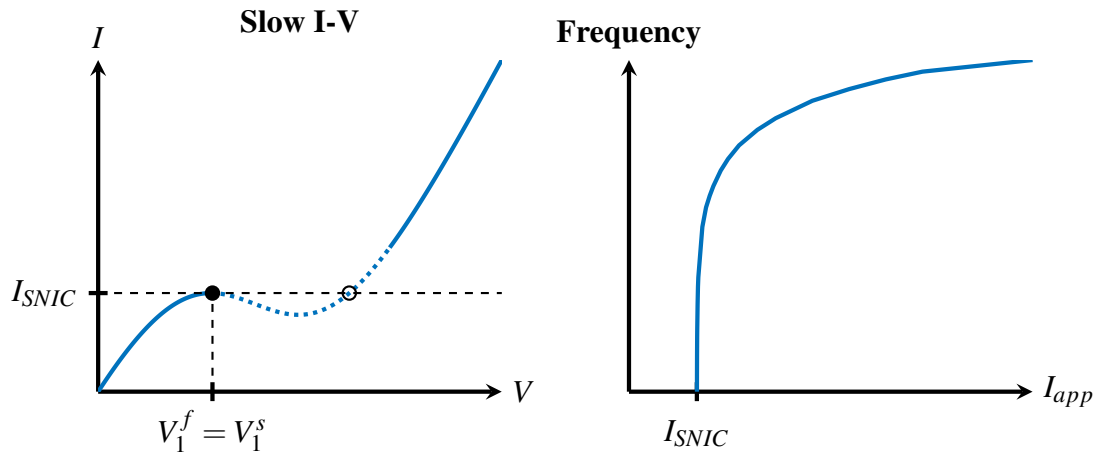


Fig. 4.14: Type I excitable neuron. Left: In order to generate oscillations with arbitrarily low frequency, it is necessary for the slow I-V curve to be non-monotonic, so that for $I_{app} = I_{SNIC}$ the system undergoes a saddle-node on invariant circle bifurcation. The thresholds are set so that the rest/spike bistability is lost, i.e. $V_1^f = V_1^s$. Right: The signature of the saddle-node on invariant circle bifurcation is the frequency of the oscillation tending to zero for I_{app} close to I_{SNIC} .

governed by a SNIC bifurcation [93]. The transition from Type II excitability in Fig. 4.6 to Type I in Fig. 4.14 is achieved by shaping the slow I-V curve around its transition from monotone to “N-shape”, so that V_1^f and V_1^s coincide. In the language of singularity theory, this transition is governed by a hysteresis singularity [30]. In our circuit, shaping an I-V curve around a hysteresis singularity is achieved by balancing a positive and a negative conductance element. This robust regulatory mechanism is central to neuromodulation and can be repeated in any timescale.

4.6 Fragile and rigid bursting mechanisms

Shaping the monotonicity properties of an I-V curve by balancing positive and negative conductance elements makes a bursting circuit robust and controllable [31]. We will now briefly review two well-known bursting mechanisms [92, 93] that do not necessitate a negative conductance element I_s^- . Such models can burst but they lack the modulation properties described in the previous section. Both models have been prevalent in the bursting literature.

The first bursting mechanism is illustrated in Fig. 4.15, in literature often referred to as *elliptic bursting*. The fast and the slow I-V curves are the same as for the purely spiking circuit in Fig. 4.3. However, because the transition from resting to spiking is through a *subcritical* Hopf bifurcation, there exists a small range of applied current in which the system

exhibits bistability between a fixed point and a stable limit cycle, separated by an unstable limit cycle. By introducing the ultra-slow positive conductance element that generates the ultra-slow oscillation between the two states, the system undergoes bursting oscillations.

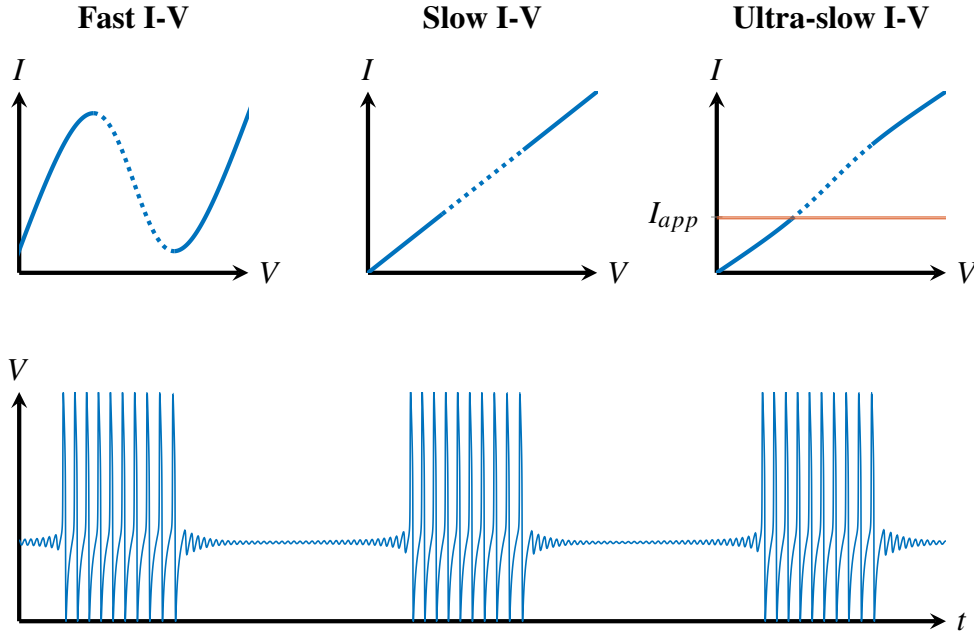


Fig. 4.15: Generating bursting from a Type II neuron. Bursting through a subcritical Hopf bifurcation can be designed by adding an ultra-slow positive conductance element to a spiking circuit. This bursting mechanism is fragile to the time scale separation and only exists for a narrow range of applied current (depicted with the two horizontal lines in the ultra-slow I-V curve).

These bursting oscillations only appear for a small range of values of I_{app} , and in addition to this, it is not possible to precisely determine this range from the ultra-slow I-V curve as before. The bistability range is also sensitive to timescale separation. In fact, it shrinks to zero as the timescale separation is increased [32], unlike the slow bistability discussed in Fig. 4.9, which is robust to an increased timescale separation.

The second bursting mechanism is illustrated in Fig. 4.16. It is achieved by adding the ultra-slow positive conductance element to a Type I neuron. We can construct a Type I neuron without the use of a slow negative conductance element I_s^- by decreasing the linear range of the positive conductance element I_s^+ compared to the fast negative conductance element I_f^- , i.e. by having:

$$I_s^+ = \alpha_s^+ \tanh(\beta_s^+(V_s - \delta_s^+)), \quad \beta_s^+ > 1 \quad (4.20)$$

Although a Type I neuron is monostable (Fig. 4.14), it can be turned into a bistable system if the fast and slow timescales are no longer separated. Such a construction is very sensitive to

the particular choice of timescales, and making the slow timescale slower than approximately $2 \max(\tau_v, \tau_f)$ destroys the bistability. Bursting achieved in this way is shown in Fig. 4.16.

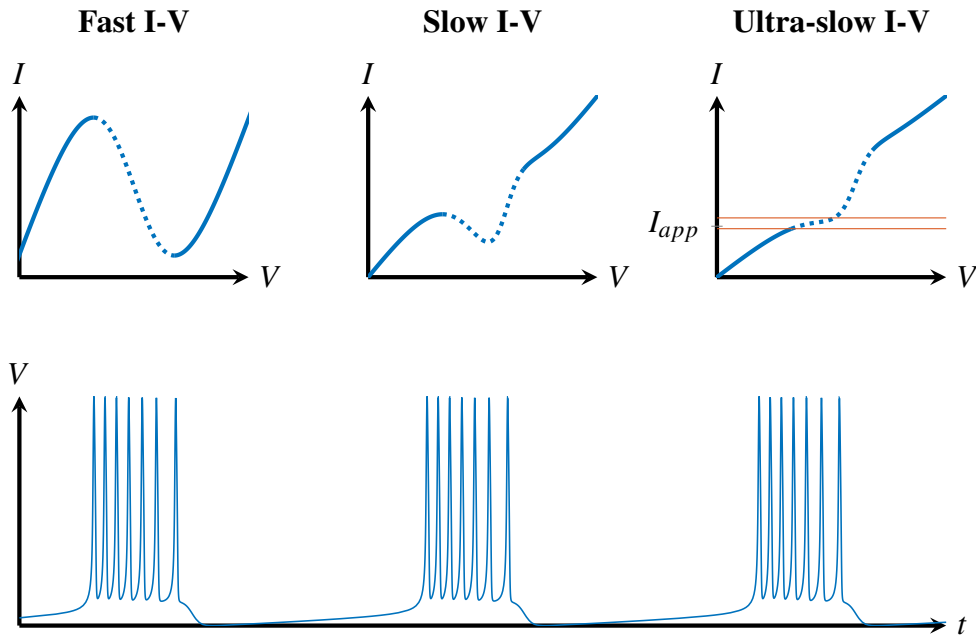


Fig. 4.16: Generating bursting from a Type I neuron. For a small timescale separation between fast and slow, the system can have bistability between resting and spiking, and adding ultra-slow positive conductance element turns it into a bursting circuit. The range of applied currents for which the system undergoes bursting oscillations is depicted with the two horizontal lines in the ultra-slow I-V curve.

The bursting mechanisms illustrated in Figs. 4.15 and 4.16 are not only fragile to parameter uncertainty. They are also rigid in the sense of completely lacking the tuning properties shown in Figs. 4.10 to 4.13; in the first case, the system necessarily undergoes elliptic-type bursts, while the second undergoes plateau bursting oscillations, for which it is not possible to precisely control the height of the plateau, or the size of the fast spikes. The bursting synthesis in the previous sections is in sharp contrast with those mechanisms: the choice of timescales is inessential and all tuning properties can be directly deduced and designed by shaping the I-V curves of the circuit. These alternative constructions underline the value of a bursting circuit realised as the interconnection of both *fast* and *slow* excitability components in order to fully capture the tuning and robustness properties of biological neurons.

Appendix 4.A Graphical interface for I-V curve neuromodulation

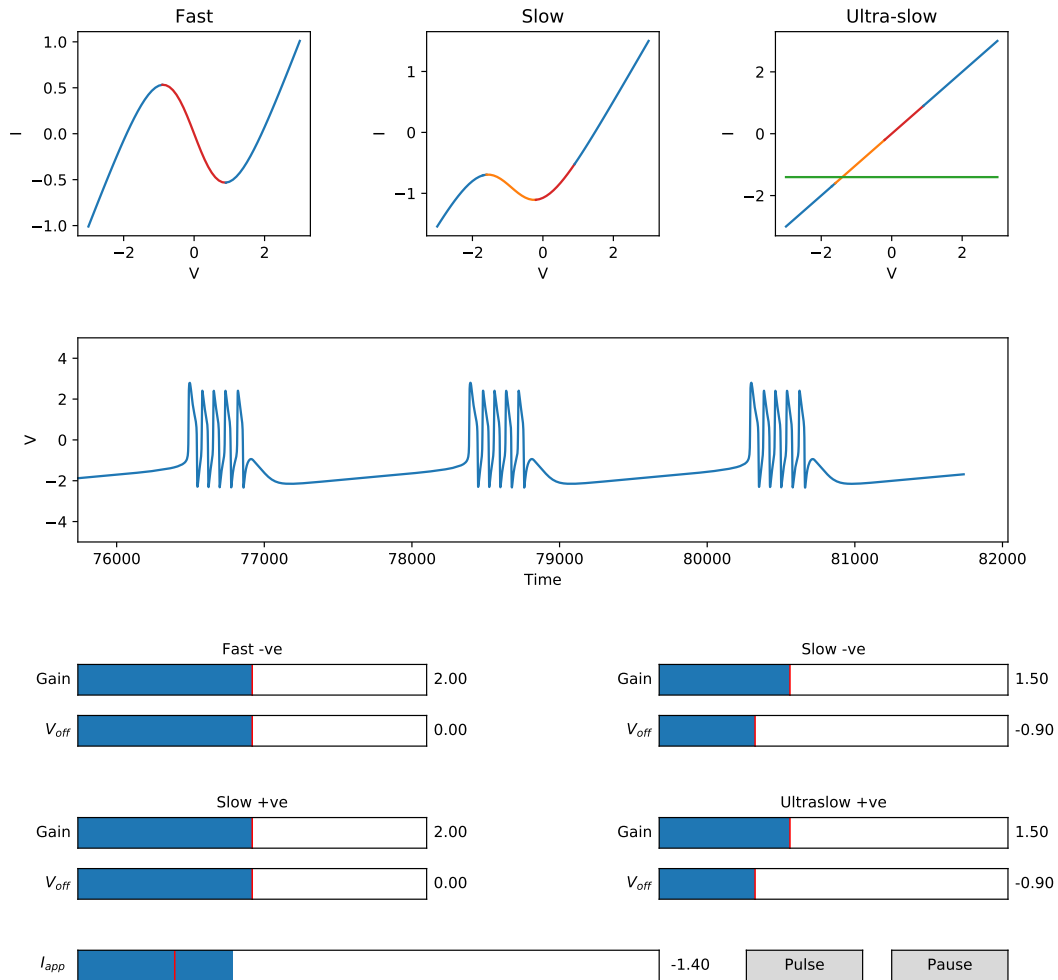


Fig. 4.17: Graphical interface for simulating a single neuron. Top: Fast, slow and ultra-slow I-V curves, where red represents the negative slope region of the fast I-V curve, and yellow represents the negative slope region of the slow I-V curve. The constant green line in the ultra-slow I-V curve is the value of the the applied current I_{app} . Middle: Live voltage trace of the simulation. Bottom: Sliders setting the simulation parameters.

We have developed a simple graphical interface in Python for simulating the neural model presented in Chapter 4 that can be downloaded from <https://github.com/lukaribar/Circuit-Neuromodulation>. The simulation offers a venue for understanding and replicating the results presented in the chapter.

The interface simulates the bursting circuit structure from Fig. 4.7 with the elements modelled as described in Eqs. (4.9), (4.12) and (4.13). The time constants of the simulation are fixed:

$$\tau_f = 0$$

$$\tau_s = 50$$

$$\tau_{us} = 2500$$

Other parameters can be varied through the sliders at the bottom of the graphical window - gain and offset for each of the four currents, as well as the applied current. The middle plot shows the live voltage trace of the simulation, while the top three plots are the current fast, slow and the ultra-slow I-V curves of the circuit. The effect of the parameters on the trace and the I-V curves is plotted instantaneously, so the simulation can be used to study the neuromodulatory properties of the model in an interactive live setting.

The button “Pulse” adds a positive pulse to the applied current of fixed duration and amplitude that can be used to study the excitability properties of the circuit.

Appendix 4.B Transcritical bifurcation in the bursting model

We connect the I-V curve analysis presented in this chapter with previous mathematical analysis of a simplified bursting model [30]. We concentrate on the fast-slow dynamics of the model that has the rest/spike bistability property. The simplified model is the following:

$$\dot{x} = -x^3 + \beta x - (y + \lambda)^2 + \alpha \quad (4.21a)$$

$$\dot{y} = \varepsilon(x - y) \quad (4.21b)$$

with $\varepsilon \ll 1$ so that x is the fast voltage variable, and y is the slow variable.

For a range of parameters, this model experiences bistability between a stable rest state and a stable limit cycle. This is exhibited in the fast-slow phase portrait as a mirrored hysteresis fast nullcline; in the limit of timescale separation, i.e. when $\varepsilon = 0$, the bistability is lost when the two hysteresis branches meet at a transcritical singularity.

The conditions on the I-V curves stated in Fig. 4.9 directly relate our bursting circuit to this model. We will consider the case where $\tau_f = 0$, so that the fast-slow system consists of

two state variables, V and V_s . Firstly, we look at the requirements for the fast I-V curve:

$$I_p(V) + I_f^-(V) = V - \alpha_f^- \tanh(V) \quad (4.22)$$

Without loss of generality, we assume $\delta_f^- = 0$. In order for the fast I-V curve to be “N-shaped”, we require $\alpha_f > 1$; when this is the case, the fast I-V curve is locally equivalent to the instantaneous term in Eq. (4.21) $x^3 - \beta x$, for $\beta \neq 0$, which can be easily verified by checking the first three derivatives around the points $V = 0$ and $x = 0$, respectively.

Because the slow I-V curve is obtained by adding the slow conductance characteristic $I_s(V) = I_s^+(V) + I_s^-(V)$ to the fast I-V curve, we can infer the properties of the slow conductance from the I-V curve conditions. The conditions that the slow I-V curve is “N-shaped” and that $V_1^s < V_1^f$ means that for $V \in (V_1^s, V_1^f)$, the fast I-V curve has a positive slope and the slow I-V curve has a negative slope, and vice-versa for $V \in (V_2^s, V_2^f)$. This means that the slow negative conductance element necessarily has a negative slope in the first region, and a positive slope in the second region, therefore having a local minimum for some $V_*^s \in (V_1^f, V_2^s)$. The characteristic is therefore locally quadratic around the point V_*^s , so that the I-V characteristic of the slow conductance elements is locally equivalent to the quadratic slow term in Eq. (4.21).

This allows us to find the point of the transcritical singularity by having the following conditions on the derivatives of the fast nullcline around the point (V_{tr}, V_{tr}^s) :

$$\left. \frac{\partial \dot{V}}{\partial V} \right|_{V=V_{tr}, V_s=V_{tr}^s} = \left. \frac{\partial \dot{V}}{\partial V_s} \right|_{V=V_{tr}, V_s=V_{tr}^s} = 0 \quad (4.23)$$

Solving Eq. (4.23), we obtain:

$$\left. \frac{d}{dV} \left(I_p^+(V) + I_f^-(V) \right) \right|_{V=V_{tr}} = 0 \quad (4.24a)$$

$$\left. \frac{d}{dV_s} \left(I_s^+(V_s) + I_s^-(V_s) \right) \right|_{V_s=V_{tr}^s} = 0 \quad (4.24b)$$

Following from Eq. (4.24), we get:

$$(V_{tr}, V_{tr}^s) = (V_1^f, V_*^s) \quad (4.25)$$

so that these points correspond to the maximum of the fast I-V curve, and the minimum of the slow conductance I-V characteristic, respectively. We find the corresponding I_{app} by imposing that this point lies on the fast nullcline, so that finally:

$$I_2^s = I_p^+(V_1^f) + I_f^-(V_1^f) + I_s^+(V_*^s) + I_s^-(V_*^s) \quad (4.26)$$

Appendix 4.C Simulation parameters

All simulations in this chapter were carried out in MATLAB.

Figures 4.3, 4.5, 4.6, 4.8 and 4.10 to 4.15 use the model described in Eqs. (4.9), (4.12) and (4.13).

The parameters for each conductance element are given in Table 4.1, as well as the applied currents. Common parameters for these figures are the following:

$$\begin{aligned} \tau_f &= 0 \\ \tau_s &= 50 \\ \tau_{us} &= 2500 \\ \delta_f^- &= \delta_s^+ = 0 \end{aligned}$$

In Fig. 4.16 the slow timescale is modified to $\tau_s = 2$, and the model described in Eq. (4.20) is used for the slow positive conductance. The parameters are the following:

$$\alpha_f^- = 2, \delta_f^- = 0, \alpha_s^+ = 1, \beta_s^+ = 3, \delta_s^+ = 0.5, \alpha_{us}^+ = 1, \delta_{us}^+ = 0, I_{app} = -1.1$$

Table 4.1: Parameter values for simulations in Chapter 4

Figure	α_f^-	α_s^+	α_s^-	δ_s^-	α_{us}^+	δ_{us}^+	I_{app}
4.3	2	2	/	/	/	/	0, -1
4.5 (solid)	2.5	2.5	/	/	/	/	0
4.5 (dashed)	2	2	/	/	/	/	0
4.5 (dotted)	1.5	1.5	/	/	/	/	0
4.6 (left)	2	[2,4]	/	/	/	/	-0.8
4.6 (right)	2	2	/	/	/	/	[-1,-0.2]
4.8	0	0	1.5	-0.88	2	0	-2, -2.6
4.10	2	2	1.5	-0.88	2	0	-1, -2, -2.6
4.11 (top)	2	2	1.5	-1.5	1.5	-1.5	-2
4.11 (bottom)	2	2	1.3	-1	1.3	-1	-1
4.12 (top, left)	2	2	1.5	-0.88	1.5	-0.88	-1.3
4.12 (middle, left)	2	2.2	1.65	-0.88	1.5	-0.88	-1.3
4.12 (bottom, left)	2	2.6	1.95	-0.88	1.5	-0.88	-1.3
4.12 (top, right)	2	2	1.5	-0.88	1.5	-0.88	-1.3
4.12 (middle, right)	2	2	1.5	-0.88	2.5	-0.88	-1.3
4.12 (bottom, right)	2	2	1.5	-0.88	3.5	-0.88	-1.3
4.13	2	2	[0.8,1.6]	-0.88	2	0	-2.2
4.14	2	2	1.2	-0.45	/	/	[-0.4,-0.3]
4.15	2	2	/	/	0.5	0	-1.2

Chapter 5

Circuit design

In Chapter 4 we have presented a methodology for designing and controlling neuronal behaviours by shaping the neuron's I-V curves in several timescales. The central premise of the approach is that the control of neuronal properties is translated into generating and shaping regions of negative conductance that in turn control the underlying oscillatory properties. To this end, the approach of Chapter 4 assumes the employment of first-order filters to set the timescales, and elementary elements with a localised bell-shaped conductance characteristic to shape the I-V curves.

The transconductance amplifier circuit operating in the subthreshold regime that we discuss in Chapter 3 is a natural implementation of such an element, due to its well-defined sigmoidal input-output relationship, and the capability of dynamically controlling its gain. We utilise the transconductance amplifier in all parts of the circuit, including the passive component and the first-order filters. The design thus purely reduces to the implementation and interconnection of these basic elements. We start by describing the properties of this implementation, and present simulation results of the circuit using the TSMC 0.35 μm technology parameters. We discuss how variations in the MOSFET parameters affect the I-V curves, and how such variations are compensated for by varying the circuit's control variables. The effect of temperature on the circuit's output is also considered.

We follow the discussion of the simulation by presenting the implementation of a proof-of-concept circuit that uses off-the-shelf discrete components. The simplistic implementation shows the robustness of the approach of Chapter 4, as well as the ease of its neuromodulation through the several voltages determining the gains of the feedback elements.

5.1 Circuit elements

5.1.1 Implementation of a localised conductance element

We propose a simple hardware implementation of an element that satisfies Eq. (4.2) and has the I-V characteristic as in Eq. (4.12), as shown in Fig. 5.1. The first-part of the circuit is the follower-integrator circuit as described in Section 3.3.3, followed by a single transconductance amplifier with the hyperbolic tangent input-output relationship (Section 3.3.2). The conductance element has the following characteristic:

$$i_x^\pm = \pm (i_b)_x^\pm \tanh\left(\kappa \frac{v_x - (v_\delta)_x^\pm}{2v_T}\right) \quad (5.1a)$$

$$C_{T_x} \dot{v}_x = i_{T_x} \tanh\left(\kappa \frac{v - v_x}{2v_T}\right) \quad (5.1b)$$

Its effective timescale is determined by the capacitance (C_{T_x}) and the base current (i_{T_x}), so that

$$T_x = (2v_T C_{T_x}) / (\kappa i_{T_x}) \quad (5.2)$$

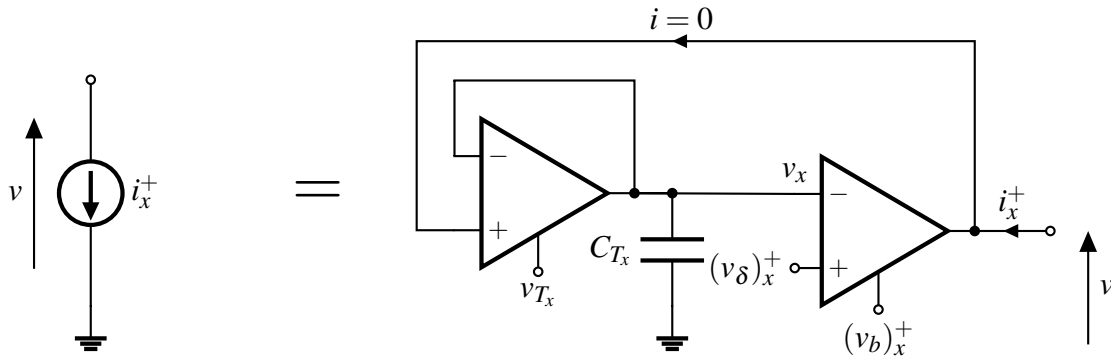


Fig. 5.1: Implementation of a localised conductance element. The first transconductance amplifier and a capacitor form a non-linear first-order filter, whose output is the filtered voltage v_x . This is then the input to the second transconductance amplifier which forms the output current i_x^+ . The element in this case is positive conductance (for a negative conductance element the inputs to the second amplifier are swapped).

The current source acts as a positive conductance when the filtered voltage is connected to the negative input terminal, as in Fig. 5.1. Instead, it acts as a negative conductance element if it is connected to the positive input terminal. The other terminal then defines the voltage offset, by default set to the middle of the voltage rails.

We map the dimensionless parameters from previous sections directly to the circuit parameters in the following way:

$$(i_b)_x^\pm = \alpha_x^\pm \left(\frac{2Gv_T}{\kappa} \right) \quad (5.3a)$$

$$(v_\delta)_x^\pm = \delta_x^\pm \left(\frac{2v_T}{\kappa} \right) \quad (5.3b)$$

$$i_{app} = I_{app} \left(\frac{2Gv_T}{\kappa} \right), \quad (5.3c)$$

with G being the conductance of the passive element around equilibrium, i.e.:

$$G = \left. \frac{di_p(v)}{dv} \right|_{v=v_e} \quad (5.4)$$

This conductance then defines the time constant of the voltage equation as in Eq. (4.6):

$$T_v = \frac{C}{G} \quad (5.5)$$

5.1.2 Implementation of the passive element

For the passive element $i_p(v)$, we utilise a linearised version of the standard transconductance amplifier. We increase the linear region of the amplifier by using the standard technique of source degeneration. The main idea is to effectively increase linearity by introducing a negative feedback loop: the output current is converted into a voltage and then subtracted from the input. This is done by introducing a resistive device at the source nodes of the input transistors: an increase in current through a transistor leads to an increase in the voltage across the resistive element, in turn decreasing the gate-source voltage of the transistor and thus stabilising the output current. We add two transistors with gate and drain shorted on each input side to act as resistive elements (Fig. 5.2). This leads to a new input-output relationship (derivation in Appendix 5.A):

$$i_{out} = i_b \tanh \left(\kappa_l \frac{v_1 - v_2}{2v_T} \right) \quad (5.6)$$

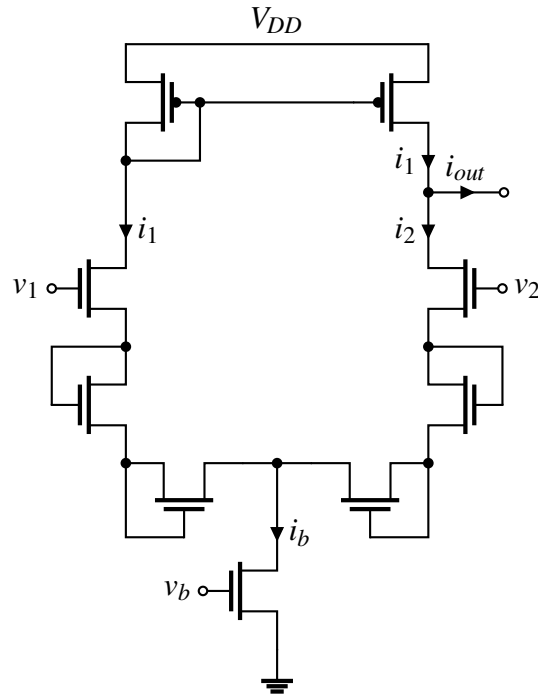


Fig. 5.2: Linearised transconductance amplifier. The two additional transistors in each differential branch add negative feedback through source degeneration, increasing the linear region of operation of the amplifier.

Comparing to the regular transconductance amplifier (Eq. (3.5)), the increase in linear region is determined by the ratio κ/κ_l :

$$\frac{\kappa}{\kappa_l} = \frac{\kappa^2 + \kappa + 1}{\kappa^2} \quad (5.7)$$

The ratio depends on the value of κ , but the linear region is necessarily increased as $\kappa < 1$. For the parameters used in the simulation, the comparison between the standard and the linearised amplifier's input-output relationships is shown in Fig. 5.3.

We have found this simplistic linearisation technique to be adequate for the purpose of designing a passive element for the neural circuit. Different techniques could alternatively be utilised to improve the linearity of the element [35, 97, 96, 17], and thus, the correspondence to the simulations from Chapter 4.

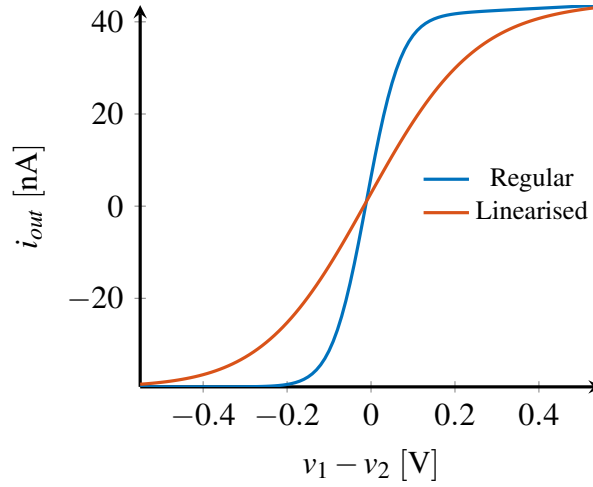


Fig. 5.3: Comparison of input-output characteristics of the regular and linearised transconductance amplifiers.

5.2 SPICE simulation

We have simulated the circuit in SPICE environment, using the BSIM3 MOSFET model with TSMC 0.35 μm process parameters and a 3.3 V voltage supply.

Each current source element of the bursting circuit from Fig. 4.7 is realised as described in the previous section. Note that since currents i_s^- and i_s^+ both act on the slow timescale, only one filter is necessary.

All capacitors were chosen to have the same capacitance $C = 100\text{pF}$, and G was set so that the period of the oscillation is of the order of seconds. We achieve this by setting:

$$T_{us} = 1\text{ s} = 50 T_s = 50^2 T_v \quad (5.8)$$

The input transistors and the source degeneration transistors were chosen to have the minimal size, so that their width and length were set to $W = 0.6\mu\text{m}$ and $L = 0.4\mu\text{m}$. The bias transistors and the current mirror transistors were made larger in order to minimise the channel length modulation effect and improve matching, so that a more precise tanh current-voltage relationship is obtained. Their size was chosen to be $W = 2.4\mu\text{m}$ and $L = 1.6\mu\text{m}$.

By using the relationships given in Eq. (5.3) we can set the parameters of the circuit to replicate any behaviour demonstrated in the previous sections. As an example, we concentrate on the transition from bursting to spiking from Section 4.5.1 (Fig. 4.13). We recreate this

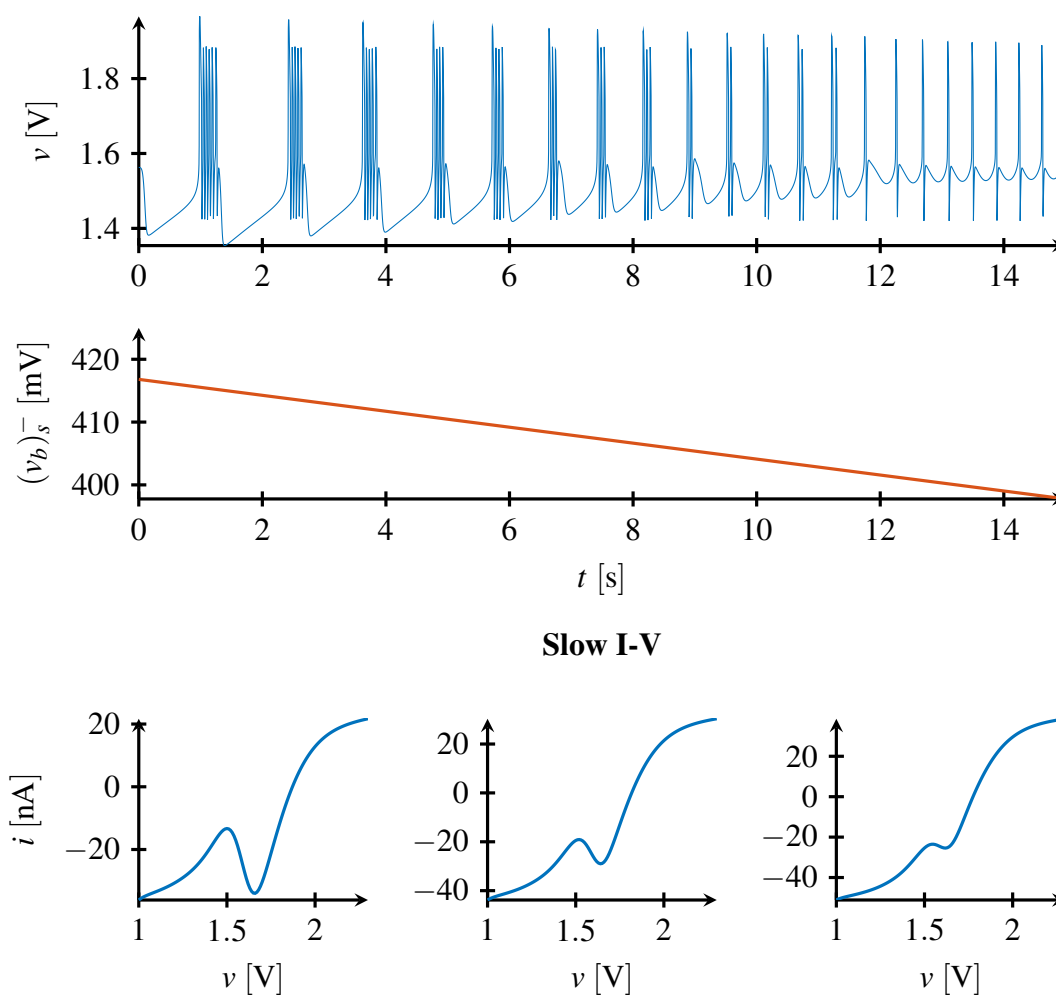


Fig. 5.4: Transition between bursting and spiking modes in the SPICE circuit simulation. The gain of the slow negative conductance element is controlled through the corresponding base voltage that modifies the gain of the current element i_s^- . Decreasing i_s^- reduced the negative conductance region of the slow I-V curve, changing the behaviour from bursting to spiking.

transition in Fig. 5.4. The transition is controlled by the parameter α_s^- , which in the circuit corresponds to the base current $(i_b)_s^-$ of the i_s^- localised conductance element. Due to the non-linearity of the passive element, the bursts have a slightly larger amplitude of the slow oscillation for high values of $(v_b)_s^-$ as seen in the figure, but we observe exactly the same transition as the negative conductance region of the slow I-V curve is modulated.

The simulated power consumption of the circuit is $0.77 \mu\text{W}$ in the bursting regime.

5.3 Robustness of I-V curve shaping

Due to manufacturing uncertainty, the parameters of the circuit will vary from the idealistic conditions of the previous section. To this extent, we would like to stress two important characteristics of our proposed architecture:

1. Maintaining the I-V curves of the circuit keeps the behaviour intact.
2. The circuit's I-V curves can be fully controlled through the gain and offset voltages of the localised conductance elements.

The first point effectively means that the underlying circuit structure is inessential: as long as the input-output characteristic of the circuit consists of a specific set of I-V curves, its behaviour is well-defined. Robustness of the circuit behaviour therefore boils down to the robustness of its I-V curves.

The second point stresses that the internal parameters of the circuit can be readjusted so that the set of I-V curves is kept constant. This means that the variability in the components can be compensated for by tuning the control voltages of the circuit elements.

To show this, we have investigated how process variability affects the I-V relationships of the circuit elements by varying the following process parameters: threshold voltage, surface mobility at the nominal temperature, gate oxide thickness, and transistor width and length offset parameters. For each parameter, the variability was modelled as a Gaussian distribution around the nominal value with the standard deviation at 10% of the nominal value.

The main effect of these process variations on the I-V characteristics of the elements was found to be the variation in the gains of the localised conductance elements, while the shape of the tanh relationships remained largely unchanged. As a result, such variations can be compensated for by readjusting the base voltages controlling the element gains (v_b in

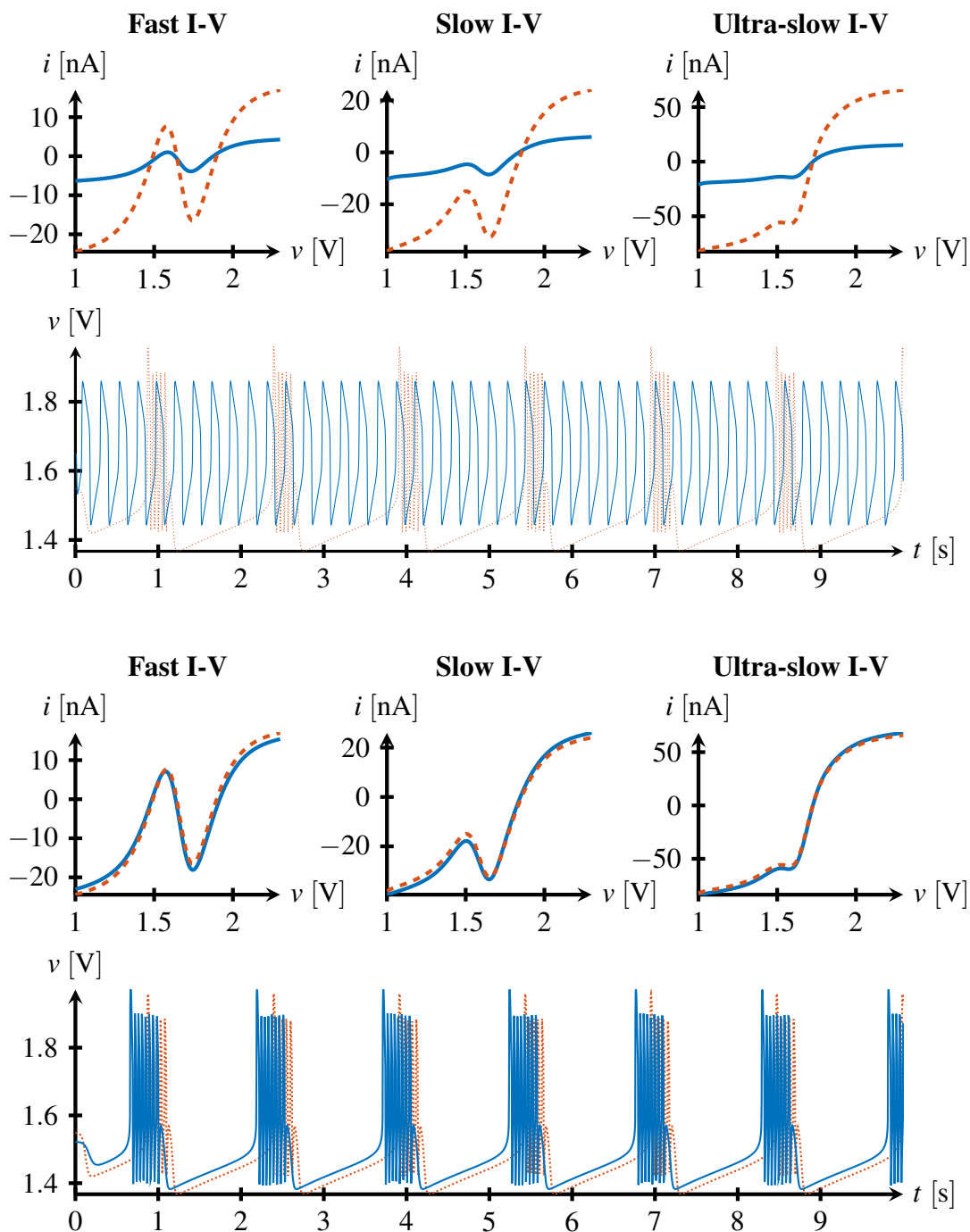


Fig. 5.5: Compensating for process variation. The element gains of a circuit instance differing from the nominal can be adjusted so that the I-V curves are restored and the behaviour is kept the same. Top: Due to process variation, the I-V curves of the circuit (blue, solid) are distorted compared to the nominal (orange, dashed), and the bursting behaviour is lost. Bottom: After compensation, the circuit's I-V curves closely match the nominal I-V curves, and the bursting behaviour is restored.

Fig. 3.3). We show this on a random instance of the circuit in Fig. 5.5: for nominal values the bursting behaviour is lost, but by rescaling the element gains the I-V curves are restored, and therefore, the nominal behaviour. The local transistor mismatches introduce voltage offsets in the tanh I-V relationships [103], and such variations are compensated for through the control of offset voltages of the circuit elements (v_1 or v_2 in Fig. 3.3).

We also consider how temperature variations affect the behaviour of the circuit. In Fig. 5.6 we can see that the circuit maintains the bursting behaviour for changing temperature, while the interburst frequency increases with increasing temperature. Such a dependence on temperature is in correspondence with the common behaviour of biological neurons [91].

In order to account for the variability in circuit components as well as temperature variations, additional compensation techniques can be considered that would allow the circuit to automatically maintain its behaviour irrespective of the changing conditions (see e.g. [106]). As we have discussed in this section, the aim of such techniques would be to maintain the circuit's input-output properties in the form of its I-V curves, so that the behaviour is subsequently preserved.

5.4 Hardware implementation

We have realised a proof of concept circuit implementation of the architecture in order to test the feasibility of the design and the proposed control principles. The focus is on showcasing the modulatory capabilities of the model as discussed in Chapter 4 in a concrete hardware realisation. The parameters of the circuit such as the time-constants differ from the simulations of the previous sections, but the I-V curve neuromodulation principles are exactly the same.

For this realisation we have only used off-the-shelf components, in contrast to the the SPICE simulations that were conducted using the TSMC 0.35 μm process parameters. We have used the transistor array packages ALD210808 and ALD1107 for the NMOS and PMOS respectively, each containing four transistors per component. For the passive element $I_p(V)$ we have used a fixed 10 k Ω resistor instead of the linearised transconductance amplifier of Fig. 5.2. The gain of each localised conductance element is controlled by a corresponding gate voltage, and the offsets through the corresponding voltage input to the transconductance amplifiers. All of the control voltages were generated using voltage dividers. The circuit

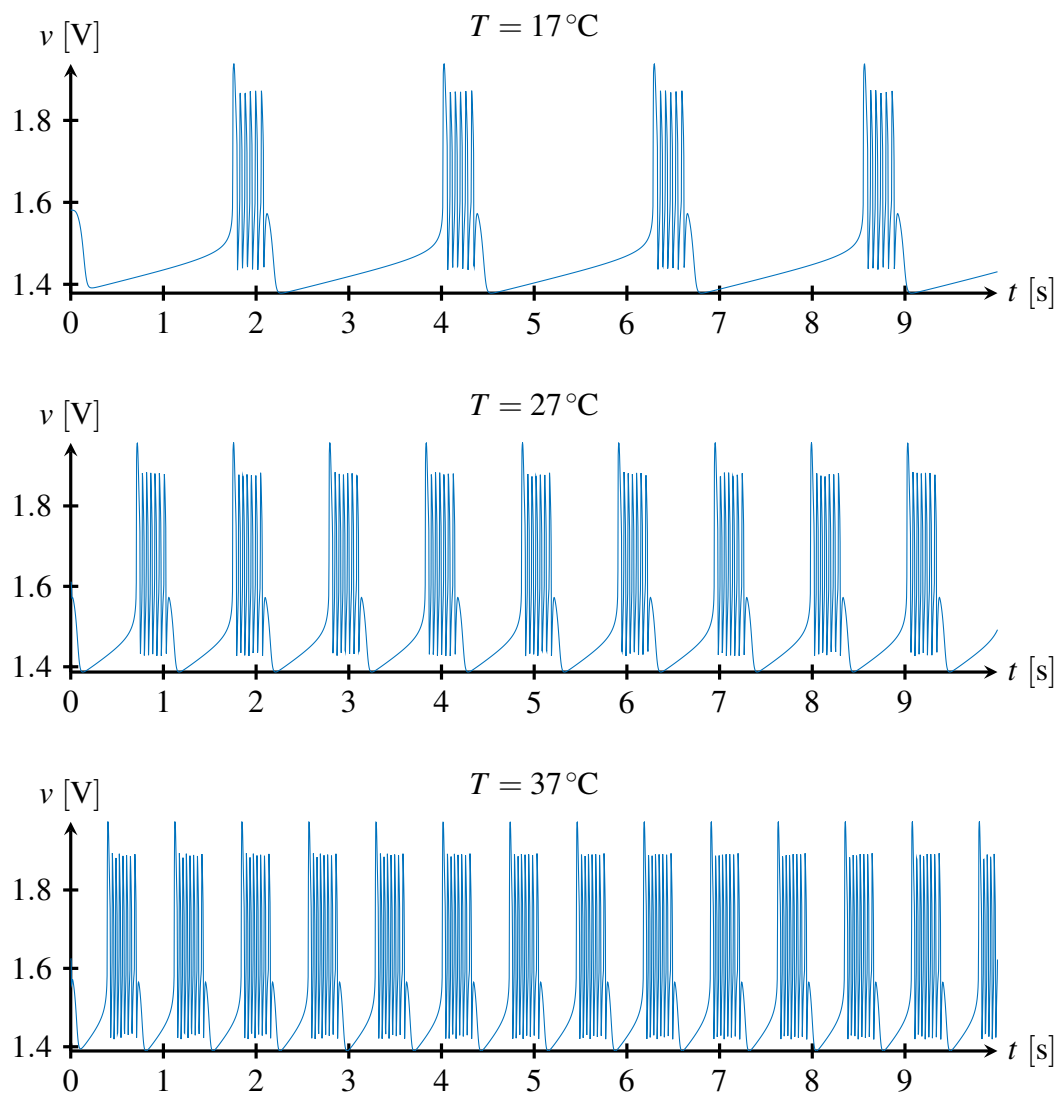


Fig. 5.6: Temperature dependence of the circuit. As temperature is increased, the circuit maintains the bursting oscillation with increasing interburst frequency, mimicking the behaviour of biological neurons.

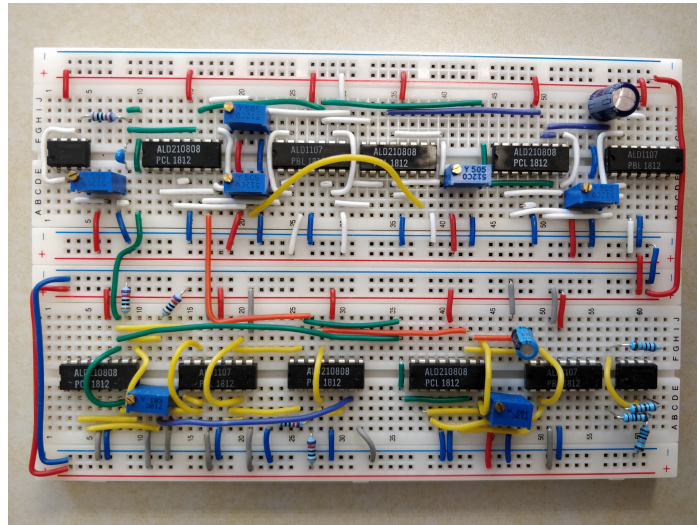


Fig. 5.7: Breadboard with a single neuron circuit.

operated with a supply voltage of 5 V. The breadboard containing the circuit is shown in Fig. 5.7.

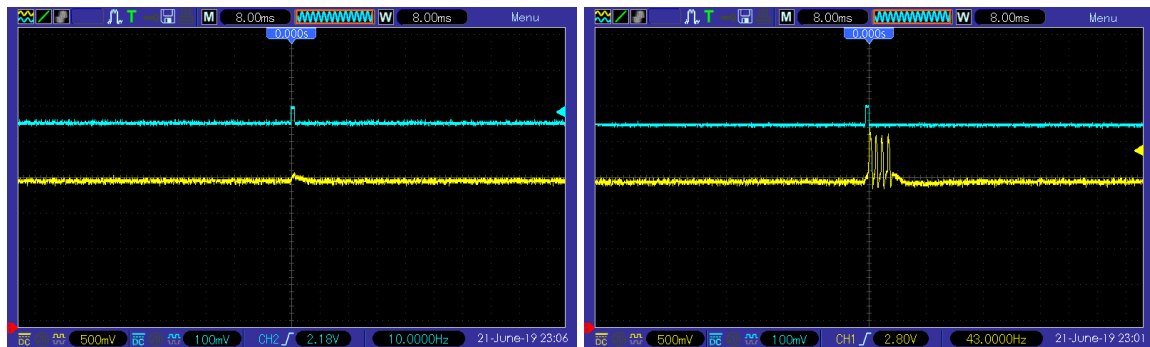


Fig. 5.8: Burst excitability of the circuit. Left: subthreshold response. Right: burst as a response to an above threshold pulse.

Setting the parameters of the circuit to the bursting regime (Fig. 4.10), we first study the modulation through the applied current. For low applied current, the circuit is at rest, but excitable, and this can be seen in Fig. 5.8. As predicted, increasing the current sets the circuit in the bursting regime (Fig. 5.9, left), while increasing it sufficiently high turns off the slow spiking and the circuit is purely fast spiking (Fig. 5.9, right).

Finally, we show that the circuit's operation can be controlled by modulating the gain of the slow negative conductance as in Fig. 4.13. By applying a periodic triangle wave at the $(v_b)_s^-$, we observe that the neuron transitions between eliciting individual spikes to bursting through increasing number of spikes per period (Fig. 5.10).

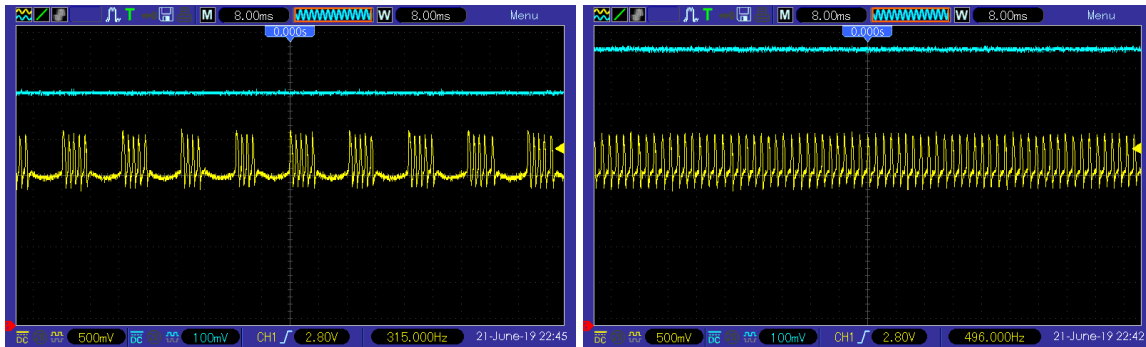


Fig. 5.9: Bursting and spiking traces of the circuit.

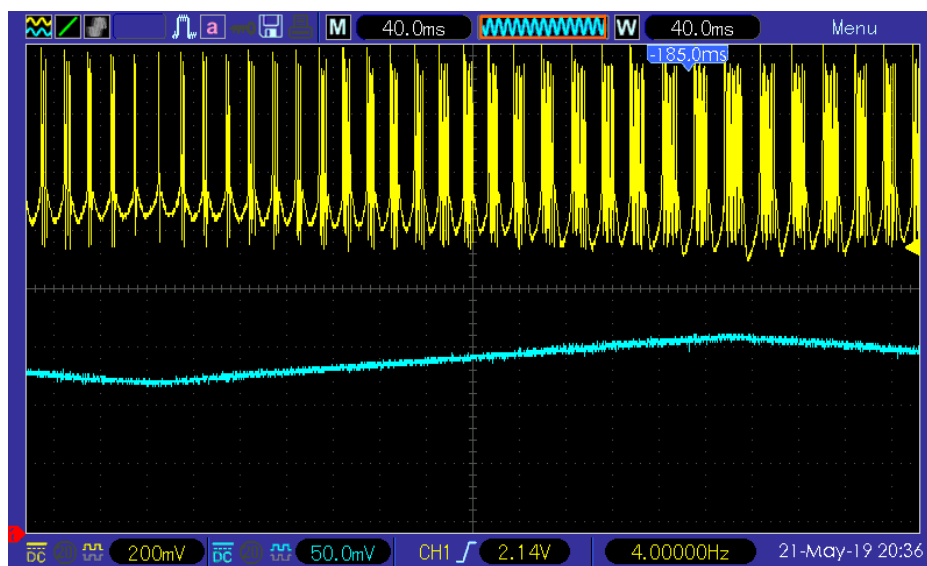


Fig. 5.10: Transition between spiking and bursting in the circuit. A periodic triangle wave is applied at the base voltage of the slow negative conductance $(v_b)_s^-$ (blue trace) so that the circuit is periodically moving between the bursting and slow spiking regimes.

Appendix 5.A Transconductance amplifier linearisation

To find the ratio κ/κ_l , we take a similar approach as in [97, 96] and consider a small voltage increase $\frac{\Delta v_{in}}{2}$ at the input v_1 and an equivalent voltage decrease $-\frac{\Delta v_{in}}{2}$ at the input v_2 of the amplifier in Fig. 5.2. Due to the symmetry, this leads to an equivalent increase in current i_1 and decrease in current i_2 of $\frac{\Delta i_{out}}{2}$. At the same time, the drain voltage of the bias transistor does not change. We thus consider an equivalent small-signal circuit of one branch of the amplifier with the drain of the bias transistor set to the ground (Fig. 5.11).

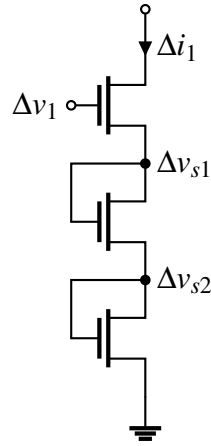


Fig. 5.11: Small-signal analysis of the linearised transconductance amplifier. The circuit is one differential branch of the amplifier, where the common middle node is grounded.

Looking at a single transistor in saturation, we relate the change in the drain-source current to the changes of the voltages at the gate and the source by differentiating Eq. (3.2):

$$\frac{\partial i_{ds}}{\partial v_g} = \kappa \frac{i_{ds}}{v_T} \quad (5.9)$$

$$\frac{\partial i_{ds}}{\partial v_s} = -\frac{i_{ds}}{v_T} \quad (5.10)$$

We now apply these relationships to the circuit in Fig. 5.2:

$$\Delta i_1 = \left(\kappa \frac{i_1}{v_T} \right) \Delta v_1 - \left(\frac{i_1}{v_T} \right) \Delta v_{s1} \quad (5.11)$$

$$\Delta i_1 = \left(\kappa \frac{i_1}{v_T} \right) \Delta v_{s1} - \left(\frac{i_1}{v_T} \right) \Delta v_{s2} \quad (5.12)$$

$$\Delta i_1 = \left(\kappa \frac{i_1}{v_T} \right) \Delta v_{s2} \quad (5.13)$$

Solving these equations, we obtain:

$$\frac{\Delta i_1}{\Delta v_1} = \frac{\kappa^3}{\kappa^2 + \kappa + 1} \left(\frac{i_1}{v_T} \right) \quad (5.14)$$

This relationship means that we can view the three transistors in Fig. 5.11 as a single one with the characteristic:

$$i_{ds} = i_0 e^{\frac{\kappa_l v_1 - v_s}{v_T}} \quad (5.15)$$

where we have defined $\kappa_l = \frac{\kappa^3}{\kappa^2 + \kappa + 1}$. Following the standard derivation for a simple transconductance amplifier [73], we obtain the input-output relationship for the linearised amplifier:

$$i_{out} = i_b \tanh \left(\kappa_l \frac{v_1 - v_2}{2v_T} \right) \quad (5.16)$$

$$\kappa_l = \frac{\kappa^3}{\kappa^2 + \kappa + 1}$$

Chapter 6

Excitability switch: from single neurons to networks

In previous chapters we have introduced the physiological concept of neuromodulation as one of the main biological control methods for orchestrating neural behaviour. We highlighted the importance of retaining the four essential feedback loops present in biological neurons, and we showed how modulation of each individual loop modifies different aspects of neural excitability. In the following chapter, we will concentrate on a specific modulatory mechanism that we have introduced in Chapter 4 and implemented in Chapter 5: the transition between bursting and spiking regimes through the control of the slow negative conductance.

This *excitability switch* has been observed in many different neural systems and underlies a prevalent and possibly highly important mechanism. The transition between the inactive and receptive states during sleep and wakefulness in animals has been found to be determined by the transition from the slow oscillatory to the fast rhythmic states in the thalamus and cerebral cortex, controlled by the neuromodulatory actions on the cell level [108, 72]. The excitability switch in subthalamic nucleus neurons has been found to be connected to the development of Parkinson's disease as it leads to different synchronisation properties of the nervous system [6]. The two modes have remarkably different input-output behaviours, as evidenced for example in the thalamic relay neurons that pass on sensory inputs to the higher processing stages [102]. The different processing properties are utilised in sensory systems, leading to different detection capabilities of the cells, as well as to different responses of the neural network depending on the spatio-temporal scale of the sensory input [58, 71, 83, 12]. Central pattern generating networks that control repetitive actions such as movement are

constantly under neuromodulatory regulation [40]. Recent work [22] suggests that switching between bursting and spiking modes could be a fundamental mechanism behind the ability of rhythmic networks to quickly switch different rhythms. Nodal control of excitability has profound effects on the network behaviour and provides a method for controlling across scales [100], introducing a possibly powerful engineering principle.

Inspired by biological examples, we would like to use the model introduced in Chapter 4 to utilise the neuromodulatory capabilities in artificial sensory and oscillatory networks. We start by investigating how modulation of a single neuron affects its input-output processing capabilities, concentrating on the bursting/spiking switch. We discuss how this internal switch can be turned into an external control mechanism through the applied current, a mechanism observed in biological neurons [6]. We showcase later how such an external switch can be utilised in a simple network setting where the increased activity of a subpopulation can switch the spiking mode of another subpopulation, and thus change its processing properties.

The second part of the chapter moves towards building small networks that are able to utilise the single neuron control to adjust the network behaviour. We will showcase this through a few toy examples that aim to present the multi-scale nature of the approach. We start by discussing a simplistic model of a synaptic connection that is nevertheless able to capture the principal effects of interneuron connections. We use these building blocks to first construct the most basic rhythm generating network: a two-cell half-centre oscillator (HCO). We show how the single cell switch can control the network rhythm and make individual neurons susceptible to local inputs. We then generalise the same mechanism by instead utilising the HCO as the building block in creating a small central pattern generating network (CPG) inspired by the lobster gastric rhythm [69, 39, 38, 22]. Our aim in this chapter is to show that controlling cellular properties can have important effects on the network behaviour, and to motivate future design that uses the neuromodulation mechanisms captured by the circuit structure from Chapters 4 and 5.

6.1 Single cell control

6.1.1 Modulating single neuron I/O properties

The combination of the fast and slow excitability currents endows the neuron with possible four states, as each of the slow and fast oscillatory modes can be turned off or on independently. We concentrate here on the control of the slow excitability while the neuron

stays fast excitable (Fig. 6.1). When the slow negative conductance is on, the combination of the slow and fast excitability leads to bursting. In this regime, the fast input spikes are effectively rejected as disturbance, as the localised inputs are blocked by the slow mode of the oscillation. On the other hand, when the slow negative conductance is off, individual spikes are unattenuated at the output and the circuit behaves as a relay.

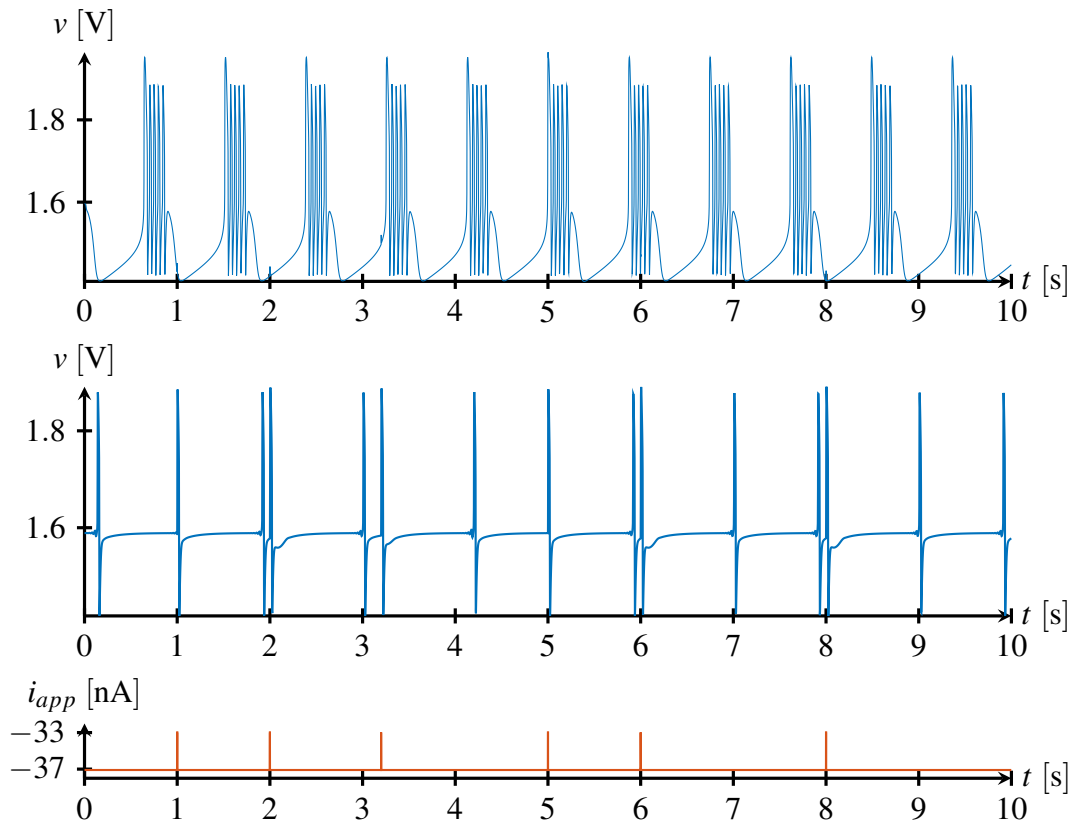


Fig. 6.1: Neural circuit's input-output properties in the oscillating regime. When the circuit is in the bursting mode, the fast input spikes are rejected as disturbance and the oscillating bursting behaviour is uninterrupted. When the circuit is in the slow spiking mode, each individual spike is relayed at the output.

This simple switch has important consequences for the single cell in the network setting. When the neuron is in the slow bursting mode, it synchronises with the slow rhythm and blocks local inputs thus participating in the global network rhythm. On the other hand when the slow mode is off, the neuron can switch off from the global rhythm and participate in the local transfer of information.

This mechanism relies crucially on the modulation of the slow negative conductance from a high to a low value. Shaping the slow bistability range allows the generation of arbitrarily large interspike interval (Fig. 4.14), so that the circuit enters the slow spiking regime when

bursting is terminated, as in Fig. 6.1. This is in contrast to the transition from bursting to spiking for an increasing applied current shown in Fig. 4.10, where the onset of spiking is characterised by a fast oscillation. Unlike the slowly spiking relay mode, the fast spiking blocks incoming inputs similarly to the bursting mode, but unlike bursting, is not susceptible to the synchronisation with slow network oscillations.

This mechanism can thus be viewed as a result of an internal property of the node. In order to allow for an external control of the neural switch, there needs to be an additional feedback loop that would regulate the internal slow current in response to the applied current. We show how this mechanism can be introduced in the following section.

6.1.2 External I/O modulation

In the previous section, the modulation between the bursting and spiking modes was achieved by adjusting the gain of the slow negative conductance element that controls the bistability range in the slow I-V curve (Fig. 4.13). In neurons such as the ones found in the subthalamic nucleus [6], this modulation has an automatic regulatory pathway through the inactivation of the slow calcium current, the current that provides slow negative conductance. This inactivation acts so that when the applied current is high, the slow negative conductance is off, therefore leading to a purely spiking activity of the neuron. On the other hand, lowering the applied current activates the slow inward calcium current, and the cell's activity transitions into bursting due to the activation of the source of slow negative conductance. This mechanism of *hyperpolarisation-induced bursting* has been studied extensively [6, 18, 116], and could provide an important external control mechanism for fast localisation of network behaviour [20].

We can make the internal switch of excitability, achieved through the control of the slow negative conductance gain, into an external switch through the applied current, by applying the very same mechanism that the biology utilises. Hyperpolarisation-induced bursting requires feedback from the input current to the slow negative conductance gain in order to induce the switch. We introduce this feedback in a simple manner by adding a multiplicative inactivation variable to the slow negative conductance gain, so that it becomes:

$$\alpha_s^- = \bar{\alpha}_s^- h(V_{us}) \quad (6.1)$$

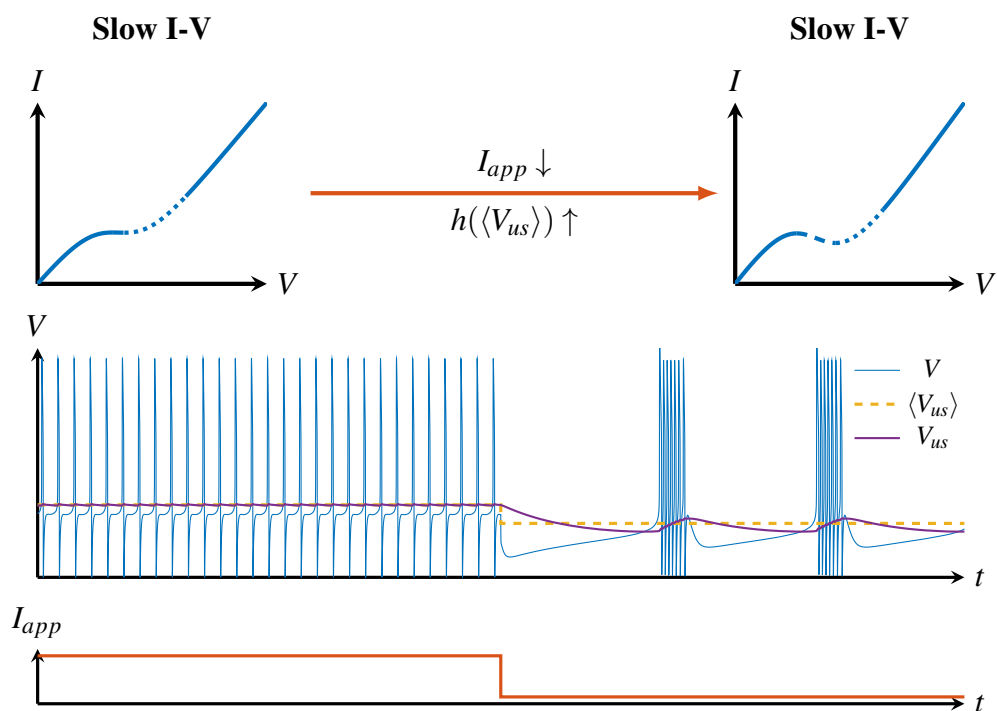


Fig. 6.2: Hyperpolarisation-induced bursting. An additional feedback loop through the inactivation of the slow negative conductance $h(V_{us})$ ensures that the decrease in applied current increases the slow negative conductance and induces a switch from slow spiking to bursting. This feedback is achieved through the ultra-slow voltage V_{us} which decreases as the neuron goes from the spiking to bursting states. The slow I-V curves are plotted for the average value of the ultra-slow voltage $\langle V_{us} \rangle$ in the two regimes.

where $\bar{\alpha}_s^-$ is the maximal gain of the slow negative conductance, and h is the inactivation variable with the following form:

$$h(V_{us}) = S(\beta(-V_{us} - \delta_h)) \quad (6.2)$$

where β is the additional steepness factor, δ_h is the voltage offset of the inactivation, and $S(x)$ is the sigmoid function:

$$S(x) = \frac{1}{1 + \exp(-x)} \quad (6.3)$$

We fix the value of $\beta = 2$ due to the hardware implementation specifics (see Section 6.2.1), but once fixed, the choice of β does not play a major role. Introducing the feedback is described in the following heuristic way: in the open-loop, the neuron is switched from spiking to bursting by increasing the slow negative conductance gain from a low value α_{s1}^- to a high value α_{s2}^- , while decreasing the current from I_{app1} to I_{app2} . Feedback is then required to automatically modulate the slow negative conductance gain between these two values when the current is switched from I_{app1} to I_{app2} . This is ensured by finding the average ultra-slow voltage in the two modes $\langle V_{us} \rangle_1$ and $\langle V_{us} \rangle_2$, and choosing the parameters $\bar{\alpha}_s^-$ and δ_h so that:

$$\bar{\alpha}_s^- h(\langle V_{us} \rangle_1) = \alpha_{s1}^-, \quad \text{for } I_{app} = I_{app1} \quad (6.4)$$

$$\bar{\alpha}_s^- h(\langle V_{us} \rangle_2) = \alpha_{s2}^-, \quad \text{for } I_{app} = I_{app2} \quad (6.5)$$

Closing the loop by introducing the inactivation then achieves the excitability switch mechanism through the applied current.

6.2 Neural interconnections

The interconnections between neurons fall into two categories: electrical and chemical. The electrical connections constitute of gap junctions and are modelled simply in the circuit language as resistive connections between neurons, so that the currents flowing into neuron j (I_{ij}^p) and neuron i (I_{ji}^p) due to a passive connection between them are:

$$I_{ij}^p = -I_{ji}^p = g_{ij}^p (V_i - V_j) \quad (6.6)$$

where g_{ij}^p is the conductance of the passive connection.

Chemical synapses on the other hand mirror the way in which ionic currents behave, with the difference that now the activity of the *presynaptic* neuron modulates the synaptic current in the *postsynaptic* neuron. Much like the ionic conductances, they have a well-defined timescale in which they act, and they only activate in the specific voltage range of the presynaptic neuron, so that the current flows only while the presynaptic neuron is *active*. Unlike the resistive connections which are dissipative and tend to synchronise and average out the activity across neurons, synaptic connections can lead to diverse heterogeneous behaviours.

We use the same modelling approach to design synaptic current elements as for realising localised conductance elements described in the Section 4.1, so that the synaptic current I_{ij}^{syn} in neuron j depends on the activity of neuron i in the following way:

$$I_{ij}^{syn} = \alpha_{ij}^{syn} S(\beta(V_i^x - \delta^{syn})) \quad (6.7a)$$

$$\tau_x \dot{V}_i^x = V_i - V_i^x \quad (6.7b)$$

α_{ij}^{syn} is the synaptic weight, β is the steepness factor, δ^{syn} is the voltage offset of the synaptic current. This synaptic implementation is similar to the form used in the well-known Hopfield network model [44], with the addition of the temporal dependence.

The circuit implementation is further discussed in Section 6.2.1.

The voltage offset of the synaptic connections δ_{syn} is chosen so that the synaptic current is close to 0 while the presynaptic neuron is silent, while generating a current spike in response to an action potential in the presynaptic neuron. The offset is therefore determined by the voltage range of the action potential: by fixing α_f^- and δ_f^- of each individual neuron, the spike amplitudes are also fixed, and δ^{syn} can be constant throughout the network. The steepness factor β is set by the circuit implementation and is equal for all synapses.

We use the model described in (6.7) to model **both** excitatory and inhibitory synapses, the only difference between the two being the sign of the synaptic weight α_{ij} . In the case of an excitatory synapse, the spike in the presynaptic neuron induces an inward current I_{ij}^{exc} in the postsynaptic neuron so that:

$$\alpha_{ij} > 0 \quad (6.8)$$

and in the case of an inhibitory synapse, the spike in the presynaptic neuron induces an outward current I_{ij}^{inh} in the postsynaptic neuron, so that:

$$\alpha_{ij} < 0 \quad (6.9)$$

For the inhibitory synapses in this chapter we set the dynamics to be *slow*, so that $V_i^x = V_i^s$ in Eq. (6.7).

6.2.1 Synapse Circuit

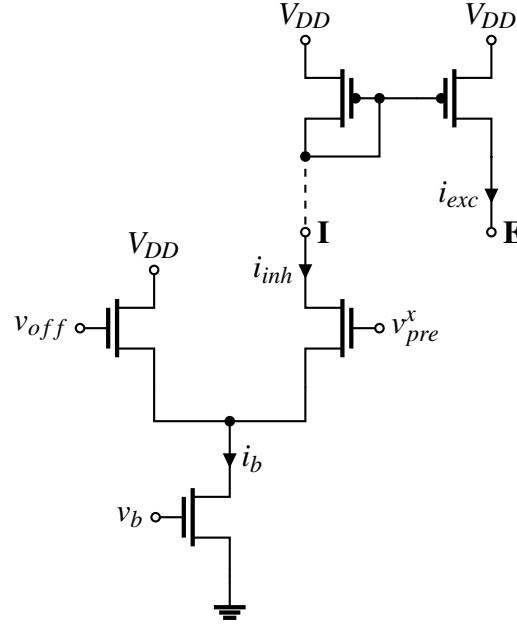


Fig. 6.3: Synapse circuit. The basic differential amplifier circuit realises a current i_{inh} which has a sigmoid function dependence on the presynaptic input voltage v_{pre} . For an inhibitory synaptic connection, the postsynaptic voltage is connected to the node **I** and the current acts as a sink. For an excitatory connection, the additional current mirror is necessary so that the current acts as a source, and the postsynaptic voltage is connected to the node **E**.

The realisation of a synapse element of Eq. (6.7) is achieved with the same basic circuitry used for the realisation of a localised conductance element (Fig. 6.3). We take a single current of the differential amplifier that then realises an inward inhibitory current:

$$i_{inh} = i_b S \left(\kappa \frac{v_{pre}^x - v_{off}}{v_T} \right) \quad (6.10)$$

Compared to the transconductance amplifier input-output equation (Eq. (3.5)), there is an additional steepness factor of 2. This corresponds to setting $\beta = 2$ in the dimensionless synapse equation Eq. (6.7).

In order to realise an outward excitatory current, it is necessary to have an additional current mirror that will copy the current i_{inh} and invert its direction. The synaptic strength is

then modulated through the sole parameter v_b which controls the current i_b in the circuit. The v_{off} parameter is chosen so that there is negligible output current while the neuron is silent, and a pulse-like output is generated in response to each action potential of the presynaptic neuron. The voltage v_{pre}^x can be set to a different filtered version of the presynaptic membrane voltage depending on the desired timescale of the synapse - in the following examples we set the timescale of the synapse to slow by having $v_{pre}^x = v_{pre}^s$.

6.3 Half-centre oscillator

We start with the simplest rhythm generating network: the half-centre oscillator. The half-centre oscillator circuit is the building block of more complex pattern generating networks and constitutes of a reciprocal inhibitory connection between two neurons or neural populations [10]. We restrict ourselves to the former situation where the single neuron behaviour can also be interpreted as the average activity of a population, in which case the same neuromodulation principles that would apply to controlling the single-neuron behaviour can be generalised to the control of a population.

The oscillatory behaviour of the HCO is determined by the individual properties of the neurons as well as the properties of the reciprocal connections. The individual neurons can be independently excitable but non-oscillating, in which case the network oscillation emerges from the synaptic currents driving the neurons sequentially into firing [113]. We will concentrate on another possibility, where the network oscillation is due to the individual oscillatory properties of the neurons and the network connections are kept weak. The synaptic connections are kept weak by restricting them to be at least an order of magnitude smaller than the intrinsic neural currents that we have described in Chapter 4. In this case the synaptic connections are mainly defining the phase relationships between the oscillators, but do not have a significant effect on the properties of the oscillation such as frequency and duty cycle.

We consider a situation where neurons are oscillating at different frequencies, shown in Fig. 6.4. In order for neurons to be susceptible to synchronisation with weak coupling, the difference in oscillating frequencies needs to be kept relatively small. This is shown in Fig. 6.5: by introducing the reciprocal inhibitory connection, neurons synchronise in anti-phase.

The network rhythm shown in Fig. 6.5 can be controlled and effectively switched off by modulating the properties of the individual cells. By controlling the slow negative

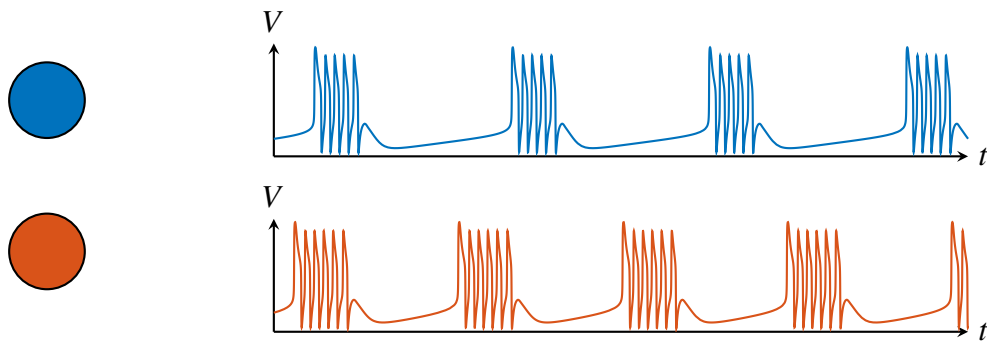


Fig. 6.4: Half-centre oscillator disconnected. Individual neurons are bursting with similar frequencies.

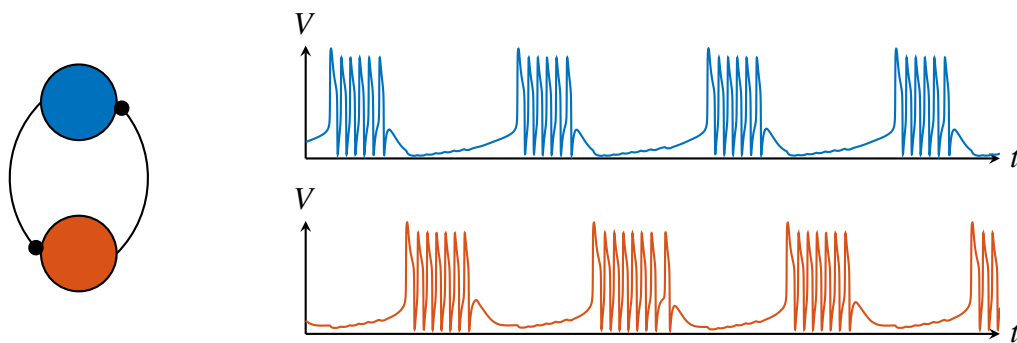


Fig. 6.5: Half-centre oscillator connected. The two bursting neurons are connected through mutual inhibitory connections. As the connections are kept weak, they mainly serve to determine the phase relationship, leading to the anti-phase oscillation of the network.

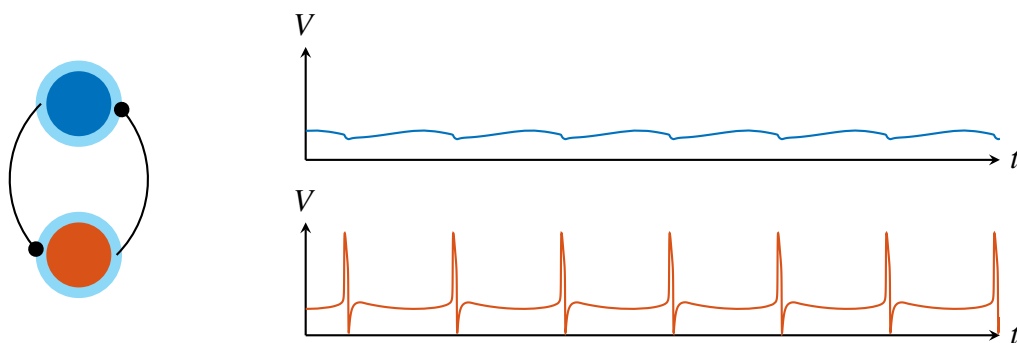


Fig. 6.6: Excitability switch in the half-centre oscillator. Decreasing the slow negative conductance gain at the cell level turns off the slow oscillation, and neurons are able to process local inputs as discussed in Fig. 6.1. The light blue border around nodes represents the tonic spiking state of the neuron.

conductance gain as described in previous chapter, the neurons switch into the tonic spiking mode, and the network oscillation is lost Fig. 6.6. In this regime, the neurons are susceptible to local inputs as shown previously (Fig. 6.1). The main control is thus kept at the nodal level, while the neural interconnections determine the anti-phase property of the network oscillation.

6.3.1 Excitability switch through inhibition

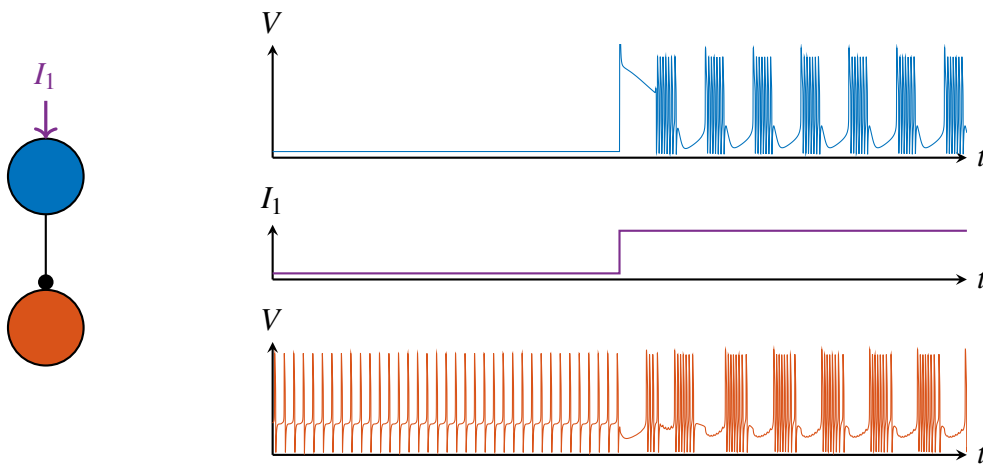


Fig. 6.7: Inhibitory switch of neuron excitability. Control neuron (blue) modulates the excitability of the second neuron (red) through inhibition when the second neuron has slow conductance inactivation dynamics discussed in Fig. 6.2.

In this section we would like to briefly revisit the external control of a neuron's excitability through the hyperpolarisation-induced bursting mechanism that we described in Section 6.1.2. The inactivation of the slow negative conductance allows the external applied current to the neuron to control its excitability. In a network setting, this leads to the possibility of neurons modulating the input-output properties of other neurons they are connected to through excitatory or inhibitory connections. We illustrate this in a simple toy example where a control neuron is modulating the excitability of the second neuron through a single inhibitory connection. By changing the firing mode of the control neuron, the magnitude of the inhibitory current changes in turn, and thus the oscillatory properties of the second neuron. When the control neuron is silent, there is no inhibitory current, and the second neuron is in the tonic spiking mode. When the control neuron is turned on, it starts to burst and consequentially generates an oscillatory inhibitory current to the second neuron, which induces the switch in its excitability regime to the slow bursting mode. The network then

oscillates in the anti-phase bursting regime. Such mechanisms have been shown to have important consequences for localising network oscillations in excitatory-inhibitory networks [20].

6.4 Central pattern generator

The property shown in Section 6.3 where the network rhythm is controlled through the individual nodes in the presence of weak interconnections can be generalised to different network topologies of varying size [100]. In this section, we concentrate on a network inspired by the simplified STG model [69, 39, 38]. By isolating the rhythm generating part of the network and grouping the neurons with synchronised activity, the authors identified the essential five-neuron network that represents the interaction between the pyloric and gastric rhythms in the STG. The network presents an interesting topology as it effectively consists of two half-centre oscillators communicating through a single neuron. The pyloric rhythm sub-network is responsible for the generation of the fast rhythm, while the gastric sub-network oscillates in the slow regime, and the rhythms are allowed to interact. As such, this simple topology provides a rich venue for studying coexisting distinct rhythms in a single network.

We recreate this network in Fig. 6.8. The parameters of the neurons are chosen so that the left half-centre oscillator generates faster bursting oscillations than the right, slow half-centre oscillator. As we effectively fix the time-constants of the individual neurons, this is done by manipulating the ultra-slow feedback that controls the interburst frequency. The middle hub neuron is set to the tonic spiking mode, so that it effectively acts as a relay between the two independent rhythms.

Figure 6.9 shows the two rhythms interacting by adding the resistive connections between the hub neuron and the half-centre oscillators. When the electrical connections are weak, the individual rhythms are mostly unaffected by the connection, and the fast and the slow rhythm within the network coexist. The hub neuron at the same time oscillates with a mix of the two frequencies.

By using the mechanism shown previously in Fig. 6.6, we can effectively disconnect the individual rhythms within the network by modulating the half-centre oscillators between the bursting and slow spiking modes. This is shown in Fig. 6.6 where the slow negative conductance gain is decreased for the neurons within the slow half-centre oscillator. The

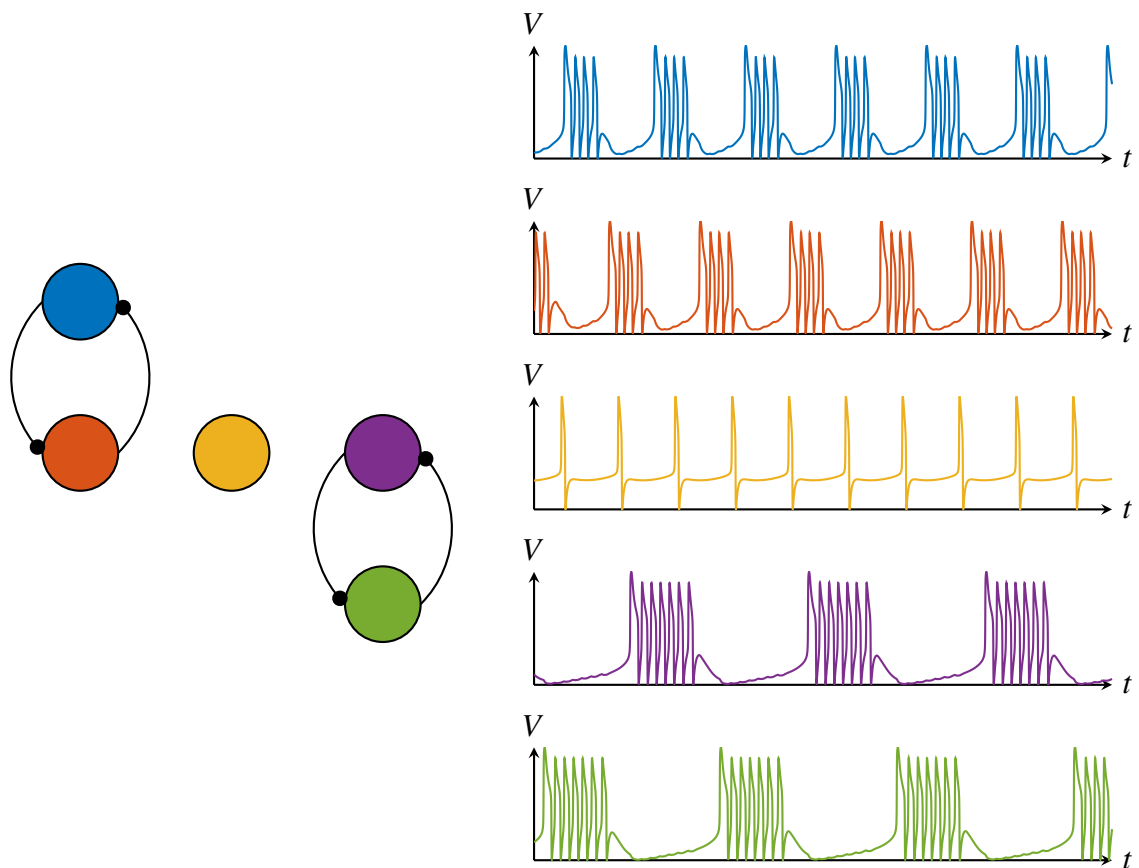


Fig. 6.8: CPG disconnected. The network consists of two half-centre oscillators and a middle hub neuron. The parameters are chosen so that the left HCO is fast and the right HCO is slow, while the hub neuron is in the tonic spiking mode.

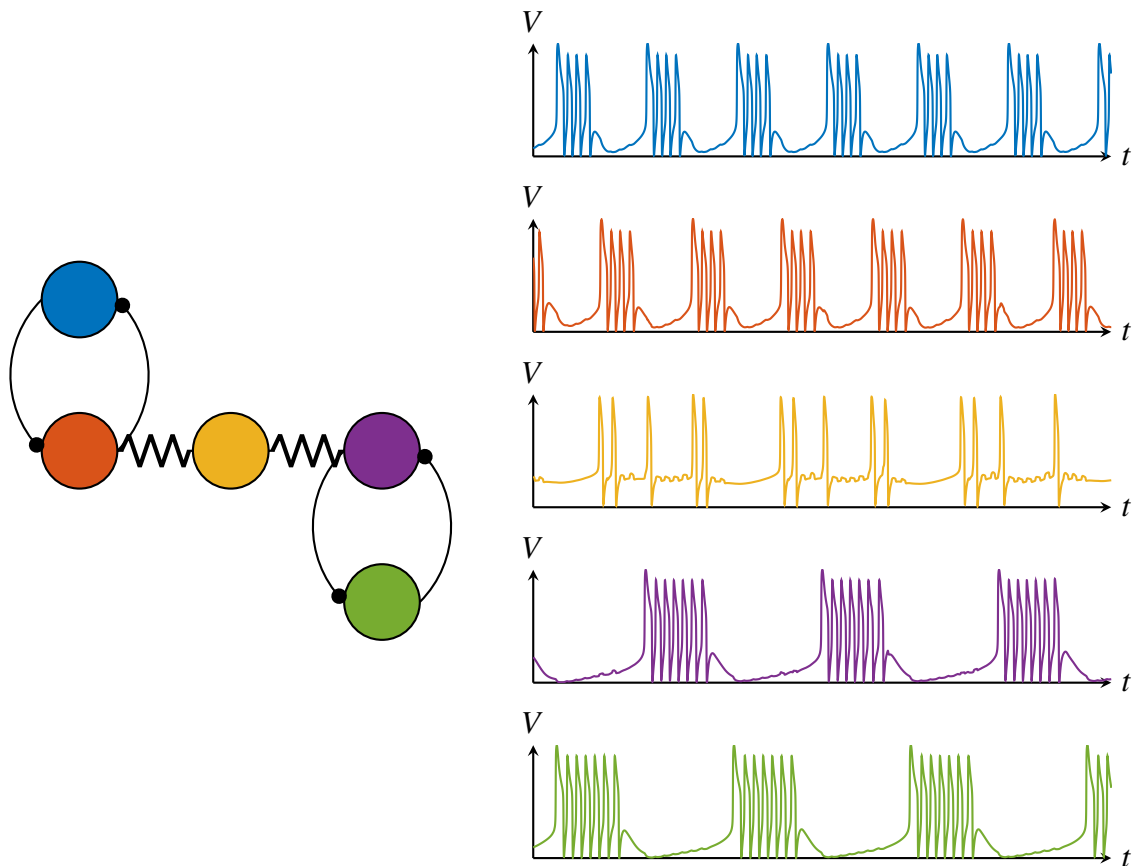


Fig. 6.9: CPG connected. Hub neuron is connected to individual neurons of the half-centre oscillators through electrical connections. The electrical connections enable the interaction between the two rhythms. Due to the presence of slow negative conductance in the rhythm generating neurons, the bursting rhythms are robust, so that the fast and slow rhythms coexist, while the hub neuron experiences a mix of the two oscillations.

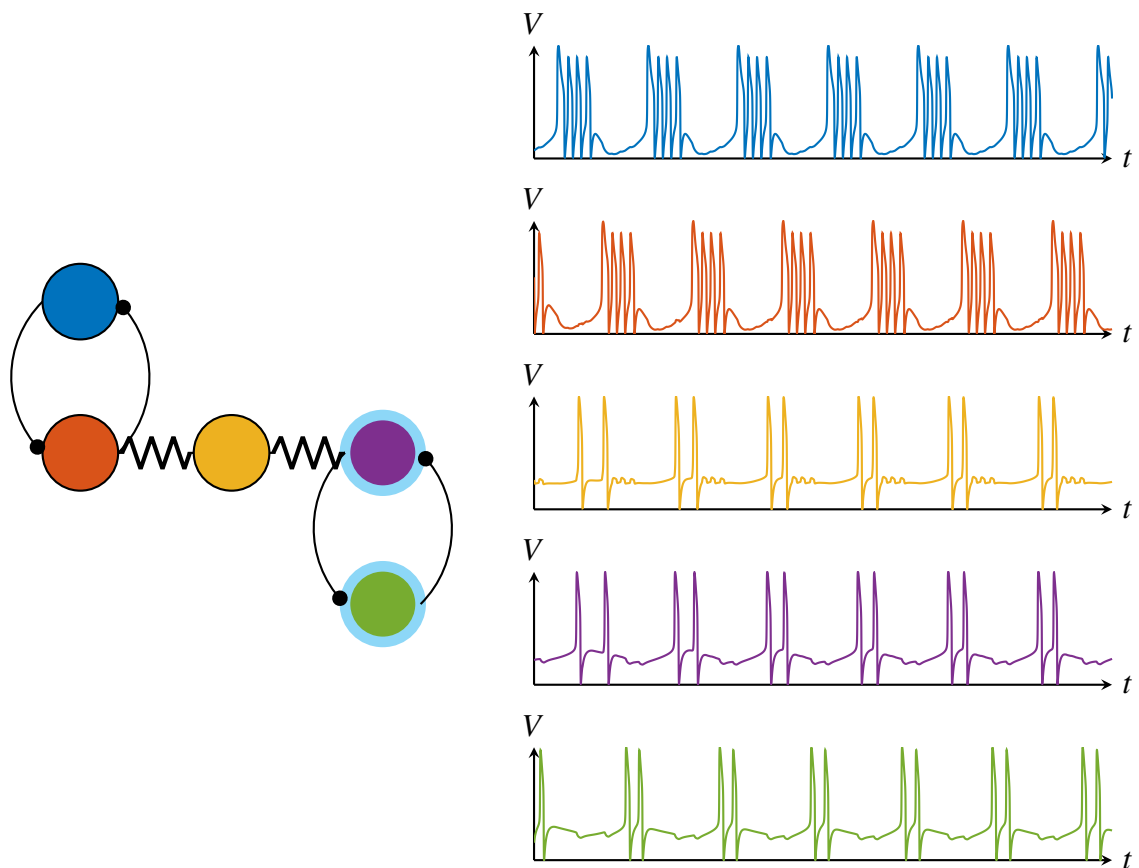


Fig. 6.10: Disconnecting a rhythm from the CPG. By modulating the slow half-centre oscillator through the inactivation of the slow negative conductance, the slow HCO cells are switched to the tonic relay mode. The fast bursting rhythm effectively propagates through the hub neuron, and the network is globally oscillating with the fast rhythm.

slow half-centre oscillator neurons then act as followers, and the fast rhythm propagating through the hub neuron now has sufficient strength to synchronise these neurons. In this case the whole network oscillates with the fast rhythm.

Appendix 6.A Simulation parameters

All simulations in this chapter apart from Fig. 6.1 were carried out in Python using the model described in Eqs. (4.9), (4.12) and (4.13). The parameters for the conductance elements and the applied currents are given in Table 6.1. Common parameters for these figures are the following:

$$\begin{aligned}\tau_f &= 0 \\ \tau_s &= 50 \\ \tau_{us} &= 2500 \\ \delta_f^- &= \delta_s^+ = 0\end{aligned}$$

Table 6.1: Parameter values for simulations in Chapter 6

Figure	α_f^-	α_s^+	α_s^-	δ_s^-	α_{us}^+	δ_{us}^+	I_{app}
6.1 (top)	2	2	1.5	-0.88	2	0	-1.8
6.1 (bottom)	2	2	1	-0.88	2	0	-1.8
6.2*	2	2	1.6	-0.88	2	0	-2.2, -2.5
6.4, 6.5 (blue)	2	2	1.5	-0.88	1.5	-0.88	-1.3
6.4, 6.5 (red)	2	2	1.5	-0.88	1.5	-0.88	-1
6.6 (blue)	2	2	1.04	-0.88	1.5	-0.88	-1.3
6.6 (red)	2	2	1.04	-0.88	1.5	-0.88	-1
6.7 (blue)	2	2	1.5	-0.88	1.5	-0.88	-2.2, -0.8
6.7 (red)*	2	2	1.7	-0.88	1.5	-0.88	-0.65
6.8, 6.9, 6.10 (fast)	2	2	1.5	-0.88	4	-0.88	-1
6.8, 6.9, 6.10 (hub)	2	2	1	-0.88	2	-0.88	-1
6.8, 6.9 (slow)	2	2	1.5	-0.88	1.5	-0.88	-1
6.10 (slow)	2	2	1	-0.88	1.5	-0.88	-1

*These neurons additionally have the inactivation dynamics of Eq. (6.1) with $\delta_h = -0.5$ and $\beta = 2$.

All inhibitory connections have the parameters:

$$\begin{aligned}\alpha_{inh} &= 0.2 \\ \delta_{inh} &= -1 \\ \beta &= 2\end{aligned}$$

and resistive connections:

$$g_{el} = 0.02$$

Figure 6.1 was obtained in SPICE using the BSIM3 model with the TSMC 0.35 μm parameters. The circuit parameters used were matched to the dimensionless parameters listed in Table 6.1.

Chapter 7

Conclusion

Neuromodulation is an essential biological mechanism that targets individual neurons and continuously alters their input-output properties, in turn shaping their response depending on the changing conditions and network requirements. It is a key process underlying adaptation in neurons, thus enabling the adaptive sensory and motor control in animals. Understanding, and at the same time, synthesising these neuromodulatory mechanisms is the fundamental requirement for building controllable and robust models of neuronal behaviour.

This thesis introduced a novel model and methodology for designing and analysing neurons with neuromodulatory capabilities. We discussed how such a model can be synthesised using well-known neuromorphic circuit techniques, and presented a proof-of-concept realisation. In addition, we have presented initial network results using the model that aim to showcase the importance of cellular control in interconnected systems, as well as to inspire future research utilising the proposed principles and circuit architecture.

We will now give an overview of the main contributions of the thesis, as well as the potential paths for future research.

7.1 Summary

Feedback structure of excitability In Chapter 2 we have given an overview of the fundamental concept of neural excitability, and discussed how it generalises to the multi-scale nature of neural bursting behaviour. We have examined and outlined the essential feedback structure of excitability consisting of the interplay between the fast positive

feedback and the slow negative feedback, represented in circuits by elements that provide fast negative and slow positive conductance, respectively. This organisation can then be repeated in slower timescales by adding *slow excitability* currents. The interaction between these fast and slow excitability currents enables the robust generation of neural behaviour. This structure is often overlooked in simplified models of neurons, thus frequently making the observed behaviour fragile and without the ability to smoothly adapt. Consequently, we have discussed in Chapter 3 how simplified neuromorphic circuits can experience the same issues, while biologically accurate circuits suffer from the difficulty of tuning due to their complex parametrisation. We use the four feedback loop structure for our proposed simplified neural model, and stress its importance in any simplified or detailed model that would robustly capture the control properties of neurons.

Simplified model of neuromodulation We have introduced in Chapter 4 a simplified circuit architecture implementing the dynamics of the neural membrane. It follows the structure of conductance-based models by having the parallel interconnection of feedback currents, but aims to simplify the dynamics by purely capturing the four fundamental feedback loops through reduced current models. Each current is modelled as an interconnection of a first-order filter and a nonlinear I-V element which can be easily synthesised in hardware. The main contribution of the approach is the novel method for designing and controlling the circuit behaviour through the shaping of its input-output I-V curves in distinct timescales. As an input-output approach, it allows direct measurement in a circuit and is independent of the underlying implementation specifics.

Neuromorphic implementation Based on the methodology in Chapter 4, we have shown in Chapter 5 how basic neuromorphic circuits can be utilised to construct a neuron with neuromodulatory properties. Following the structure of Chapter 4, the circuit synthesis is simple, and only requires the parallel interconnection of subthreshold transconductance amplifiers realising the basic I-V elements and first-order filters. We have characterised its operation through a SPICE simulation, and shown how the robustness of the design reduces to the robustness of its input-output properties. The proof-of-concept circuit that we have presented in addition showcases that the circuit can be easily synthesised using off-the-shelf components. The study undertaken in this chapter provides a blueprint for future scaling-up of the design to build network behaviour.

Network design Finally, we have outlined the small-network design using the model in Chapter 6. We have highlighted neuromodulation between bursting and spiking modes as an important biological mechanism that has not received a lot of attention in circuit design so far. We have shown how the transition leads to different input-output properties of neurons, and have discussed how the circuit can be augmented to showcase the transition through an external current modulation, a mechanism observed in several biological networks. We have highlighted the effect of bursting-spiking transition in a few toy examples that serve as building blocks for generating central-pattern generator networks. This chapter provides a first step into synthesising neural networks that would utilise cellular control properties in order to adapt their behaviour.

7.2 Future work

Integrated circuit implementation The design and the simulation results in Chapter 5 naturally lead to the development of the neural circuit in an integrated circuit. Such a development would allow the study of small neuromodulable networks that can be used to design controllable central-pattern generators, as well as neural networks inspired by the sensory systems found in animals. The input-output nature of the control means that additional circuitry can be implemented that would allow for direct measurement of the I-V curves and thus graphical control of neural behaviour in hardware, similar to some previous approaches concentrating on the neural nullcline analysis [4].

Homeostatic regulation Since the structure of the neuromorphic neuron shares the parallel interconnection architecture of conductance-based models, powerful biological concepts such as homeostatic regulation can be implemented in the architecture by mirroring the mechanisms observed in biology [81, 82, 64, 2]. Homeostasis allows neurons to robustly retain their properties in the face of noise, variation in their fundamental elements, and temperature variation - the same problems affecting neuromorphic circuits. These mechanisms act by modulating the feedback loops through the many parallel ionic currents, and the same could be achieved in the circuit architecture by introducing regulatory feedback from the membrane voltage to the gain variables of the localised conductance elements.

Central pattern generator design Designing robust, adaptable and energy efficient central pattern generating systems is an exciting avenue for building robots with biological

capabilities such as adaptable motor control. CPG design and implementation has therefore received a lot of interest in the neuromorphic community [107, 60, 104, 80, 112, 105, 61]. Complementing these approaches, we would like to study how the cellular control properties introduced in this thesis can be used to shape and switch the network oscillation. As a first step, in Chapter 6 we have outlined some of the basic building blocks for generating oscillatory behaviour in networks, and our aim is to utilise these to study network designs inspired by well-studied biological examples such as the STG rhythm generating network in crabs, where cellular properties and neuromodulation have profound effects on the rhythmic pattern.

Sensory devices Another interesting direction is to study how the continuous modulation of the input-output properties of neurons introduced in this thesis can be used to build intelligent sensory systems that utilise these mechanisms to constantly adapt their sensory information processing capabilities. The biological examples such as the electrolocation sensory system of the electric fish [58] show that bursting and spiking are effectively used as different modes of detection when the animal is traversing the environment. Such examples provide an exciting research direction into understanding how these mechanisms could be used to develop novel devices that employ the multi-scale nature of neuronal behaviours.

References

- [1] Aamir, S. A., Müller, P., Kiene, G., Kriener, L., Stradmann, Y., Grübl, A., Schemmel, J., and Meier, K. (2018). A Mixed-Signal Structured AdEx Neuron for Accelerated Neuromorphic Cores. *IEEE Transactions on Biomedical Circuits and Systems*, 12(5):1027–1037.
- [2] Abbott, L. F. and LeMasson, G. (1993). Analysis of Neuron Models with Dynamically Regulated Conductances. *Neural Computation*, 5(6):823–842.
- [3] Arthur, J. V. and Boahen, K. A. (2011). Silicon-Neuron Design: A Dynamical Systems Approach. *IEEE Transactions on Circuits and Systems I: Regular Papers*, 58(5):1034–1043.
- [4] Basu, A. and Hasler, P. E. (2010). Nullcline-Based Design of a Silicon Neuron. *IEEE Transactions on Circuits and Systems I: Regular Papers*, 57(11):2938–2947.
- [5] Benjamin, B. V., Gao, P., McQuinn, E., Choudhary, S., Chandrasekaran, A. R., Bussat, J.-M., Alvarez-Icaza, R., Arthur, J. V., Merolla, P. A., and Boahen, K. (2014). Neurogrid: A mixed-analog-digital multichip system for large-scale neural simulations. *Proceedings of the IEEE*, 102(5):699–716.
- [6] Beurrier, C., Congar, P., Bioulac, B., and Hammond, C. (1999). Subthalamic nucleus neurons switch from single-spike activity to burst-firing mode. *The Journal of neuroscience*, 19(2):599–609.
- [7] Boahen, K. (2005). Neuromorphic Microchips. *Scientific American*, 292(5):56–63.
- [8] Boahen, K. A. (2000). Point-to-point connectivity between neuromorphic chips using address events. *IEEE Transactions on Circuits and Systems II: Analog and Digital Signal Processing*, 47(5):416–434.
- [9] Brette, R. and Gerstner, W. (2005). Adaptive Exponential Integrate-and-Fire Model as an Effective Description of Neuronal Activity. *Journal of Neurophysiology*, 94(5):3637–3642.
- [10] Bucher, D., Haspel, G., Golowasch, J., and Nadim, F. (2015). Central Pattern Generators. In *eLS*, pages 1–12. American Cancer Society.
- [11] Castañós, F. and Franci, A. (2017). Implementing robust neuromodulation in neuromorphic circuits. *Neurocomputing*, 233:3–13.

- [12] Chacron, M. J. (2006). Nonlinear Information Processing in a Model Sensory System. *Journal of neurophysiology*, 95(5):2933–2946.
- [13] Chay, T. R. and Keizer, J. (1983). Minimal model for membrane oscillations in the pancreatic beta-cell. *Biophysical Journal*, 42(2):181–189.
- [14] Connors, B. W. and Gutnick, M. J. (1990). Intrinsic firing patterns of diverse neocortical neurons. *Trends in Neurosciences*, 13(3):99–104.
- [15] Dayan, P. and Abbott, L. F. (2001). *Theoretical Neuroscience: Computational and Mathematical Modeling of Neural Systems*. MIT press.
- [16] Dethier, J., Drion, G., Franci, A., and Sepulchre, R. (2015). A positive feedback at the cellular level promotes robustness and modulation at the circuit level. *Journal of Neurophysiology*, 114(4):2472–2484.
- [17] DeWeerth, S. P., Patel, G. N., and Simoni, M. F. (1997). Variable linear-range sub-threshold OTA. *Electronics Letters*, 33(15):1309–1311.
- [18] Do, M. T. H. and Bean, B. P. (2003). Subthreshold Sodium Currents and Pacemaking of Subthalamic Neurons: Modulation by Slow Inactivation. *Neuron*, 39(1):109–120.
- [19] Douglas, R., Mahowald, M., and Mead, C. (1995). Neuromorphic Analogue VLSI. *Annual Review of Neuroscience*, 18(1):255–281.
- [20] Drion, G., Dethier, J., Franci, A., and Sepulchre, R. (2018a). Switchable slow cellular conductances determine robustness and tunability of network states. *PLOS Computational Biology*, 14(4):e1006125.
- [21] Drion, G., Franci, A., Dethier, J., and Sepulchre, R. (2015a). Dynamic Input Conductances Shape Neuronal Spiking. *eNeuro*, 2(1).
- [22] Drion, G., Franci, A., and Sepulchre, R. (2018b). Cellular switches orchestrate rhythmic circuits. *Biological Cybernetics*.
- [23] Drion, G., Franci, A., Seutin, V., and Sepulchre, R. (2012). A novel phase portrait for neuronal excitability. *PloS one*, 7(8):e41806.
- [24] Drion, G., O’Leary, T., and Marder, E. (2015b). Ion channel degeneracy enables robust and tunable neuronal firing rates. *Proceedings of the National Academy of Sciences*, 112(38):E5361–E5370.
- [25] Ermentrout, G. B. and Terman, D. H. (2010). *Mathematical Foundations of Neuroscience*. Springer Science & Business Media.
- [26] Farquhar, E. and Hasler, P. (2005). A bio-physically inspired silicon neuron. *IEEE Transactions on Circuits and Systems I: Regular Papers*, 52(3):477–488.
- [27] FitzHugh, R. (1961). Impulses and physiological states in theoretical models of nerve membrane. *Biophysical journal*, 1(6):445.
- [28] Folowosele, F., Hamilton, T. J., and Etienne-Cummings, R. (2011). Silicon Modeling of the Mihalaş–Niebur Neuron. *IEEE Transactions on Neural Networks*, 22(12):1915–1927.

- [29] Franci, A., Drion, G., and Sepulchre, R. (2012). An Organizing Center in a Planar Model of Neuronal Excitability. *SIAM Journal on Applied Dynamical Systems*, 11(4):1698–1722.
- [30] Franci, A., Drion, G., and Sepulchre, R. (2014). Modeling the Modulation of Neuronal Bursting: A Singularity Theory Approach. *SIAM Journal on Applied Dynamical Systems*, 13(2):798–829.
- [31] Franci, A., Drion, G., and Sepulchre, R. (2017). Robust and tunable bursting requires slow positive feedback. *Journal of Neurophysiology*, 119(3):1222–1234.
- [32] Franci, A., Drion, G., Seutin, V., and Sepulchre, R. (2013). A Balance Equation Determines a Switch in Neuronal Excitability. *PLoS Computational Biology*, 9(5):e1003040.
- [33] Franci, A. and Sepulchre, R. (2014). Realization of nonlinear behaviors from organizing centers. In *53rd IEEE Conference on Decision and Control*, pages 56–61.
- [34] Furber, S. (2016). Large-scale neuromorphic computing systems. *Journal of Neural Engineering*, 13(5):051001.
- [35] Furth, P. M. and Andreou, A. G. (1995). Linearised differential transconductors in subthreshold CMOS. *Electronics Letters*, 31(7):545–547.
- [36] Goldman, M. S., Golowasch, J., Marder, E., and Abbott, L. F. (2001). Global Structure, Robustness, and Modulation of Neuronal Models. *Journal of Neuroscience*, 21(14):5229–5238.
- [37] Gray, C. M. and McCormick, D. A. (1996). Chattering Cells: Superficial Pyramidal Neurons Contributing to the Generation of Synchronous Oscillations in the Visual Cortex. *Science*, 274(5284):109–113.
- [38] Gutierrez, G. J. and Marder, E. (2014). Modulation of a Single Neuron Has State-Dependent Actions on Circuit Dynamics. *eNeuro*, 1(1).
- [39] Gutierrez, G. J., O’Leary, T., and Marder, E. (2013). Multiple Mechanisms Switch an Electrically Coupled, Synaptically Inhibited Neuron between Competing Rhythmic Oscillators. *Neuron*, 77(5):845–858.
- [40] Harris-Warrick, R. M. (2011). Neuromodulation and flexibility in Central Pattern Generator networks. *Current Opinion in Neurobiology*, 21(5):685–692.
- [41] Herz, A. V., Gollisch, T., Machens, C. K., and Jaeger, D. (2006). Modeling single-neuron dynamics and computations: A balance of detail and abstraction. *science*, 314(5796):80–85.
- [42] Hindmarsh, J. L. and Rose, R. M. (1984). A model of neuronal bursting using three coupled first order differential equations. *Proceedings of the Royal Society of London B: Biological Sciences*, 221(1222):87–102.
- [43] Hodgkin, A. L. and Huxley, A. F. (1952). A quantitative description of membrane current and its application to conduction and excitation in nerve. *The Journal of physiology*, 117(4):500.

- [44] Hopfield, J. J. (1984). Neurons with graded response have collective computational properties like those of two-state neurons. *Proceedings of the National Academy of Sciences*, 81(10):3088–3092.
- [45] Hynna, K. M. and Boahen, K. (2006). Neuronal ion-channel dynamics in silicon. In *Circuits and Systems, 2006. ISCAS 2006. Proceedings. 2006 IEEE International Symposium On*, pages 4–pp. IEEE.
- [46] Hynna, K. M. and Boahen, K. (2007). Thermodynamically equivalent silicon models of voltage-dependent ion channels. *Neural Computation*, 19(2):327–350.
- [47] Indiveri, G. (2003). A low-power adaptive integrate-and-fire neuron circuit. In *2003 IEEE International Symposium on Circuits and Systems (ISCAS)*, volume 4, pages IV–IV.
- [48] Indiveri, G., Linares-Barranco, B., Hamilton, T. J., van Schaik, A., Etienne-Cummings, R., Delbruck, T., Liu, S.-C., Dudek, P., Häfliger, P., Renaud, S., Schemmel, J., Cauwenberghs, G., Arthur, J., Hynna, K., Folowosele, F., Saighi, S., Serrano-Gotarredona, T., Wijekoon, J., Wang, Y., and Boahen, K. (2011). Neuromorphic Silicon Neuron Circuits. *Frontiers in Neuroscience*, 5.
- [49] Indiveri, G., Linares-Barranco, B., Legenstein, R., Deligeorgis, G., and Prodromakis, T. (2013). Integration of nanoscale memristor synapses in neuromorphic computing architectures. *Nanotechnology*, 24(38):384010.
- [50] Izhikevich, E. (2004). Which Model to Use for Cortical Spiking Neurons? *IEEE Transactions on Neural Networks*, 15(5):1063–1070.
- [51] Izhikevich, E. M. (2000). Neural excitability, spiking and bursting. *International Journal of Bifurcation and Chaos*, 10(06):1171–1266.
- [52] Izhikevich, E. M. (2003). Simple model of spiking neurons. *IEEE Transactions on neural networks*, 14(6):1569–1572.
- [53] Izhikevich, E. M. (2007). *Dynamical Systems in Neuroscience*. MIT press.
- [54] Jo, S. H., Chang, T., Ebong, I., Bhadviya, B. B., Mazumder, P., and Lu, W. (2010). Nanoscale Memristor Device as Synapse in Neuromorphic Systems. *Nano Letters*, 10(4):1297–1301.
- [55] Keener, J. and Sneyd, J. (2009). *Mathematical Physiology: I: Cellular Physiology*. Interdisciplinary Applied Mathematics. Springer-Verlag, New York, second edition.
- [56] Keener, J. P. (1983). Analog circuitry for the van der Pol and FitzHugh-Nagumo equations. *IEEE Transactions on Systems, Man and Cybernetics*, (5):1010–1014.
- [57] Koch, C. (2004). *Biophysics of Computation: Information Processing in Single Neurons*. Oxford university press.
- [58] Krahe, R. and Gabbiani, F. (2004). Burst firing in sensory systems. *Nature Reviews Neuroscience*, 5(1):13–23.

- [59] Lazzaro, J., Ryckebusch, S., Mahowald, M., and Mead, C. A. (1989). Winner-Take-All Networks of $O(N)$ Complexity. In Touretzky, D. S., editor, *Advances in Neural Information Processing Systems 1*, pages 703–711. Morgan-Kaufmann.
- [60] Lee, Y. J., Lee, J., Kim, K. K., Kim, Y.-B., and Ayers, J. (2007). Low power CMOS electronic central pattern generator design for a biomimetic underwater robot. *Neurocomputing*, 71(1-3):284–296.
- [61] Lewis, M., Etienne-Cummings, R., Cohen, A., and Hartmann, M. (2000). Toward biomorphic control using custom aVLSI CPG chips. In *Proceedings 2000 ICRA. Millennium Conference. IEEE International Conference on Robotics and Automation. Symposia Proceedings (Cat. No.00CH37065)*, volume 1, pages 494–500, San Francisco, CA, USA. IEEE.
- [62] Linares-Barranco, B., Sánchez-Sinencio, E., Rodríguez-Vázquez, A., and Huertas, J. L. (1991). A CMOS implementation of FitzHugh-Nagumo neuron model. *IEEE Journal of Solid-State Circuits*, 26(7):956–965.
- [63] Liu, S.-C. and Delbruck, T. (2010). Neuromorphic sensory systems. *Current Opinion in Neurobiology*, 20(3):288–295.
- [64] Liu, Z., Golowasch, J., Marder, E., and Abbott, L. F. (1998). A Model Neuron with Activity-Dependent Conductances Regulated by Multiple Calcium Sensors. *Journal of Neuroscience*, 18(7):2309–2320.
- [65] Lyon, R. and Mead, C. (1988). An analog electronic cochlea. *IEEE Transactions on Acoustics, Speech, and Signal Processing*, 36(7):1119–1134.
- [66] Maher, M., Deweerth, S., Mahowald, M., and Mead, C. (1989). Implementing neural architectures using analog VLSI circuits. *IEEE Transactions on Circuits and Systems*, 36(5):643–652.
- [67] Mahowald, M. and Douglas, R. (1991). A silicon neuron. *Nature*, 354(6354):515–518.
- [68] Marder, E. (2012). Neuromodulation of Neuronal Circuits: Back to the Future. *Neuron*, 76(1):1–11.
- [69] Marder, E. and Bucher, D. (2007). Understanding Circuit Dynamics Using the Stomatogastric Nervous System of Lobsters and Crabs. *Annual Review of Physiology*, 69(1):291–316.
- [70] Marder, E. and Eisen, J. S. (1984). Electrically coupled pacemaker neurons respond differently to same physiological inputs and neurotransmitters. *Journal of Neurophysiology*, 51(6):1362–1374.
- [71] Marsat, G. and Pollack, G. S. (2006). A Behavioral Role for Feature Detection by Sensory Bursts. *Journal of Neuroscience*, 26(41):10542–10547.
- [72] McCormick, D. A. (1992). Neurotransmitter actions in the thalamus and cerebral cortex and their role in neuromodulation of thalamocortical activity. *Progress in Neurobiology*, 39(4):337–388.

- [73] Mead, C. (1989). *Analog VLSI and Neural Systems*, volume 1. Reading: Addison-Wesley.
- [74] Mead, C. (1990). Neuromorphic electronic systems. *Proceedings of the IEEE*, 78(10):1629–1636.
- [75] Mead, C. A. and Mahowald, M. A. (1988). A silicon model of early visual processing. *Neural Networks*, 1(1):91–97.
- [76] Merolla, P. A., Arthur, J. V., Alvarez-Icaza, R., Cassidy, A. S., Sawada, J., Akopyan, F., Jackson, B. L., Imam, N., Guo, C., Nakamura, Y., Brezzo, B., Vo, I., Esser, S. K., Appuswamy, R., Taba, B., Amir, A., Flickner, M. D., Risk, W. P., Manohar, R., and Modha, D. S. (2014). A million spiking-neuron integrated circuit with a scalable communication network and interface. *Science*, 345(6197):668–673.
- [77] Mihalaş, Ş. and Niebur, E. (2009). A Generalized Linear Integrate-and-Fire Neural Model Produces Diverse Spiking Behaviors. *Neural Computation*, 21(3):704–718.
- [78] Morris, C. and Lecar, H. (1981). Voltage oscillations in the barnacle giant muscle fiber. *Biophysical journal*, 35(1):193.
- [79] Nagumo, J., Arimoto, S., and Yoshizawa, S. (1962). An active pulse transmission line simulating nerve axon. *Proceedings of the IRE*, 50(10):2061–2070.
- [80] Nakada, K., Asai, T., and Amemiya, Y. (2003). An analog CMOS central pattern generator for interlimb coordination in quadruped locomotion. *IEEE Transactions on Neural Networks*, 14(5):1356–1365.
- [81] O’Leary, T. (2018). Homeostasis, failure of homeostasis and degenerate ion channel regulation. *Current Opinion in Physiology*, 2:129–138.
- [82] O’Leary, T., Williams, A. H., Franci, A., and Marder, E. (2014). Cell Types, Network Homeostasis, and Pathological Compensation from a Biologically Plausible Ion Channel Expression Model. *Neuron*, 82(4):809–821.
- [83] Oswald, A.-M. M., Chacron, M. J., Doiron, B., Bastian, J., and Maler, L. (2004). Parallel Processing of Sensory Input by Bursts and Isolated Spikes. *Journal of Neuroscience*, 24(18):4351–4362.
- [84] Plant, R. E. (1981). Bifurcation and resonance in a model for bursting nerve cells. *Journal of Mathematical Biology*, 11(1):15–32.
- [85] Pottelbergh, T. V., Drion, G., and Sepulchre, R. (2018). Robust Modulation of Integrate-and-Fire Models. *Neural Computation*, 30(4):987–1011.
- [86] Qiao, N., Mostafa, H., Corradi, F., Osswald, M., Stefanini, F., Sumislawska, D., and Indiveri, G. (2015). A reconfigurable on-line learning spiking neuromorphic processor comprising 256 neurons and 128K synapses. *Frontiers in Neuroscience*, 9.
- [87] Rangan, V., Ghosh, A., Aparin, V., and Cauwenberghs, G. (2010). A subthreshold aVLSI implementation of the Izhikevich simple neuron model. In *2010 Annual International Conference of the IEEE Engineering in Medicine and Biology*, pages 4164–4167, Buenos Aires. IEEE.

- [88] Ribar, L. and Sepulchre, R. (2017). Bursting through interconnection of excitable circuits. In *2017 IEEE Biomedical Circuits and Systems Conference (BioCAS)*, pages 1–4.
- [89] Ribar, L. and Sepulchre, R. (2018). Neuromorphic hyperpolarized bursting. *BMC Neuroscience*, 19(2):64.
- [90] Ribar, L. and Sepulchre, R. (2019). Neuromodulation of Neuromorphic Circuits. *IEEE Transactions on Circuits and Systems I: Regular Papers*, pages 1–13.
- [91] Rinberg, A., Taylor, A. L., and Marder, E. (2013). The Effects of Temperature on the Stability of a Neuronal Oscillator. *PLOS Computational Biology*, 9(1):e1002857.
- [92] Rinzel, J. (1987). A formal classification of bursting mechanisms in excitable systems. In *Mathematical Topics in Population Biology, Morphogenesis and Neurosciences*, pages 267–281. Springer.
- [93] Rinzel, J. and Ermentrout, G. B. (1989). Analysis of neural excitability and oscillations. In *Methods in Neuronal Modeling*, pages 135–169. MIT press.
- [94] Rinzel, J. and Lee, Y. S. (1987). Dissection of a model for neuronal parabolic bursting. *Journal of mathematical biology*, 25(6):653–675.
- [95] Sarpeshkar, R. (1998). Analog Versus Digital: Extrapolating from Electronics to Neurobiology. *Neural Computation*, 10(7):1601–1638.
- [96] Sarpeshkar, R., Lyon, R. F., and Mead, C. (1997). A Low-Power Wide-Linear-Range Transconductance Amplifier. *Analog Integrated Circuits and Signal Processing*, 13(1-2):123–151.
- [97] Sarpeshkar, R., Lyon, R. F., and Mead, C. A. (1996). An analog VLSI cochlea with new transconductance amplifiers and nonlinear gain control. In *1996 IEEE International Symposium on Circuits and Systems. Circuits and Systems Connecting the World. ISCAS 96*, volume 3, pages 292–296 vol.3.
- [98] Schemmel, J., Briiderle, D., Gribbl, A., Hock, M., Meier, K., and Millner, S. (2010). A wafer-scale neuromorphic hardware system for large-scale neural modeling. In *Proceedings of 2010 IEEE International Symposium on Circuits and Systems*, pages 1947–1950, Paris, France. IEEE.
- [99] Sepulchre, R., Drion, G., and Franci, A. (2018). Excitable Behaviors. In *Emerging Applications of Control and Systems Theory*, Lecture Notes in Control and Information Sciences - Proceedings, pages 269–280. Springer, Cham.
- [100] Sepulchre, R., Drion, G., and Franci, A. (2019a). Control Across Scales by Positive and Negative Feedback. *Annual Review of Control, Robotics, and Autonomous Systems*, 2(1):89–113.
- [101] Sepulchre, R., O’Leary, T., Drion, G., and Franci, A. (2019b). Control by neuromodulation: A tutorial. In *2019 18th European Control Conference (ECC)*, pages 483–497.
- [102] Sherman, S. M. (2001). Tonic and burst firing: Dual modes of thalamocortical relay. *Trends in neurosciences*, 24(2):122–126.

- [103] Simoni, M., Cymbalyuk, G., Sorensen, M., Calabrese, R., and DeWeerth, S. (2004). A Multiconductance Silicon Neuron With Biologically Matched Dynamics. *IEEE Transactions on Biomedical Engineering*, 51(2):342–354.
- [104] Simoni, M. and DeWeerth, S. (2006). Two-Dimensional Variation of Bursting Properties in a Silicon-Neuron Half-Center Oscillator. *IEEE Transactions on Neural Systems and Rehabilitation Engineering*, 14(3):281–289.
- [105] Simoni, M., Sorensen, M., Cymbalyuk, G., Calabrese, R., and DeWeerth, S. (2002). Control of bursting properties in a silicon neuron CPG. *Neurocomputing*, 44-46:645–651.
- [106] Simoni, M. F. and DeWeerth, S. P. (1999). Adaptation in a VLSI model of a neuron. *IEEE Transactions on Circuits and Systems II: Analog and Digital Signal Processing*, 46(7):967–970.
- [107] Simoni, M. F. and DeWeerth, S. P. (2007). Sensory Feedback in a Half-Center Oscillator Model. *IEEE Transactions on Biomedical Engineering*, 54(2):193–204.
- [108] Steriade, M., McCormick, D. A., and Sejnowski, T. J. (1993). Thalamocortical oscillations in the sleeping and aroused brain. *Science*, 262(5134):679–685.
- [109] Su, H., Alroy, G., Kirson, E. D., and Yaari, Y. (2001). Extracellular Calcium Modulates Persistent Sodium Current-Dependent Burst-Firing in Hippocampal Pyramidal Neurons. *The Journal of Neuroscience*, 21(12):4173–4182.
- [110] Swensen, A. M. and Bean, B. P. (2005). Robustness of Burst Firing in Dissociated Purkinje Neurons with Acute or Long-Term Reductions in Sodium Conductance. *Journal of Neuroscience*, 25(14):3509–3520.
- [111] Van der Pol, B. (1926). LXXXVIII. On “relaxation-oscillations”. *The London, Edinburgh, and Dublin Philosophical Magazine and Journal of Science*, 2(11):978–992.
- [112] Vogelstein, R. J., Tenore, F. V. G., Guevremont, L., Etienne-Cummings, R., and Mushahwar, V. K. (2008). A Silicon Central Pattern Generator Controls Locomotion in Vivo. *IEEE Transactions on Biomedical Circuits and Systems*, 2(3):212–222.
- [113] Wang, X.-J. and Rinzel, J. (1992). Alternating and Synchronous Rhythms in Reciprocally Inhibitory Model Neurons. *Neural Computation*, 4(1):84–97.
- [114] Watts, L., Kerns, D. A., Lyon, R. F., and Mead, C. A. (1992). Improved implementation of the silicon cochlea. *IEEE Journal of Solid-State Circuits*, 27(5):692–700.
- [115] Wijekoon, J. H. and Dudek, P. (2008). Compact silicon neuron circuit with spiking and bursting behaviour. *Neural Networks*, 21(2-3):524–534.
- [116] Wilson, C. J. and Bevan, M. D. (2011). Intrinsic dynamics and synaptic inputs control the activity patterns of subthalamic nucleus neurons in health and in Parkinson’s disease. *Neuroscience*, 198:54–68.
- [117] Wilson, H. R. (1999). *Spikes, Decisions, and Actions: The Dynamical Foundations of Neurosciences*. Oxford University Press, Incorporated.

-
- [118] Womack, M. D. and Khodakhah, K. (2003). Somatic and Dendritic Small-Conductance Calcium-Activated Potassium Channels Regulate the Output of Cerebellar Purkinje Neurons. *The Journal of Neuroscience*, 23(7):2600–2607.
- [119] Yu, T. and Cauwenberghs, G. (2010). Analog VLSI Biophysical Neurons and Synapses With Programmable Membrane Channel Kinetics. *IEEE Transactions on Biomedical Circuits and Systems*, 4(3):139–148.
- [120] Yu, T., Park, J., Joshi, S., Maier, C., and Cauwenberghs, G. (2012). 65k-neuron integrate-and-fire array transceiver with address-event reconfigurable synaptic routing. In *2012 IEEE Biomedical Circuits and Systems Conference (BioCAS)*, pages 21–24.
- [121] Yu, T., Sejnowski, T. J., and Cauwenberghs, G. (2011). Biophysical Neural Spiking, Bursting, and Excitability Dynamics in Reconfigurable Analog VLSI. *IEEE Transactions on Biomedical Circuits and Systems*, 5(5):420–429.

